DEVELOPMENT OF PIEZOELECTRIC MEMS DEVICES

BY

WANG TAO

(M.Sc., National University of Singapore)

(B. Eng., University of Electronic Science and Technology of China)

A THESIS SUBMITTED

FOR THE DEGREE OF DOCTOR OF PHILOSOPHY

DEPARTMENT OF ELECTRICAL AND COMPUTER ENGINEERING

NATIONAL UNIVERSITY OF SINGAPORE

2016

DECLARATION

I hereby declare that this thesis is my original work and it has been written by me in its entirety. I have duly acknowledged all the sources of information which have been used in the thesis.

This thesis has also not been submitted for any degree in any university previously.

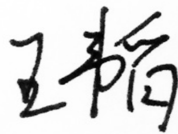

Wang Tao

10 January 2016

Acknowledgements

First and foremost, I would like to express my sincere gratitude to my supervisors Prof. Chengkuo Lee and Prof. Alex Gu for their consistent supports, encouragement and discussions during my entire Ph.D. study. I would like to gratefully acknowledge Prof. Lee for his invaluable guidance and insightful enlightenment throughout my Ph.D candidature. I would never forget his patience, encouragements and immense knowledge, which help me working through all the challenges during past four years. I also deeply appreciate Prof. Gu for offering such precious attachment opportunity in Institute of Microelectronics (IME) and his continuous consideration on me. I really could not have imagined the possibility of this dissertation without gracious concerns and kind helps from both of my supervisors.

Besides, I would like to thank Prof. Xiaojing Mu for his valuable suggestions on my research. Meanwhile, I am very grateful to Dr. Chengliang Sun, Dr. Jinghui Xu, Dr. Jifang Tao, Dr. Guoqiang Wu, Dr. Tao Sun and Dr. Min Tang for their continuous support and guidance during my attachment period. Without their helps, I would not able to complete the fabrication and characterization successfully.

In addition, I must express my sincere gratitude to all my past and present colleagues and friends in CICFAR lab: Dr. Liang Lou, Dr. Songsong Zhang, Prof. Huicong Liu, Dr. Nan Wang, Prof. Bin Yang, Prof. Jin Xie, Dr. Li Guo, Mr. Qiongfeng Shi, Ms. Nan Chen, Ms. Kailing Shih, Dr. Zhuolin Xiang, Dr. Bo Li, Dr. Kah How Koh, Dr. You Qian, Dr. Woon Soon Bo, Mr. Pitchappa Prakash, Mr. Chongpei Ho, Mr. Hao Wang, Mr. Sanghoon Lee, and so on. I would also like to thank Mrs. Chiow Mooi Ho and Mr. Chee Keong Koo for continuous technical

supports.

I would also like to express my genuine appreciation to my family. Without the encouragement from my parents and grandparents, I would not able to make such adventure. Last but not the least; I would also like to express my deepest gratitude to my beloved fiancée Ms. Lijun Yu, who has always been supporting me with her unselfish love, undeniably scarification and patience through the past years.

Table of Contents

DECLARATION iii
Acknowledgements iv
Table of Contents vi
Summary x
List of Tables xii
List of Figures xiii
List of Acronyms xxi
List of Symbols xxiv
Chapter 1 Introduction 1
1.1 Piezoelectric Materials 1
1.1.1 Aluminum Nitride (AlN) 3
1.1.2 Lead Zirconate Titanate (PZT) 4
1.1.3 Other materials 5
1.2 Basic Physics of Ultrasound 5
1.2.1 Background 6
1.2.2 Acoustic impedance 6
1.2.3 Reflection and transmission 7
1.2.4 Ultrasound intensity 8
1.2.5 Attenuation 9
1.2.6 Bandwidth 9
1.2.7 Ultrasound safety 10
1.3 Piezoelectric Ultrasonic MEMS Devices 10
1.3.1 Acoustic wave sensors (ultrasound within device) 10
1.3.2 Ultrasonic transducer (ultrasound outside device) 15
1.3.2.1 Bulk piezoelectric ultrasonic transducer 16
1.3.2.2 Capacitive micromachined ultrasonic transducer (cMUT) 18
1.3.2.3 Piezoelectric micromachined ultrasonic transducer (pMUT) 20
1.4 Thesis Organization 24
Chapter 2 Fabrication of Piezoelectric Ultrasonic MEMS Devices 26
2.1 Piezoelectric Material Deposition 26
2.1.1 Deposition of AlN thin film 26
2.1.1.1 Physical vapor deposition 27

2.1.1.2 Stress control 28
2.1.2 Deposition of PZT thin film 29
2.1.2.1 Sol-gel method 29
2.1.2.2 Electric poling 30
2.2 Piezoelectric Material Etching 33
2.2.1 AlN thin film etching 33
2.2.2 PZT thin film etching 34
2.3 Integrated Fabrication Process Flow 35
2.3.1 Backside deep-reactive ion etching (DRIE) 35
2.3.1.1 Acoustic wave sensors 35
2.3.1.2 PZT based pMUT 37
2.3.2 Cavity SOI wafer 38
Chapter 3 SAW Based MEMS Pressure Sensor 41
3.1 Design of SAW Based Pressure Sensor 43
3.2 Device Characterization and Results 44
3.2.1 Device characterization 44
3.2.2 Pressure testing 46
3.3 Study of the Diaphragm Shape Effect on Sensitivity 47
3.4 Methods of Sensitivity Enhancement 52
3.5 Summary 53
Chapter 4 Decoupled Viscosity and Density MEMS Sensor 54
4.1 Motivation 58
4.2 Working Principles and Sensor Design 60
4.3 Experimental Results and Discussions 66
4.3.1 Testing setup 67
4.3.2 Device testing in air 68
4.3.3 Liquids testing 69
4.3.3.1 Liquids testing using DI water, acetone ethanol and IPA 69
4.3.3.2 Liquids testing using glycerol-water mixtures 72
4.3.3.3 Liquids testing using NaCl solutions 74
4.3.3.4 Potential applications as a label-free liquid sensor 75
4.4 Summary 76
Chapter 5 Highly Efficient pMUT with Enhanced Performance 78

5.1 Zero-Bending Membrane pMUT ... 79
5.1.1 Design consideration ... 79
5.1.1.1 Stress influence on transmitting sensitivity ... 79
5.1.1.2 Realizing zero-bending membrane ... 81
5.1.2 Device characterization and discussion ... 85
5.2 pMUT with Piston-Like Membrane Motion ... 93
5.2.1 Concept and design ... 94
5.2.1.1 Perforated membrane ... 94
5.2.1.2 Advantages of using etching holes ... 96
5.2.2 Device characterization and discussion ... 96
5.3 Summary ... 100
Chapter 6 Towards PZT Based High Performance pMUT ... 102
6.1 pMUT Design and Optimization ... 103
6.2 Experimental Results and Discussions ... 106
6.2.1 Device characterization ... 106
6.2.2 In-Air transmitter testing ... 113
6.3 Summary ... 115
Chapter 7 pMUT with Ultra-wide Frequency Bandwidth ... 116
7.1 Motivation ... 117
7.2 Concept and Design ... 119
7.3 Device Characterization and Discussion ... 122
7.3.1 Device characterization in air ... 122
7.3.2 Underwater testing ... 125
7.3.2.1 Testing setup ... 125
7.3.2.2 Testing results and discussion ... 126
7.4 Summary ... 127
Chapter 8 Conclusions and Future Works ... 128
8.1 Summary of Current Works ... 128
8.2 Future Development of Electrically Switchable pMUT ... 129
8.2.1 Motivation ... 129
8.2.2 Concept and design ... 130
8.2.3 Preliminary characterization and discussion ... 132
Bibliography ... 137

Appendix: List of Publication........154
Journal Papers........154
Awards........155
Invited Talks........155
Conference Papers........155

Summary

Piezoelectric effect provides a direct transduction between electrical and mechanical domains. Such transduction is bidirectional, which means a piezoelectric device can work as both sensor and actuator. Varieties of piezoelectric micro electromechanical systems (MEMS) devices are presented in this thesis. Leveraging on the piezoelectric effect, acoustic wave based micro resonators are developed as the sensing elements. A series of surface acoustic wave (SAW) pressure sensors for harsh environment applications are designed, fabricated and characterized. The effect of diaphragm shape on the performance of SAW pressure sensors is studied as well. The longitudinal and lateral strains along the SAW propagation direction (<100> direction) have opposite effects on the frequency change, *i.e.* longitudinal strain increases the resonant frequency while lateral strain decreases the resonant frequency. It is found that the ratio of longitudinal/lateral strain is determined by the diaphragm shape. The rectangular diaphragm (large aspect ratio) with only lateral strain shows negative pressure coefficient of frequency (PCF), while those sensors where longitudinal strain dominates show positive PCF. In addition to the SAW sensor, a Lamb wave based viscosity and density sensor is also developed, with two unique modes employed. Unlike the conventional sensors, this sensor can measure the viscosity and density separately, providing a more accurate way of chemical detection.

In addition to the acoustic wave sensors, several aluminum nitride (AlN) or lead zirconate titanate (PZT) based piezoelectric micromachined ultrasonic transducers (pMUTs) are developed and investigated. Conventional piezoelectric ceramic based ultrasonic transducer suffers several inherent limitations, *e.g.* acoustic impedance

mismatch, poor bandwidth and poor sensitivity. Aiming at overcoming these limitations, the MEMS based pMUTs have several unique features. By using integrated vacuum cavity and frame-like top electrode configuration, a pMUT of perfectly flat membrane is achieved. Such pMUT has over 450% higher transmitting sensitivity than a conventional design. To further enhance the ultrasound transmitting efficiency, a pMUT with piston-like membrane motion is realized. The piston membrane motion can push more acoustic medium back and forth, generating a higher ultrasound pressure. With the high performance PZT thin film and optimized structure design, an airborne pMUT is developed as well. Besides, the mode-merging concept is proposed to extend the pMUT frequency bandwidth. Several higher modes are simultaneously excited and overlapped with fundamental mode, forming a much wider bandwidth. An ultra-wide bandwidth of 94.7% is eventually achieved. For the future plan, an innovative frequency switchable pMUT is still under investigation. Preliminary data show that its operating frequency can be electrically switched, without physically changing the ultrasonic transducers.

List of Tables

Table 1.1 Summary of densities, sound speeds and acoustic impedances of ultrasound media 7

Table 1.2 Summary of attenuation coefficients α 9

Table 2.1 Sputtering conditions for AlN thin film deposition 27

Table 3.1 Phase velocity sensitivity to strain γ for (100) Si plane [116] 50

Table 3.2 Phase velocity sensitivity to strain γ for (110) Si plane [116] 52

Table 4.1 Summary of mechanical properties of air and chemicals 69

Table 4.2 Summary of mechanical properties of glycerol-water mixtures 72

Table 4.3 Summary of mechanical properties of NaCl solutions 74

Table 5.1 Material properties applied in the FEM 82

Table 5.2 Comparison of the transmitting sensitivity 89

Table 6.1 Comparison of displacement sensitivities of reported PZT based pMUTs 110

List of Figures

Figure 1.1 (a) a piezoelectric disk generates a voltage when it is stressed (direct piezoelectric effect); (b) crystal structure of PZT material; (c) distortion of unit cell from the original shape under external electric fields (inverse piezoelectric effect) and; (d) orientation of domains before and after poling. 2

Figure 1.2 Schematic sketches of the four typical types of acoustic wave sensors: (a) the Thickness Shear Mode (TSM) device, (b) the Surface Acoustic Wave (SAW) device, (c) the Acoustic Plate Mode (APM) device and; (d) the Flexural Plate Wave (FPW) or Lamb wave device. 11

Figure 1.3 Comparison between the four types of acoustic wave devices. 12

Figure 1.4 Surface acoustic wave (SAW) moves vertically in a direction normal to the surface plane. The energy is confined to the surface, and SAW sensor is very sensitive to device surface changes. 13

Figure 1.5 Illustration of a typical Lamb wave sensor with the two Lamb wave modes. 14

Figure 1.6 Illustration of the interdigital transducer (IDT) for acoustic wave generation and detection. 15

Figure 1.7 Typical applications using ultrasonic transducers (UTs): (a) B-mode diagnostic ultrasonic imaging; (b) non-destructive flaw testing; (c) reserve parking sensor and; (d) liquid flow rate sensing. 16

Figure 1.8 Commercially available conventional UTs for various applications: (a) diagnostic ultrasonic imaging, (b) NDT and (c) range finding. 17

Figure 1.9 Typical cross-sectional structure of a cMUT [56]. 19

Figure 1.10 The SEM images of a cMUT array. cMUT employs an extremely small gap to maintain the performance [58]. 19

Figure 1.11 Typical cross-sectional structure of a pMUT [56]. 20

Figure 1.12 A recently reported 72*9 pMUT array and the HD ultrasonic images [53]. 21

Figure 1.13 (a) A miniaturized high dense pMUT array with 1261 elements [66] and; (b) an intravascular imaging probe with pMUT array [67] 22

Figure 1.14 (a) Demonstration of airborne gesture recognition for photo swiping

and; (b) 3-D range finding for targets detection [72]..................................22

Figure 1.15 A recently reported ultrasonic fingerprint sensor using pMUT array [73]..23

Figure 1.16 A tiny pMUT which functions as audio prosthesis is in-*vivo* implanted inside middle-ear [75]...23

Figure 2.1 Cross-sectional SEM image of deposited AlN thin film using sputtering..28

Figure 2.2 Measured residual stress of deposited AlN thin film as a function of thickness [83]..29

Figure 2.3 Cross-sectional SEM image of deposited PZT thin film....................30

Figure 2.4 The waveform of unipolar pulse poling signals. This waveform is 1 kHz triangle voltage pulse with interval of 0.1s for 10 times; (b) The measured piezoelectric constant d_{31} of the PZT thin films after DC poling and pulse poling and; (c) The measured dielectric loss of the PZT thin films after DC poling and pulse poling...32

Figure 2.5 (a) The SEM image of the etched AlN thin film using SiO_2 as hard mask and; (b) cross-sectional view. 33

Figure 2.6 The SEM image of PZT thin film after wet-etching. The edge is zigzagged because the HCl tends to rapidly attack PZT along the grain boundaries..34

Figure 2.7 Fabrication process flow of the acoustic wave sensor: (a) SOI substrate with 30µm or 50µm device silicon layer; (b) deposition of AlN layer using sputtering; (c) metal layer (Al or Mo) deposition and pattering to form IDT electrodes; (d) wafer thinning to 400µm, followed by 1µm SiO_2 hard mask deposition and pattering on backside; (e) backside Si DRIE release; (f) SiO_2 hard mask removal by wet etching...................................36

Figure 2.8 Fabrication process flow of the device: (a) SOI substrate with 5µm or 10µm device silicon layer and 400 µm handle silicon layer; (b) deposition of 1µm SiO_2/10nm Ti/200nm Pt/2µm MPB-PZT/10nm Ti/200nm Pt stack. The PZT thin film is deposited by sol-gel method, followed by RTA at 650°C for crystallization; (c) patterning of the stack. Ar ion milling, wet etching and RIE are for metal, PZT and SiO_2, respectively; (d) Au (100nm) wire bonding pads formation; (e) backside Si DRIE to release the flexural membrane and; (f) pulse poling of PZT thin film at 100V..........................37

Figure 2.9 Fabrication process flow of the AlN based pMUT: (a) Formation of the cavity SOI wafer; (b) Deposition of Mo / AlN / Mo stack; (c) Patterning of top Mo layer; (d) Deposition of PECVD SiO_2 for isolation, and SiO_2 and AlN are etched to open contact via (bottom). The contact via (top) is then opened by etching SiO_2; (e) Deposition and patterning of Al metal layer for electrical connections and to form bonding pads and; (f) Blank etching of

oxide by RIE. 39

Figure 3.1 (a) The 3-D schematic illustration of the AlN based SAW pressure sensor; (b) Cross-sectional view of the illustration. All the devices are fabricated on (100) wafer and the SAW propagating direction is along <100>. 43

Figure 3.2 (a) Optical microscope (OM) image of fabricated pressure sensor; Secondary electron microscope (SEM) images, showing the 50μm thick silicon layer; (c) Backside view of the three pressure sensors showing the different diaphragm shapes and; (d) Packaged and assembled pressure sensor with printed-circuit-board (PCB) for testing. The pressure is applied using hydraulic controller through the tube and the SMA connectors are for signal readout. 44

Figure 3.3 (a) Measured and simulated frequency responses of the pressure sensor. The mode shape indicates the induced acoustic wave is a SAW and; (b) – (d) The frequency change with respect to applied pressure for PS_A, PS_B and PS_C, respectively. 45

Figure 3.4 (a) Simulated Von Mises stress distributions of the three pressure sensors and; (b) The associated strain directions of the three pressure sensors. The dash lines indicate where the IDTs are located. 47

Figure 4.1 Liquid flow sensing system [127]: (a) geometry of viscosity & density sensor with liquid flow channel; (b) block diagram of the flowing system for the sensor measurements in liquid phase; (c) transient frequency responses of the sensor to various aqueous solutions (with constant concentration) and; (d) transient frequency responses of the sensor as a function of concentration for KCl aqueous solutions. 55

Figure 4.2 Viscosity and density detection based smart tongue device [118]: (a) photograph of fabricated device; (b) Photograph of the assembled device with the liquid reservoir used for experimental setup; (c) testing of different liquids showing excellent discrimination; (d) testing of milk samples with different skimmed-level and; (e) Testing of milk samples showing the effect of aging. 56

Figure 4.3 Analytical system for residual liquid detergent detection [128]: (a) photograph of the assembled system; (b) OM of fabricated sensor; (c) principal components analysis of different detergents and; (d) frequency response vs. different concentrations of detergent solutions. 57

Figure 4.4 Real-Time monitoring of whole blood coagulation [129]: (a) Schematic illustration; (b) an SEM image of the fabricated device; (c) Viscosity characterization and; (d) Real-time monitoring the coagulation process of a citrated blood. 57

Figure 4.5 (a) Dual SAW sensors from [136]. $(\eta \cdot \rho)^{1/2}$ is measured using sensor with smooth surface while ρ is obtained by sensor with corrugated surface. η can be derived from the two values and; (b) frequency response of the

Lamb wave sensor from [137]. Frequency response is assumed to be independent with liquid viscosity, but this is only valid when viscosity is small enough. 59

Figure 4.6 Schematic drawing of the directly decoupled viscosity and density sensor: (a) bird's view and; (b) cross-sectional view. The IDT electrodes induce the Lamb wave within the plate. Relatively thick device silicon (30μm) is employed for the plate to lower the frequency of higher-order modes. 62

Figure 4.7 Simulation results of Mode 1: (a) mode shape; (b) velocity vectors on backside surface and; (c) zoom-in view of velocity vectors. Motion of particles on backside surface is entirely in-plane, generating shear waves in liquid. 63

Figure 4.8 Simulation results of Mode 2: (a) mode shape; (b) velocity vectors on backside surface and; (c) zoom-in view of velocity vectors. Motion of particles on backside surface is out-of-plane, generating longitudinal waves in liquid. 64

Figure 4.9 Simulated relative frequency shifts to the density of (a) Mode 1 and (b) Mode 2. Frequency of Mode 1 does not shift to density at all, which can be used for viscosity sensing. 66

Figure 4.10 The fabricated decoupled viscosity and density sensor: (a) optical microscope photograph; (b) scanning electron microscope (SEM) photograph; and (c) cross-sectional SEM photograph. 66

Figure 4.11 (a) Schematic drawing of packaged sensor with loaded liquid under test; sensor mounted on the holed PCB with sealed bonding wires by silicone (b) front side and (c) backside; (d) PCB calibration kit for eliminating the interferences from cables and PCB package 68

Figure 4.12 S11 parameter in the range of 400 MHz to 600 MHz, measured in air using Agilent E5071B network analyzer. The signal is quite stable while high Q-factor makes easy and accurate frequency determination possible . 68

Figure 4.13 Relative frequency shifts to the square root of viscosity-density product of Mode A in DI water, acetone, ethanol and IPA. DI water and ethanol share the same frequency response. 70

Figure 4.14 Relative frequency shifts to the viscosity of Mode C in DI water, acetone, ethanol and IPA. DI water and ethanol are discriminated due to their different viscosities. 71

Figure 4.15 Relative frequency shifts to the density of Mode D in DI water, acetone, ethanol and IPA. Acetone, ethanol and IPA cannot be differentiated because of the almost same density, indicating frequency response of Mode D is not influenced by viscosity. 71

Figure 4.16 Relative frequency shifts in glycerol-water solutions with volumic

concentration from 0% to 50%: (a) Mode A to the square root of viscosity-density product; (b) Mode C to the viscosity and; (c) Mode D to the density. 73

Figure 4.17 Relative frequency shifts in NaCl-water solutions with mass concentration from 0% to 20%: (a) Mode A to the square root of viscosity-density product; (b) Mode C to the viscosity and; (c) Mode D to the density. 75

Figure 4.18 A novel 2-D method for label-free liquid detiction. Frequency responses of Mode C and Mode D are plotted in X-axis and Y-axis, respectively. Liquids with same viscosity-density product or same density can be easily discriminated by this method. 76

Figure 5.1 Two typical conventional pMUT designs with: (a) Frame-like top electrode; (b) Central top electrode. The simulation results of residual stress induced buckling: (c) Design 1 and; (d) Design 2. 81

Figure 5.2 3-D schematic drawings of: (a) & (c) the zero-bending pMUT, denoted as Device A; (b) Reference pMUT, denoted as Device B and; (d) & (e) Comparison of Device A and B. Vacuum pressure can compensate the initial bending of Device A, but aggravate the initial bending of Device B. 83

Figure 5.3 Simulation results of membrane deflection: (a) Device A; (b) Device B and; (c) Stress distribution in the AlN layer of Device A along A-A' direction before and after vacuum pressure compensation. 84

Figure 5.4 The fabricated pMUT devices: (a) OM images and; (b) SEM images. 85

Figure 5.5 The cross-sectional view of SEM image, showing the integrated vacuum cavity. 86

Figure 5.6 (a) The 3-D images captured by holographic MEMS analyzer and; (b) The extracted surface profiles. Maximum deflection of the Device A is less than 10nm, which is considered as zero-bending, and the deflection of Device B is 96nm. The measured profiles match the simulation results very well...87

Figure 5.7 Simulated and measured frequency responses of displacement amplitude with 1 V AC excitation for: (a) Device A and; (b) Device B. The inset shows the vibration mode shapes from both simulation and measurement. 87

Figure 5.8 The impedance measurement results of the zero-bending pMUT (Device A): (a) measured in air and; (b) measured in DI water. 91

Figure 5.9 Simulation and measurement results of the pMUTs (frame-like top electrode) with different sizes: (a) The resonant frequency and; (b) The displacement amplitude. The 300μm pMUTs with and without 0.7μm oxide

layer: (c) Optical microscope images and; (d) measured surface profiles...91

Figure 5.10 Transmitting sensitivity comparison of 300μm pMUTs: (a) without top oxide layer and; (b) with top oxide layer. The displacement amplitude is normalized to the simulation result, i.e. the ideal displacement amplitude. 93

Figure 5.11 Illustrations of the piston-like pMUT. The etching holes located inner top electrode, are through all layers..94

Figure 5.12 Simulated mode shapes by FEA modeling: (a) classical pMUT and; (b) piston-like pMUT. With the help of etching holes, the mode shape has a relatively flat surface...95

Figure 5.13 (a) The optical microscope images of fabricated pMUTs. The classical pMUT is denoted as Device A, and the piston-like pMUTs with two and three rows of etching holes are denoted as Device B and Device C, respectively; (b) the SEM image of Device C; (b) SEM images showing the etching holes and; (d) cross-sectional view of pMUT membrane. 97

Figure 5.14(a) Surface profiles of the pMUTs at resonance; (b) 3-D images of *Device C*; (c) frequency responses of displacement amplitude for piston-like pMUT. Inset table shows the comparison of the three devices and; (d) simulated far field space pressure levels for *Device A & C*.........................99

Figure 6.1 Schematic drawings of the proposed high performance pMUT: (a) 3-D illustration and; (b) cross-sectional view of illustration. 103

Figure 6.2 The FEM results for pMUT design optimization: (a) normalized displacement with respect to silicon thickness and; (b) normalized displacement with respect to top electrode width.....................................104

Figure 6.3 Comparison of the pMUTs with etched PZT/Pt/SiO_2 stack and without the etched stack. The FEA modeling results indicate that the pMUT with etched stack has about twice higher sensitivity...105

Figure 6.4 The as-fabricated pMUT devices. The red dash lines in optical microscope image indicate the released membrane, which is slightly wider than top electrode to achieve the best performance. The inset shows the pMUT with dual in-line package (DIP) for testing...................................106

Figure 6.5 The cross-sectional view of the SEM image. It is clearly shown the BOX is completely removed and the top electrode and PZT stack partially covers the released membrane. This fabricated pMUT fulfills all the design requirements to achieve its optimized performance. 107

Figure 6.6 The secondary electron microscope (SEM) images of the fabricated pMUT. As the edge of the wet-etched PZT is zigzagged, the PZT thin film and bottom electrode is intentionally larger than top electrode to avoid the short circuit. 108

Figure 6.7 3-D image of the pMUT, captured by the digital holographic

microscope. No obvious membrane buckling can be observed. 108

Figure 6.8 The measured displacement sensitivity of the pMUT without DC offset. A 807nm/V sensitivity is achieved at the resonant frequency (482kHz), which is considerbly high. The 3-D mode shape captured during vibration is shown as well. 110

Figure 6.9 The impedance measurement results of the pMUT. The PZT based devices shows relatively low impedance, and standard 50Ω can be achieved by connecting 7 pMUTs in parallel for impedance match. The electromechanical coupling coefficient can be derived from the resonant and anti-resonant frequency as 1.62%. 111

Figure 6.10 The uniformity testing results of the the pMUT array. This pMUT array shows quite good uniformity, where the maximum frequency deviation is only 1.67% 112

Figure 6.11 The setup for in-air transmitting testing: (a) A standard ultrasound source is used for calibration first, which is able to generate 79dB SPL at distance of 250mm and; (b) pMUT is driven by 2V sinusoidal signals, and the transmitted ultrasound is recorded by the ultrasound microphone. 113

Figure 6.12 (a) The recorded ultrasound transmitted by a single pMUT element at a distance of 10mm and; (b) The SPL chagne with respect to the distance. The SPL drops exponentially, and the deviations at distance of 20mm and 30mm are probably due to the standing wave between the pMUT and the microphone. 115

Figure 7.1 (a) Longer pulse (Pulse A) in time domain and frequency domain and; (b) Shorter pulse (Pulse B) in time domain and frequency domain. 117

Figure 7.2 (a) The schematic drawing of proposed pMUT; (b) Relation between *a* and length / width aspect ratio *k*; (c) Derived modal frequency ratios with varying *k* and; (d) The associated mode shapes. 121

Figure 7.3 (a) OM image of fabricated pMUT; SEM image of (b) cross-sectional view of released multi-layer membrane; (c) pMUT array and; (d) edge of pMUT element. 122

Figure 7.4 (a) Simulated and measured frequency response under 1 V_{pp} electrical excitation; (b) The mode shape for each resonant peak. Left ones are measured (multimedia view) and right ones are obtained by simulation; (c) Impedance measurement results and; (d) Comparison of analytical model, FEM simulation and measurement results. 123

Figure 7.5 (a) Underwater performance testing results using hydrophone and; (b) The corresponding Fast Fourier Transform (FFT) spectrum. The testing set-up is shown in the inset. 126

Figure 8.1 (a) 3-D schematic illustration of the switchable pMUT, which has five individual top electrodes and; (b) The electrical connections of the top

electrodes. The top electrodes are divided into three sets, denoted as Electrode A, B and C. 131

Figure 8.2 The as-fabricated switchable pMUT: (a) OM image of the pMUT array; (b) SEM image of a single pMUT element. The minimum feature size is 1μm; (c) The multilayer metal structures and vias and: (d) cross-sectional view of the device. 133

Figure 8.3 The activated electrode sets and the corresponding phase image for each resonance mode. By activating different sets of top electrodes, the synthesized effective electrode matches the in-phase motion parts of the membrane to achieve efficient coupling. 134

Figure 8.4 Performance comparison of reference pMUT and switchable pMUT: measured frequency response of displacement amplitude with 1V input voltage at each mode. The simulated mode shapes by FEA modeling are also shown as insets. 135

List of Acronyms

MEMS	Micro-electro-mechanical systems
SAW	Surface acoustic wave
TSM	Thickness shear mode
APM	Acoustic plate mode
FPW	Flexural plate wave
BAW	Bulk acoustic wave
FBAR	Film bulk acoustic resonator
dB	Decibel
PCF	Pressure coefficient of frequency
AlN	Aluminum Nitride
PZT	Lead zirconate titanate
MPB-PZT	Morphotropic phase boundary composition PZT (Zr/Ti=52/48)
Tetra-PZT	Tetragonal PZT (Zr/Ti=30/70)
ZnO	Zinc Oxide
PVDF	Polyvinylidene fluoride
CMOS	Complementary metal-oxide-semiconductor
IC	Integrated circuits
VOA	Variable optical attenuator
EH	Energy harvester
FDA	Food and Drug Administration (United states of America)
IDT	Inter-digital transducer
NDT	Non-destructive testing

UT	Ultrasonic transducer
MUT	Micromachined ultrasonic transducer
cMUT	Capacitive micromachined ultrasonic transducer
pMUT	Piezoelectric micromachined ultrasonic transducer
HD	High definition
FWHM	Full width at half maximum
XRD	x-ray diffraction
RTA	Rapid thermal annealing
RIE	Reactive-ion etching
DRIE	Deep reactive-ion etching
Ar	Argon
N_2	Nitrogen
Si	Silicon
SiO_2	Silicon dioxide
Al	Aluminum
Mo	Molybdenum
Pb	Lead
Ti	Titanium
BCl_3	Boron trichloride
HF	Hydrofluoric acid
HCl	Hydrochloric acid
H_2O	Water
PR	Photoresist
PbClF	Lead chloride fluoride
HNO_3	Nitric acid

PECVD	Plasma-enhanced chemical vapor deposition
SOI	Silicon-on-insulator
BOX	Buried oxide
DC	Direct current
AC	Alternating current
ALD	Atomic layer deposition
OM	Optical microscope
SEM	Secondary electron microscope
SOLT	Short-Open-Load-Through (a calibration method)
FEA	Finite elements analysis
FEM	Finite elements model
PDMS	Polydimethylsiloxane
PCB	Printed circuits board
IPA	Isopropyl alcohol
DI water	Deionized water
SPL	Sound pressure level
DIP	Dual in line package
DUT	Device under testing
FFT	Fast Fourier Transform
IVUS	Intravascular ultrasound (an ultrasonic imaging technology)

List of Symbols

Z	Acoustic impedance
ρ	Density of the ultrasound medium
c	Sound speed in the ultrasound medium
p_r	The reflected ultrasound pressure
p_i	The incident ultrasound pressure
p_t	The transmitted ultrasound pressure
θ_i	The angle of incident wave to the normal
θ_t	The angle of transmitted wave to the normal
Z_1	The acoustic impedance of medium 1 (incident wave)
Z_2	The acoustic impedance of medium 2 (transmitted wave)
c_1	The sound speed in medium 1
c_2	The sound speed in medium 2
I	Ultrasound intensity
T	Time
A	Ultrasound attenuation in dB
α	Ultrasound attenuation coefficient
l	Ultrasonic wave propagating distance
u	Particle motion speed
d_{31}	Transverse axial piezoelectric constant
f	Frequency of ultrasonic wave
v_{ph}	The phase velocity of the acoustic wave
λ	The wavelength of the acoustic wave

σ	Mechanical stress or residual stress
ε	Mechanical strain
u	Mechanical displacement (SAW device)
c	Linear elastic moduli (SAW device)
c'	Third-order elastic moduli (SAW device)
e	Piezoelectric moduli (SAW device)
ϵ	Permittivity tensors (SAW device)
φ	Electric potential (SAW device)
v_0	The phase velocity with zero strain
γ	The velocity sensitivity to strain
B	Bending stiffness
d	Plate thickness
E	Young's modulus
υ	Poisson's ratio
M_{eff}	Effective mass
M_{plate}	Unit plate mass
M_{den}	Mass loading due to liquid density
M_{vis}	Viscous loading of the liquid
η	Liquid viscosity
ρ	Liquid density
D	Modulus of flexural rigidity
ρ_s	The area plate density
M^p	The piezoelectric moment induced by input voltage
T^s	The overall plate tension caused by the residual stresses
M^s	The residual moment about the neutral plane

k_{eff}^2	Electromechanical coupling coefficient
f_r	Resonant frequency
f_a	Anti-resonant frequency
L_x	Length of rectangular membrane
L_y	Width of rectangular membrane
m	Mode number
n	Mode number
$f_{m,n}$	Frequency of rectangular membrane at mode (m,n)
T	Surface tension
k	The length / width ratio
f_0	Frequency of fundamental mode
S_{ref}	The sensitivity of the reference pMUT (conventional design)

Chapter 1 Introduction

The phenomenon of piezoelectricity was discovered by brothers Pierre and Paul-Jacques Curie in 1880. Piezoelectricity is coined in 1881 by Wilhelm Hankel, and remained a curiosity until 1921, when Walter Cady discovered the quartz resonator for stabilizing electronic oscillators. Piezoelectricity refers to the production of electrical charges by the applied mechanical stress (see Figure 1.1 (a)), and this is known as the direct effect of piezoelectricity. This phenomenon is reciprocal. Alternately, the same materials are able to produce a mechanical deformation when an electric field is applied to them, and this is called the inverse effect of piezoelectricity. Piezoelectric effect provides a direct transduction between electric and mechanical domains. Acoustic wave, or ultrasonic wave, thus can be generated and detected using the piezoelectric devices.

1.1 Piezoelectric Materials

Piezoelectric materials are crystals. The microscopic origin of piezoelectricity is the displacement of ionic charges within a crystal, leading to the polarization and electric field. A stress applied to a piezoelectric crystal alters the spacing between centers of positive and negative charge sites; this leads to a net polarization manifested as open circuit voltages measurable at the crystal surface. Inversely, an external electric field exerts a force between the centers of positive and negative charges, leading to an elastic strain and changes of dimensions. The inverse piezoelectric effect is shown in Figure 1.1 (b) and (c), using lead zirconate titanate (PZT) material as an example.

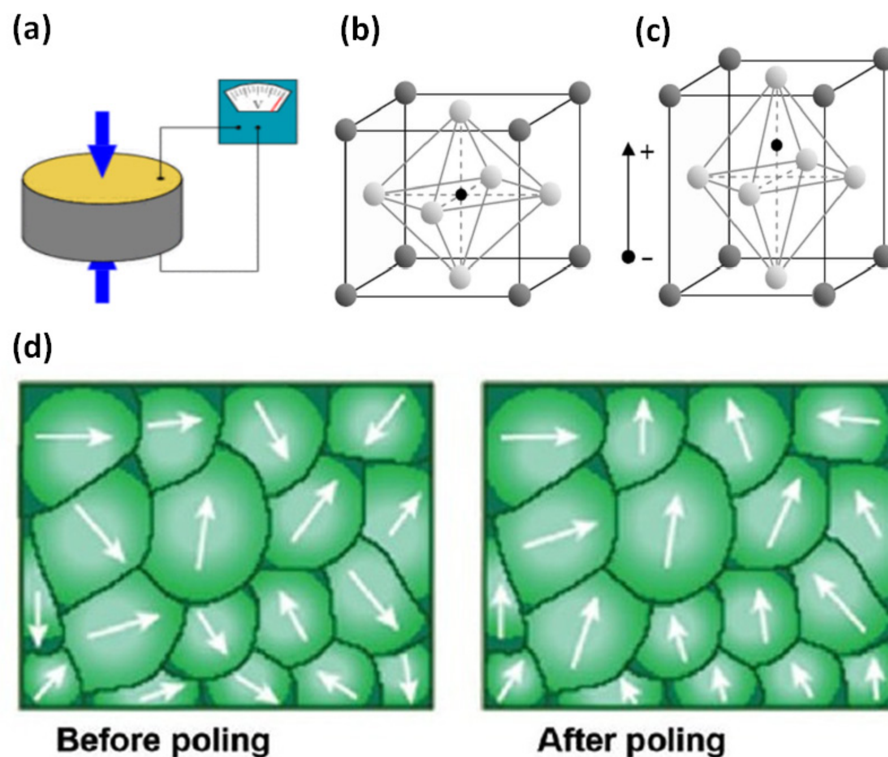

Figure 1.1 (a) a piezoelectric disk generates a voltage when it is stressed (direct piezoelectric effect); (b) crystal structure of PZT material; (c) distortion of unit cell from the original shape under external electric fields (inverse piezoelectric effect) and; (d) orientation of domains before and after poling.

Piezoelectric crystals are usually poly-crystalline, which can be considered to be a mass of domains. The macroscopic behavior of the crystal may differ from that of individual domains, due to the orientation of such domains. Owing to the random distribution of domains throughout the material, no overall polarization or piezoelectric effect is exhibited. A crystal can be made piezoelectric in any chosen direction by electric poling, which involves exposing it to a strong electric field at an elevated temperature. Under the action of this field, domains that are aligned with the field grow at the expenses of others. When the field is removed, the dipoles remain locked in an approximate alignment, giving the crystal a remnant polarization, shown in Figure 1.1 (d).

Piezoelectric materials hence enable electromechanical transduction. Transducers using piezoelectric materials can be configured either as actuators, when the design of the device is optimized for generating mechanical strain using the inverse piezoelectric effect, or as sensors when the design of the device is optimized for the generation of an electric signal using the direct piezoelectric effect.

Several most commonly used piezoelectric materials are listed below:

- Single crystals: Aluminum Nitride (AlN), Zinc Oxide (ZnO), Quarts, *etc.*
- Piezo-ceramics: Lead Zirconate Titanate (PZT) - $Pb(Zr_xTi_{1-x})O_3$
- Piezo-polymers: Polyvinylidene Fluoride (PVDF) and its copolymers, Nylon
- Composites: PVDF+PZT

Each of the piezoelectric material has specific advantages and disadvantages, which include performance, cost, temperature dependence, fabrication process, attenuation and loss, acoustic wave propagation velocity, bio-compatibility, compatibility with complementary metal-oxide-semiconductor (CMOS) process *etc.*

1.1.1 Aluminum Nitride (AlN)

AlN is a III-V semiconducting compound. When they are pure, AlN crystals are hard, colorless and transparent [1]. AlN has a wurtzite crystal structure and is a covalent bonded material. This material is stable to very high temperatures in inert atmospheres. In air, surface oxidation occurs above 700°C. The formed layer of aluminum oxide protects the material up to 1370°C, and bulk oxidation occurs above this temperature. The most important advantage of AlN is that its deposition is compatible with CMOS microelectronic process. AlN based piezoelectric devices may be able to integrate with integrated circuits (ICs) in monolithic chip. AlN thus has gained much interest in new prospects such as bulk acoustic wave (BAW) and film

bulk acoustic resonator (FBAR) technology [2-4]. Besides all the above mentioned advantages, the chemical stability of AlN is good as well [5, 6]. Therefore, AlN is an attractive candidate for liquid sensing and is adopted as the piezoelectric material in this research. Some key properties of AlN are given as follows:

- Dielectric constant: $\varepsilon = 8.5$;
- Piezoelectric coefficient: $d_{31} = 1.55$;
- Thermal expansion coefficient: $a = 5.27$ (close to that of silicon);
- Non-reactive with normal chemicals and gases during microelectronic process;
- Compatible with CMOS process.

1.1.2 Lead Zirconate Titanate (PZT)

PZT is another popular piezoelectric material. The considerably high electromechanical coupling efficiency makes it a very attractive material for micro sensors and micro actuators. According to the composition (ratio of zirconate and titanate), two types of PZT thin film are most widely used: the morphotropic phase boundary composition PZT (Zr/Ti=52/48, MPB-PZT) and the tetragonal PZT (Zr/Ti=30/70, Tetra-PZT). Among all the compositions, the MPB-PZT has the largest piezoelectric constant [7]. Micro actuators, such as micro mirrors [8-13] and variable optical attenuators (VOAs) [14-16], usually employ the MPB-PZT to realize large displacement. The Tetra-PZT has lower piezoelectric constant. However, since the Tetra-PZT has much lower dielectric constant, this type of PZT is mainly used for self-driving sensors [17] and energy harvesters (EHs) [18-24]. The output voltage would be higher because of the lower dielectric constant.

Unfortunately, the deposition of PZT thin film requires very high temperature for sintering and annealing processes. Even with the help of nanocrystalline composite

technique, the sintering temperature could still be as high as 600 – 700 °C [25]. Hence, the PZT material is not compatible with CMOS process. Some key properties of PZT are given as follows:

- Dielectric constant: ε = 500 (Tetra-PZT) and 1500 (MPB-PZT);
- Piezoelectric coefficient: d_{31} = 40-50 (Tetra-PZT) and 70 – 110 (MPB-PZT);
- High electromechanical coupling factor: k^2 = 7 – 15%;
- High temperature process;
- Not compatible with CMOS process.

1.1.3 Other materials

Similar to AlN, ZnO is also with a wurtzite crystal structure. This piezoelectric material have been used for BAW devices [26, 27] and integrated into micro sensor in early times [28]. Due to its small bandgap (~3eV) and the inherent risk of increased conductivity, ZnO is gradually replaced by AlN (~6eV) now. As ZnO can be deposited at room temperature, for some low temperature applications such as flexible devices on polymer substrate, ZnO is still used [29-34].

PVDF as a polymer is a flexible piezoelectric material. The PVDF has relatively high piezoelectric constant (d_{31}=5) and is easy to deform. Leveraging on its flexibility and piezoelectric effect, a wind based EH is developed [35]. This PVDF EH can start working at a very low wind pressure.

1.2 Basic Physics of Ultrasound

Leveraging on the piezoelectric effect and MEMS technology, a number of piezoelectric MEMS ultrasonic devices are presented in this thesis. Understanding the fundamental of ultrasound is helpful to design appropriate devices. A brief physics of

ultrasound will be introduced in this section.

1.2.1 Background

Ultrasound is a mechanical vibration at a frequency above audible range (>20kHz). The frequency range of ultrasound could be from kHz to GHz. Since ultrasound wave is a mechanical wave, a medium is compulsory for ultrasound to propagate through. The medium can be gas, liquid or solid. Based on the particle oscillation direction, the ultrasound waves can be divided into two categories: the longitudinal wave (along the propagation direction) and the shear wave (transverse to the propagation direction). Only solids can support both longitudinal and shear waves. In the case of liquid, most liquids cannot easily support the shear wave and the supporting capability of shear wave increases with their viscosity. For air, only longitudinal wave can propagate through it.

1.2.2 Acoustic impedance

Acoustic impedance is defined as the ratio of acoustic pressure and the particle motion speed at a certain point in the medium. For a plane wave, the acoustic impedance Z can be described as:

$$Z = \rho \cdot c \tag{1.1}$$

where ρ is the medium density and c is the sound speed in this medium. Usually the gas has extremely small acoustic impedance, while the solid has very large acoustic impedance. The acoustic impedance of liquid should be somewhere in between. The acoustic impedance is very important in characterizing the propagation of ultrasound

waves. The densities, sound speeds and acoustic impedances of several common ultrasound media are summarized in Table 1.1 [36]. The parameters are also shown in Figure 1.2 for easier visualization.

Table 1.1 Summary of densities, sound speeds and acoustic impedances of ultrasound media

Medium	ρ (kg/m^3)	c (m/s)	Z (MRayl)
Air	1.2	333	0.0004
Water	1000	1480	1.48
Soft tissue	1070	1542	1.65
PZT	7600	2800	21.28
Silicon	2329	8433	19.64

1.2.3 Reflection and transmission

A propagating ultrasound wave will be partially reflected at the interface of two media. The reflection coefficient is determined by the acoustic impedance difference of the two media.

$$\frac{p_r}{p_i} = \frac{Z_2 \cos\theta_i - Z_1 \cos\theta_t}{Z_2 \cos\theta_i + Z_1 \cos\theta_t} \tag{1.2}$$

where p is the acoustic pressure, Z is the acoustic impedance, and θ is the angle. The i refers to the incident wave, r refers to the reflected wave, and t refers to the transmitted wave. Similarly, the transmission coefficient is obtained as:

$$\frac{p_t}{p_i} = \frac{2Z_2 \cos\theta_i}{Z_2 \cos\theta_i + Z_1 \cos\theta_t} \tag{1.3}$$

The ultrasound transmission obeys the Snell's Law:

$$\frac{c_1}{c_2} = \frac{\sin\theta_t}{\sin\theta_i} \tag{1.4}$$

where the c is the sound speed in medium.

An acoustic impedance mismatch may result in a large reflection. Therefore for some applications a matching layer or other methods are applied, in order to minimize the impedance mismatch and increase the transmission [37-39].

1.2.4 Ultrasound intensity

The ultrasound intensity is defined as the time average flow of ultrasound energy through a unit area:

$$I = \frac{1}{T}\int_0^T pu\,dt \tag{1.5}$$

where p is the ultrasound pressure, u is the particle speed and T is the time period. Since the acoustic impedance Z is the ratio of ultrasound pressure to particle speed, the ultrasound intensity can be calculated as:

$$I = \frac{p^2}{2Z} \tag{1.6}$$

1.2.5 Attenuation

A propagating ultrasound wave will be attenuated in medium due to absorption and scattering. For most materials, the ultrasound attenuation A in dB is linearly proportional to the ultrasound frequency f, as described in Eq. 1.7.

$$A\ (\text{dB}) = \alpha \cdot f \cdot l \tag{1.7}$$

where l is the propagating distance of the ultrasonic wave. Table 1.2 summarizes the attenuation coefficients of several ultrasonic media.

Table 1.2 Summary of attenuation coefficients α

Medium	Attenuation coefficients (dB/MHz·cm)
Air	1.64
Water	0.0022
Soft tissue	0.8

It is clearly shown that air has very large attenuation coefficient, and hence the ultrasound devices working in air usually have a very low frequency (<1MHz), to reduce the ultrasound attenuation.

1.2.6 Bandwidth

The -6dB fractional bandwidth is commonly adopted by researchers to describe the bandwidth of an ultrasonic transducer. This bandwidth is defined as:

$$BW = \frac{f_2 - f_1}{f_0} \times 100\%$$

where f_2 and f_1 are the frequences where the amplitude drops to half of maximum,

and f_0 is the central frequency.

1.2.7 Ultrasound safety

In general, ultrasound is safe to human and widely used for biomedical applications. However, as is mentioned above ultrasound wave is a mechanical wave, too high ultrasound may still be harmful to human bodies. High intensity ultrasound wave may damage the tissue by local heating and cavitation effect. Therefore the Food and Drug Administration (FDA) of U.S. recommends that the ultrasound intensity in human body should not exceed 720 mW/cm^2.

1.3 Piezoelectric Ultrasonic MEMS Devices

Typically there are two types of ultrasonic devices: the acoustic wave device with ultrasonic wave propagating within the device, and the ultrasonic transducer with ultrasound wave radiating into outer medium. Since the outer medium is liquid or air for most cases, the ultrasonic transducer is designed to generate and receive longitudinal ultrasonic wave. Meanwhile, acoustic wave device usually employs both longitudinal and shear waves, because the shear wave can be supported by solids.

1.3.1 Acoustic wave sensors (ultrasound within device)

Acoustic wave sensor is so called because it employs the inner propagating ultrasound wave as the sensing mechanism. With the ultrasonic wave propagating through or on the surface of the sensor, any perturbation on the propagation path affects the velocity and / or amplitude of the wave. Changes in velocity can be monitored by measuring the frequency of the sensor and can then be correlated to the corresponding physical or chemical quantity being measured.

Based on different propagating modes within the device, acoustic wave sensors can be generally divided into four categories:

- The Thickness Shear Mode (TSM) device;
- The Surface Acoustic Wave (SAW) device,
- The Acoustic Plate Mode (APM) device,
- The Flexural Plate Wave (FPW) or Lamb wave device.

Figure 1.2 shows schematic sketches of each type of acoustic sensors, while the side views and cross sections of four devices are shown in Figure 1.3.

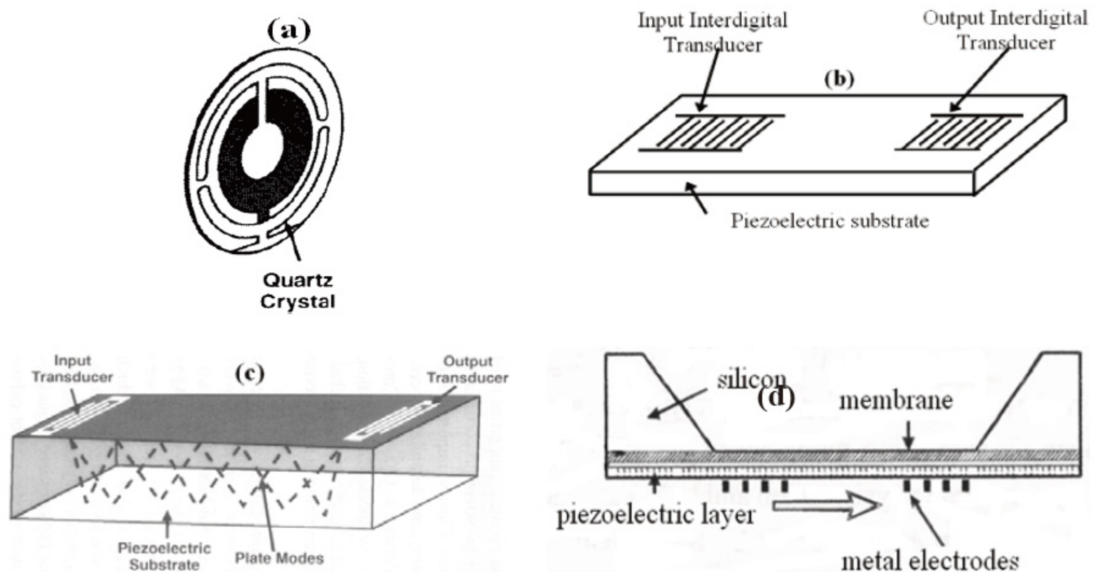

Figure 1.2 Schematic sketches of the four typical types of acoustic wave sensors: (a) the Thickness Shear Mode (TSM) device, (b) the Surface Acoustic Wave (SAW) device, (c) the Acoustic Plate Mode (APM) device and; (d) the Flexural Plate Wave (FPW) or Lamb wave device.

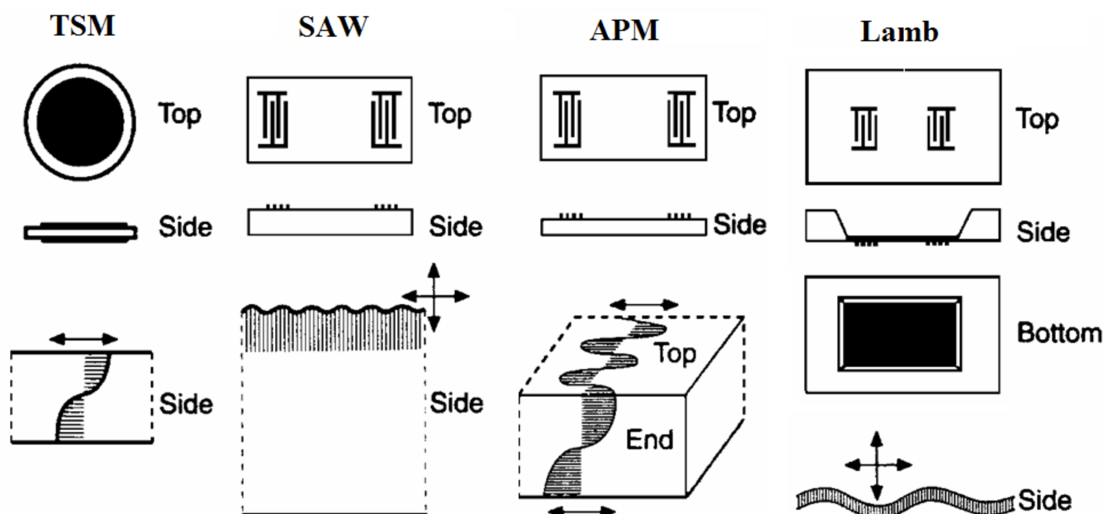

Figure 1.3 Comparison between the four types of acoustic wave devices.

SAW, or Rayleigh wave, is a unique acoustic mode where the ultrasound wave propagation is confined to the surface. In 1887, Lord Rayleigh discovered this wave mode of propagation and predicted the properties of SAWs in his classic paper [40]. The SAW contains a longitudinal and a shear motion component. Both components can couple with the medium which contacts the SAW device surface, shown in Figure 1.4. Such coupling strongly affects the amplitude and velocity of the SAW. This feature enables SAW devices to sense mass and mechanical properties directly, and SAW has the highest sensitivity among all acoustic wave sensors because all energy is confined within the surface. However, due to the vertical motion of the surface wave, an excessive attenuation of the surface wave is caused by leaking energy into liquid. Thus the SAW sensor may not be suitable for liquid sensing.

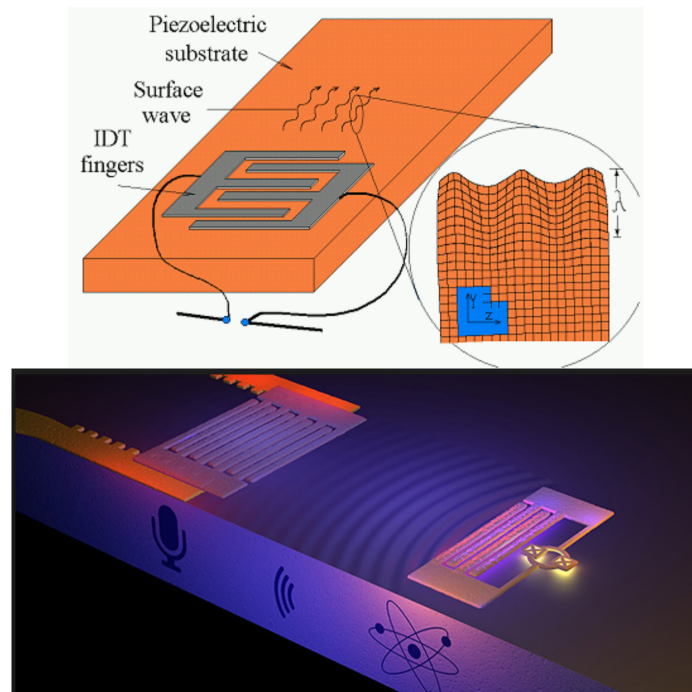

Figure 1.4 Surface acoustic wave (SAW) moves vertically in a direction normal to the surface plane. The energy is confined to the surface, and SAW sensor is very sensitive to device surface changes.

Another acoustic wave sensor, *i.e.* the Lamb wave sensor, is also noteworthy. Lamb wave sensor is firstly presented by R. M. White *et al.* in 1988 [41], in which an acoustic wave is excited in a thinned membrane with a thickness smaller than the propagating wavelength, shown in Figure 1.5. A unique feature of Lamb wave is that its phase velocity is lower than that of most liquids. When a Lamb wave sensor contacts or is immersed in a liquid, a slow mode of propagation exists, in which there is no radiation from the plate. Energy dissipation into liquid is minimized for Lamb wave, and thus it functions well in a liquid environment. Lamb wave sensor therefore is an ideal candidate for sensing in liquid [40, 42-46].

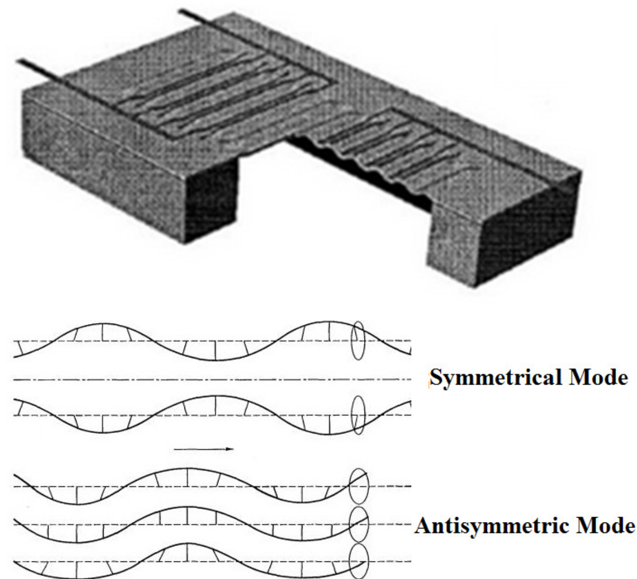

Figure 1.5 Illustration of a typical Lamb wave sensor with the two Lamb wave modes.

The acoustic wave sensors, including SAW and Lamb wave sensors, use a piezoelectric interdigital transducer (IDT) to generate and detect acoustic waves [47], as is shown in Figure 1.6. An oscillating electric field is applied to the IDT to deform the piezoelectric substrate (thick substrate for SAW and thin plate for Lamb wave), creating a mechanical wave. Excited acoustic wave then propagates through the substrate. When the acoustic wave arrives at another IDT, it deforms the piezoelectric substrate and is then converted back to an electric signal for measurement. It is worth noting that the wavelength λ of induced acoustic wave is directly determined by the IDT. For the lowest mode, its wavelength equals to the periodicity of IDT electrodes, shown in Figure 1.6 as well. Thus the expected wavelength of the acoustic wave sensor can be designed by changing the distance between two IDT electrodes.

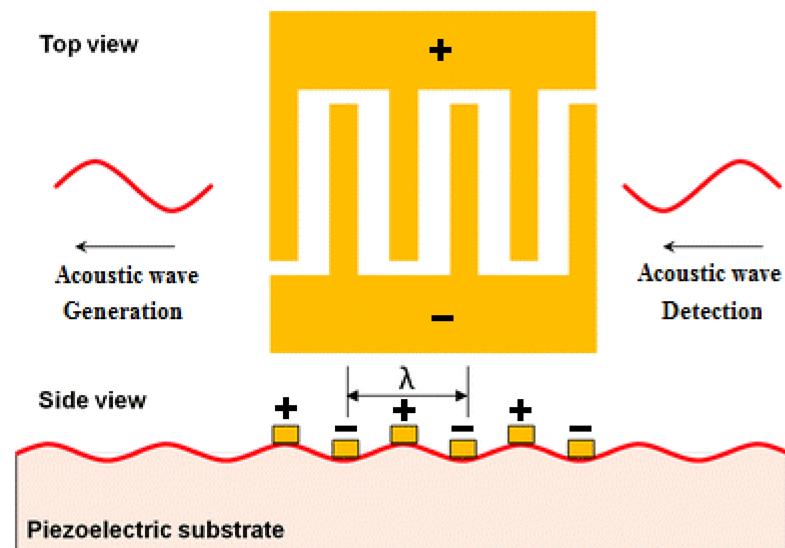

Figure 1.6 Illustration of the interdigital transducer (IDT) for acoustic wave generation and detection.

In this thesis, development of two acoustic wave sensors, *i.e.* SAW based pressure sensors and Lamb wave based viscosity and density sensors, will be presented and discussed in detail in Chapter 3 and 4, respectively.

1.3.2 Ultrasonic transducer (ultrasound outside device)

In addition to the previously discussed acoustic wave sensor, ultrasonic transducer (UT) is another type of ultrasonic device. Unlike the acoustic wave device, ultrasonic wave generated by the UT is transmitted into outer medium, *e.g.* air, water or human body. Transmitted ultrasonic wave is received by another UT after reflection, refraction and scattering in the medium. Interesting information or parameters about the medium can then be extracted from the time, frequency, phase and amplitude of received ultrasonic wave.

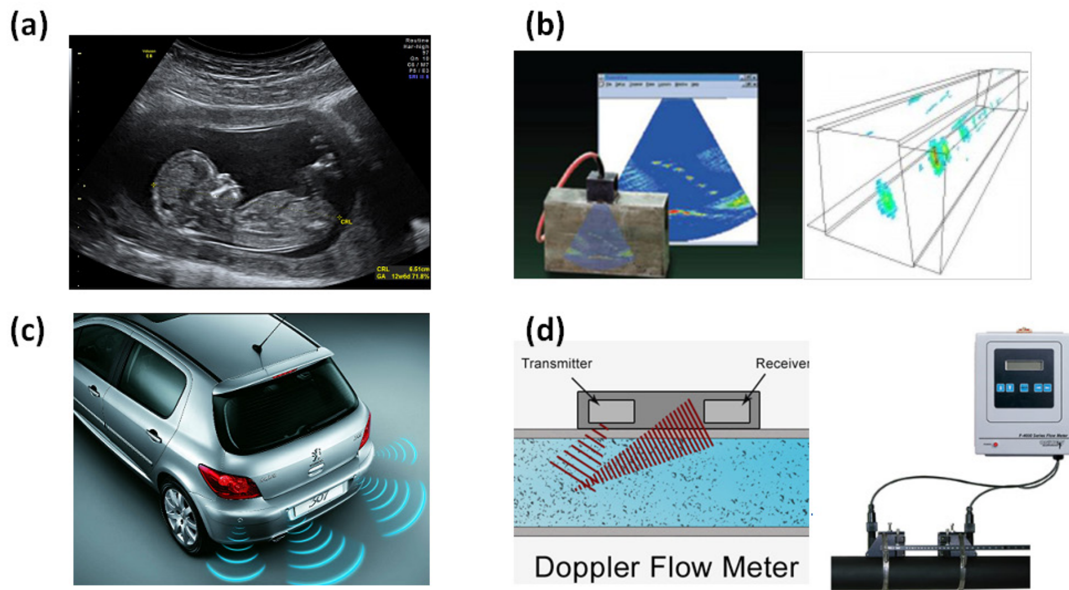

Figure 1.7 Typical applications using ultrasonic transducers (UTs): (a) B-mode diagnostic ultrasonic imaging; (b) non-destructive flaw testing; (c) reserve parking sensor and; (d) liquid flow rate sensing.

Various applications are realized with the ultrasonic transducers, such as B-mode ultrasonic imaging, nondestructive testing (NDT), reserve parking sensor, and liquid flow rate sensing, shown in Figure 1.7. Combined the ultrasonic imaging with flow velocity sensing, information about the blood flow rate in the heart can be extracted and provided to doctors [48]. Basically there are three types of UT: bulk piezoelectric UT (conventional UT), capacitive micromachined ultrasonic transducer (cMUT) and piezoelectric micromachined ultrasonic transducer (pMUT).

1.3.2.1 Bulk piezoelectric ultrasonic transducer

Figure 1.8 Commercially available conventional UTs for various applications: (a) diagnostic ultrasonic imaging, (b) NDT and (c) range finding.

The conventional UT has dominated the markets for decades. The currently available ultrasonic applications such as diagnostic imaging and NDT are all implemented using conventional UTs, shown in Figure 1.8. The conventional UT is usually made of rigid bulk piezoelectric ceramic. Compared to the ultrasound medium such as soft tissue, water or air, the rigid ceramic has much higher acoustic impedance. The commonly used PZT ceramic has an acoustic impedance of 21.28MRayl, while the acoustic impedance of soft tissue is only 1.65MRal. The acoustic impedance of air is even much smaller. As the consequence of such huge impedance mismatch, more than 90% of ultrasonic energy reflects back at the interface and cause large loss [49]. The bandwidth and sensitivity of the UT therefore is drastically reduced. Although a λ/4 impedance matching layer can improve the ultrasound transmission efficiency, the matching layer becomes too thin to be mechanically handled as frequency increases, and sometimes it is not even practical [50]. Another limitation comes from the fabrication of the conventional UT. The emerging 3-D diagnostic ultrasound imaging is of great interests, which requires a 2-D UT array with very small pixels and pitches. Unfortunately the conventional UT can hardly fulfil such requirements. Conventional UT is fabricated by mechanical dicing and assembly. Thus only 1-D array is available

because the complicated electrical connections for 2-D array are extremely challenging. The size of UT pixel and pitch already approach their limitation as well and can hardly be further reduced.

Researches on the micromachined ultrasonic transducers (MUTs) are growing rapidly in recent years. Leveraging on the advanced MEMS technology, the MUT can be of miniaturized dimension, lower cost and lower power consumption. In addition, MUT provides more design flexibility [50] and better acoustic impedance matching [51]. Unlike the conventional UT, the MUT employs a flexural membrane for generating and receiving ultrasound waves. Since the flexural membrane is much softer than rigid ceramic, its acoustic impedance is closer to the operation medium. Better impedance matching thus can be achieved without the matching layer, and its transmission efficiency is much higher than the conventional UTs [52]. The 2-D MUT array is also possible, as the photolithography process can easily realize very complicated electrical connections (multiple metal layers if necessary) for the 2-D array [53].

1.3.2.2 Capacitive micromachined ultrasonic transducer (cMUT)

The cMUTs have been well developed since 1994 [54, 55]. Figure 1.9 shows the typical structure of a cMUT element [56]. The cMUT element is a micro capacitor which contains a flexural metalized membrane and a ridged metalized substrate, with an extremely small gap in between. The flexural vibration is induced by the electrostatic attraction. When a DC voltage is applied to the electrodes, the membrane is attracted by the substrate and is deformed by the electrostatic force [57]. Ultrasonic wave is generated by the membrane oscillation with an AC voltage input. Reversely, if an ultrasonic wave hits the membrane and forces it to oscillate, the change in

distance results in the change of capacitance. The capacitance change can be readout by external circuits. Benefited from the flexural membrane, a much superior impedance matching is achieved and demonstrated by experimental results [52].

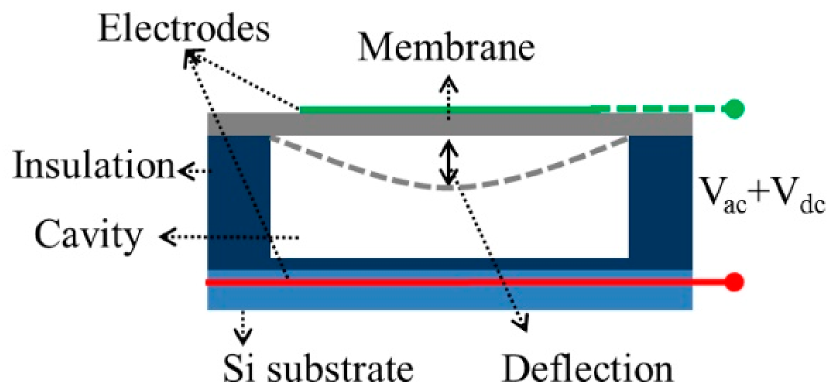

Figure 1.9 Typical cross-sectional structure of a cMUT [56].

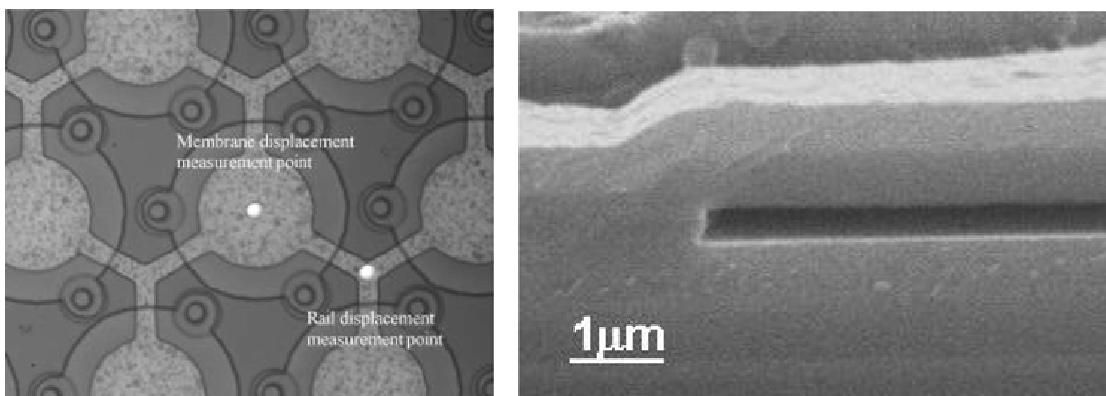

Figure 1.10 The SEM images of a cMUT array. cMUT employs an extremely small gap to maintain the performance [58].

Despite all the advantages of cMUT, several inherent drawbacks limit its future applications. The cMUT requires an extremely small gap under the flexural membrane to achieve acceptable sensitivity, as is shown in Figure 1.10. Fabrication of such small gap is complicated, expensive, and suffers from very low yield. In addition, the operation of the cMUT requires very high voltage bias, usually over 100V. Such

high voltage may bring safety issues for human body, especially for the implanted applications. The high voltage also limits its applications in portable devices. Moreover, the response of cMUT is highly non-linear, which requires sophisticated circuits for correction and signal processing.

1.3.2.3 Piezoelectric micromachined ultrasonic transducer (pMUT)

The pMUT, however, overcomes all the inherent drawbacks of cMUT [59-63]. Particularly, its operation voltage is lowered to only several volts [64, 65]. Hence, the pMUT seems like a promising candidate for practical applications, especially for portable electronics.

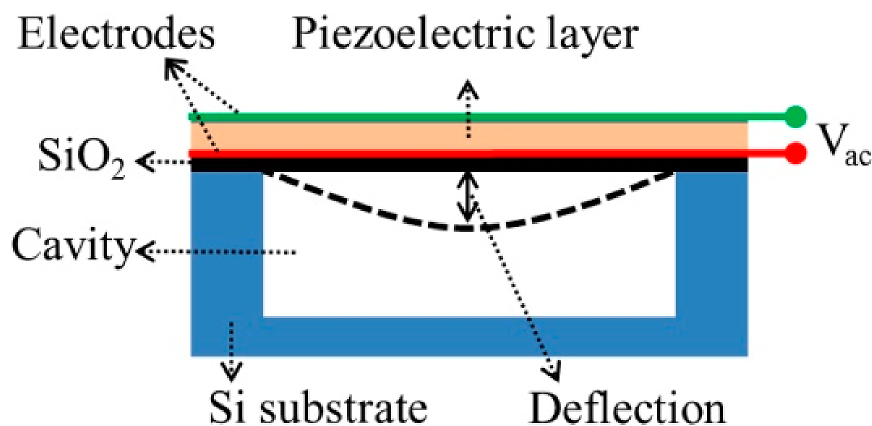

Figure 1.11 Typical cross-sectional structure of a pMUT [56].

Figure 1.11 shows the typical structure of a pMUT, where an active piezoelectric layer and a passive supporting layer (usually Si or SiO_2) are required. The pMUT works at d_{31} mode, whereas the lateral strain is induced by the piezoelectric effect, causing a stress mismatch between the piezoelectric layer and the supporting layer. The stress mismatch of the two layers thus forces the membrane to deflect around its neutral plane. It is important that the neutral plane must be outside the piezoelectric

layer by carefully choosing the materials and thicknesses. If the neutral plane falls into the piezoelectric layer, the piezoelectric strain will work against itself, and results in a very poor performance.

Varieties of novel applications are implemented using pMUTs. 2-D pMUTs array with very small pixel size and pitches are reported. High definition (HD) ultrasonic images can be real-time captured without physical scanning, shown in Figure 1.12 [53].

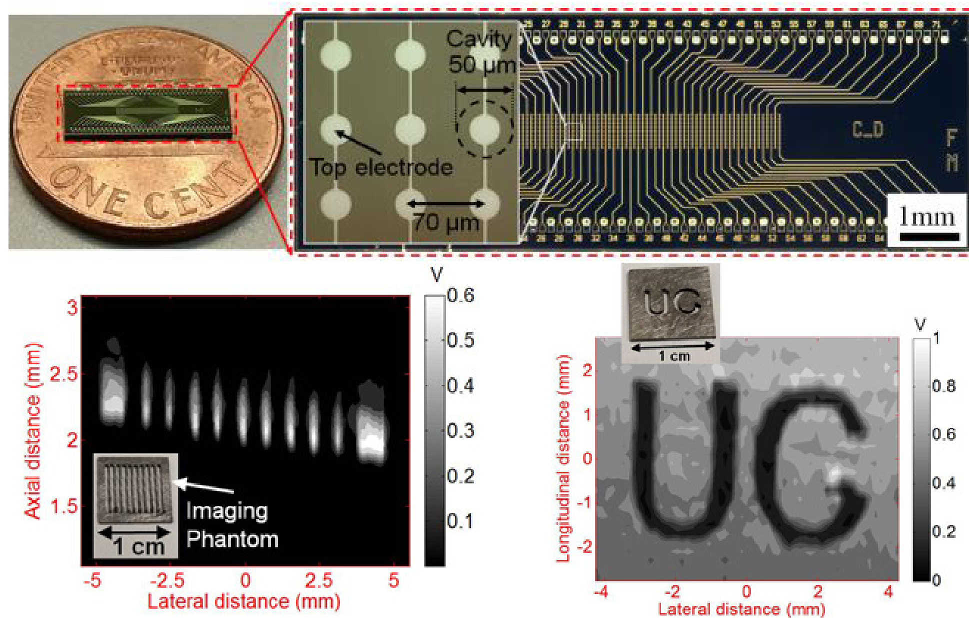

Figure 1.12 A recently reported 72*9 pMUT array and the HD ultrasonic images [53].

Besides the outside body imaging, a miniaturized high dense pMUT array is developed for forward-looking ultrasonic imaging inside the blood vessels. This pMUT array contains 1261 elements in a diameter of 1.23mm, which is 10 to 20 times higher than previously reported array, shown in Figure 1.13 (a) [66]. An ultrasound probe made of pMUT array (Figure 1.13 (b)) for intracardiac imaging is reported as well [67]. This probe shows the capability of acquiring real-time and *in-vivo*

ultrasonic images in the heart.

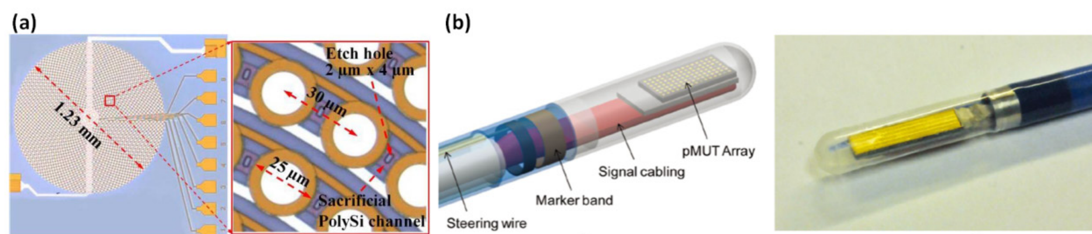

Figure 1.13 (a) A miniaturized high dense pMUT array with 1261 elements [66] and; (b) an intravascular imaging probe with pMUT array [67].

In addition to the imaging related applications, researchers have also demonstrated airborne gesture recognition using pMUT [68-71]. Photo swiping without touching the screen has been realized, as shown in Figure 1.14 (a). Since this pMUT can be integrated to portable devices such as mobile phone, the airborne gesture recognition may possibly be the next-generation interacting approach for electronic devices. Beyond that, pMUT array based 3-D range finder is also realized, which can simultaneously detect the hands and the head of a human.

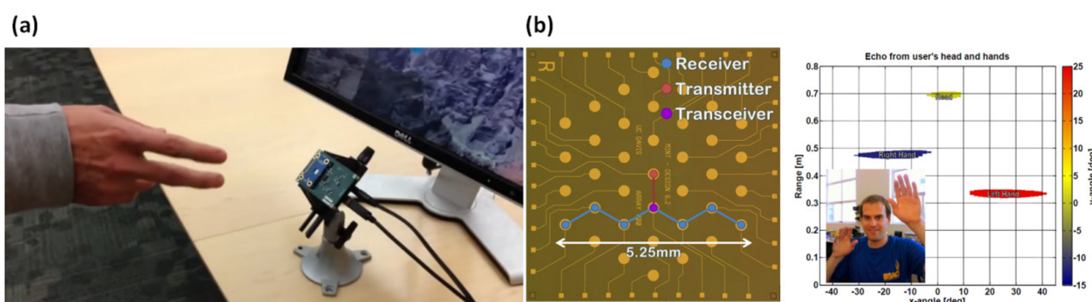

Figure 1.14 (a) Demonstration of airborne gesture recognition for photo swiping and; (b) 3-D range finding for targets detection [72].

Recently, another research group reports an ultrasonic fingerprint sensor also using pMUT array [73, 74]. The acquired fingerprint image is shown in Figure 1.15. Compared to current optical fingerprint sensors, pMUT sensor consumes significantly

lower power, which is of great value for extending the battery lifetime of portable electronics.

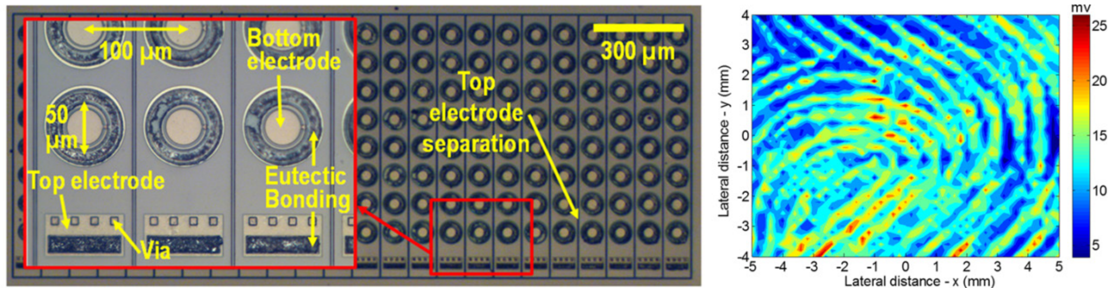

Figure 1.15 A recently reported ultrasonic fingerprint sensor using pMUT array [73].

pMUT shows its suitability for implantation to human body. In-*vivo* implantation of a tiny pMUT inside the middle ear is shown in Figure 1.16, which functions as audio prosthesis [75]. This pMUT is implanted near the oval window. Some researches are also done to further extend its suitability for implantation. A pMUT is successfully fabricated on a flexible substrate, and this flexible pMUT is definitely more friendly to human body [76].

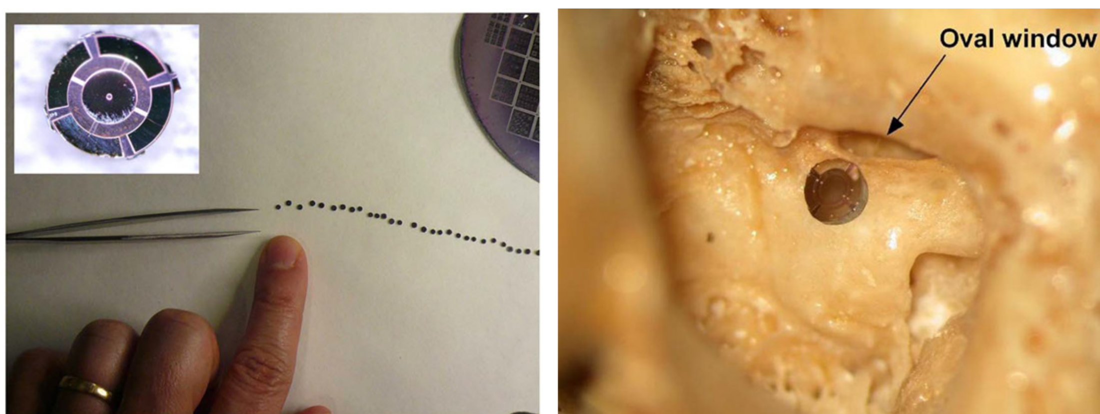

Figure 1.16 A tiny pMUT which functions as audio prosthesis is in-*vivo* implanted inside middle-ear [75].

Although pMUT shows all abovementioned advantages and potentials, it has several inherent limitations. Aiming to overcome these limitations, various pMUTs with different unique features are designed, fabricated and characterized, which will be presented and discussed in Chapter 4 to 7 in detail.

1.4 Thesis Organization

This thesis summarizes the various works on piezoelectric MEMS devices that were undertaken during my Ph.D. candidature. The content of each chapter in the thesis is as follows:

Chapter 2 summarizes the micro fabrication processes of all the presented piezoelectric MEMS devices. As the critical processes, deposition and etching of two piezoelectric thin films, i.e. AlN and PZT, are described in detail. The integrated fabrication process flow for each MEMS device is also described respectively.

Chapter 3 investigates a series of SAW based pressure sensors. Though there are many reported SAW based pressure sensors, the sensitivity mechanism of such sensors is still not very clear. The pressure sensors under investigation have different diaphragm shapes, and they exhibit largely different sensitivities. Using the finite element models, the diaphragm shape is found to influence the ratio of pressure induced longitudinal / lateral strains. Since the longitudinal and later strains have opposite contributions to overall SAW frequency shift (sensitivity), the diaphragm shapes thus largely changes the sensitivity by affecting the strain ratio. This study reveals the sensitivity mechanism of SAW based pressure sensor, and several possible approaches for enhancing the sensitivity are proposed as well.

Chapter 4 presents a Lamb wave based decoupled viscosity and density liquid sensor. Previously reported Lamb wave based viscosity and density sensor can only

measure the product of these two parameters, *i.e.* both viscosity change and density change equally contribute to the frequency shift of the sensor. To overcome this main limitation, the proposed decoupled Lamb wave sensor is designed to work at two unique modes: viscosity mode and density mode. Experimental results show that each mode is solely sensitive to viscosity or density change.

Chapter 5 provides two highly efficient pMUTs with enhanced transmitting sensitivity. Currently the reported pMUTs suffer from severe stress issue, which significantly suppresses the membrane displacement. The transmitting sensitivity thus is not satisfactory, and this is the main limitation of the pMUT. The first presented pMUT has a unique structure which helps to alleviate the stress issue. Its transmitting sensitivity is characterized as 450% higher than reference pMUT. The second design employs a perforated membrane, which enables a piston-like membrane motion. More medium can be pushed back and forth, and the transmitting efficiency is enhanced.

Chapter 6 presents a high performance pMUT using PZT thin film. Migrating from AlN thin film to PZT thin film, the pMUT sensitivity is significantly enhanced. In addition, the design parameters are optimized using finite element model. The fabricated pMUT shows superior sensitivity to previously reported PZT pMUTs.

Chapter 7 further develops an ultra-wide bandwidth pMUT based on the PZT thin film. Poor bandwidth is another main limitation of pMUT. Large bandwidth helps to achieve a high resolution ultrasonic image. By engineering the length / width ratio of the membrane, several resonance modes are simultaneously excited within a certain frequency range. The peaks are overlapped together to form an ultra-wide bandwidth of 94.7%, which is much wider than previously reported pMUTs.

Finally, the main contributions of this thesis and suggestions for future work are summarized in Chapter 8.

Chapter 2 Fabrication of Piezoelectric Ultrasonic MEMS Devices

The fabrication process is very critical for realizing a high performance piezoelectric ultrasonic MEMS device. As the functional layer, piezoelectric material directly determines the device performance. Therefore it is important to deposit piezoelectric thin films with high piezoelectric constant. Meanwhile, the fabrication process would largely affect the final piezoelectric constant of the piezoelectric material. Annealing and electric field poling can significantly enhance the piezoelectric constant, while some microfabrication process, *e.g.* deep reactive ion etching (DRIE), may degrade the constant. Hence, the process conditions and the sequence must be carefully chosen to ensure a high performance. Moreover, the residual stress of the piezoelectric material must be minimized. Large residual stress may induce the deflection or buckling of released structures, worsen the device performance, and even break the device. In the following sections, fabrication details of piezoelectric ultrasonic MEMS devices will be discussed. Various process considerations and optimization process will be introduced.

2.1 Piezoelectric Material Deposition

In this section, deposition of two piezoelectric materials, *i.e.* AlN and PZT thin film will be introduced and discussed.

2.1.1 Deposition of AlN thin film

2.1.1.1 Physical vapor deposition

The AlN thin film is deposited by DC pulsed sputtering. The deposition conditions used in this work are shown in Table 2.1.

Table 2.1 Sputtering conditions for AlN thin film deposition

Sputtering gas	Argon and Nitrogen (N_2), ratio 1:5
DC power	2kW to 8kW
Deposition temperature	350°C
Pressure	4mTorr

One critical parameter for AlN thin film growth is the supply of energy to the substrate [6]. This parameter can be adjusted by controlling the total pressure and the substrate bias voltage [77, 78]. To ensure the piezoelectric effect of AlN thin film, the energy to the substrate must be high enough so that the highly (002) oriented AlN thin film can be grown and the c-axis is perpendicular to the substrate surface. However, this energy should not be too high because too high energy may damage the deposited thin film, resulting in a poor crystal quality.

It is worth noting that a high (002) orientation does not guarantee a good piezoelectric effect. In some cases, the AlN film with a very good crystal quality exhibits a very poor piezoelectric response [79]. This could be attributed to the grains with opposite piezoelectric polarization in the deposited thin film [80]. If the energy to the substrate is slightly lower than the value for growing pure (002) oriented AlN thin film, such grains with opposite piezoelectric polarization is likely to appear even the crystal quality is very good. Therefore, the energy should be carefully adjusted.

The deposited AlN thin film is shown in Figure 2.1. It is clearly shown that the AlN thin film is highly (002) oriented, and the full width at half maximum (FWHM)

of the x-ray diffraction (XRD) rocking curve is measured as less than 1.5°.

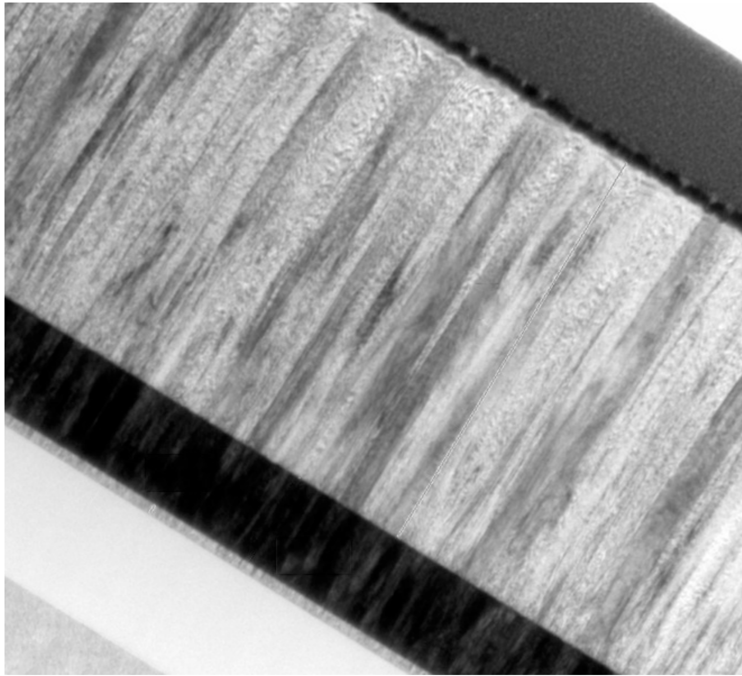

Figure 2.1 Cross-sectional SEM image of deposited AlN thin film using sputtering.

2.1.1.2 Stress control

Large residual stress may result in performance degradation of the ultrasonic MEMS devices. For the acoustic wave sensors, the stress significantly influences the sound speed and hence changes the device frequency unexpectedly. In addition, the stress can also drastically suppress the sensitivity of pMUT [81]. Therefore, minimized residual stress of the AlN thin film is desirable.

The residual stress of AlN thin film after deposition has been well studied [82]. Besides the deposition conditions, the residual stress of AlN thin film is largely dependent on its thickness [83]. The in-plane residual stress increases with the thickness, and the sign is changed from negative (compressive stress) to positive (tensile stress) at certain film thickness. As is shown in Figure 2.2, the AlN thin film

deposited on metal exhibits different stresses. The residual stress changes its sign at about 1μm thickness, where the residual stress becomes zero. A nearly stress-free AlN thin film thus may be possible via controlling the thickness. In this work, the AlN thin film deposition is controlled to 1.2μm. By adjusting other deposition conditions, a nearly stress-free AlN thin film is finally achieved with cross-wafer residual stress of +/-50MPa.

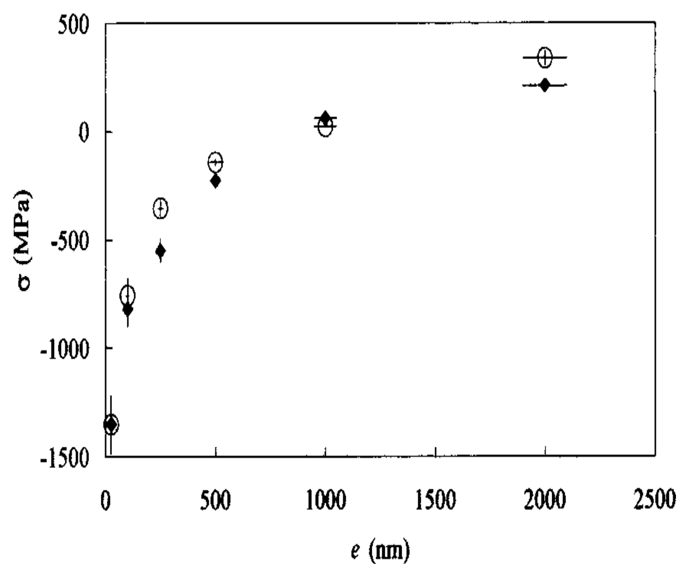

Figure 2.2 Measured residual stress of deposited AlN thin film as a function of thickness [83].

2.1.2 Deposition of PZT thin film

2.1.2.1 Sol-gel method

The sol-gel method is often used for PZT thin film (> 1μm) deposition, due to its simplicity and excellent reproducibility [84-87]. In this work, a commercially available PZT solution (PZT-20; Kojundo Chemical Co, Japan) is used as a precursor solution. Since the MPB-PZT has the largest piezoelectric coefficient [88], the PZT

solution with Zr/Ti=52/48 is adopted to maximize the device performance. This PZT solution is firstly spin-coated onto the substrate at 500rpm for 3s, 3200rpm for 20s and 6000rpm for 2s. The deposited film is dried by heating at 120°C for 2 minutes, and then pyrolyzed at 250°C for 5 minutes. After the pyrolysis, the PZT thin film is crystallized using rapid thermal annealing (RTA) at 650 °C for 2 minutes, with the ramping rate of 100°C/s. To achieve a relatively thick PZT thin film, multi-coating process is necessary. Previous studies indicates that the film quality through layer-by-layer crystallization is much better than that through single-crystallization [89]. Therefore, the spin-coating, drying, pyrolysis and RTA step are repeated for 16 times. A 2μm MPB-PZT thin film is finally achieved.

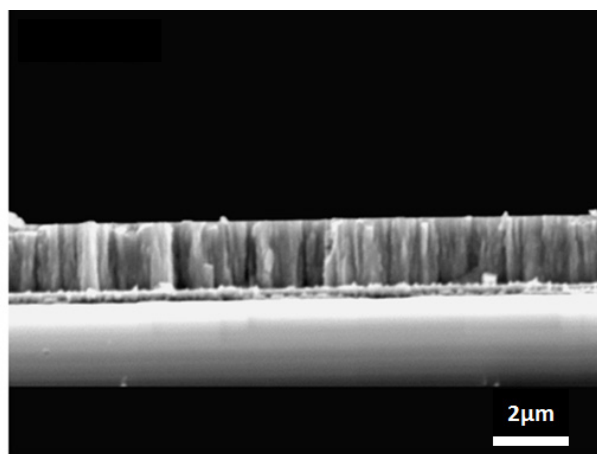

Figure 2.3 Cross-sectional SEM image of deposited PZT thin film

2.1.2.2 Electric poling

For the PZT thin film deposited by sol-gel method, its final piezoelectric constant d_{31} is mainly determined by the electric poling process because the initial d_{31} is very limited. Usually a DC electric field of 10–100 kV/cm is applied to the PZT thin film for about 5 minutes as the electric polling. According to previous study, this

step is suitable after completion of all fabrication processes [90], since the d_{31} after polling could be drastically lowered by the following processes [91].

Recently, a unipolar pulse poling process for PZT thin film is developed [92]. The pulse poling process is found to be much more effective than the conventional DC poling, resulting in a much higher d_{31} coefficient. Figure 2.4 (a) shows the employed waveform of the unipolar pulse poling signals (1 kHz triangle voltage pulse with interval of 0.1s for 10 times). To evaluate the behaviors of PZT thin films after poling, the piezoelectric coefficients d_{31} are derived as described in [92]. Figure 2.4 (b) compares the d_{31} of the 2μm MPB-PZT thin films after DC poling and pulse poling. The DC poling voltage is limited to 20V to avoid the breakdown of PZT thin film. For the pulse poling, however, the extremely short duration can hardly induce the PZT breakdown. Thus, the poling voltage can be much higher than the DC poling. The measured d_{31} of MPB-PZT reaches its maximum of 105pm/V with pulse poling at 100V, which is significantly higher than the DC poling (78 pm/V). In addition to the piezoelectric coefficient, the dielectric loss is also important as lower dielectric loss is always desirable. Benefited from the short duration, the high voltage pulse poling does not increase the dielectric loss of MPB-PZT but further reduce it. The minimum dielectric loss of 0.06 is achieved with pulse poling at 100V.

The Tetra-PZT thin film is also shown as the reference. The Tetra-PZT thin films show lower d_{31} for both DC and pulse poling, and its performance starts to degrade at 60V. At such higher voltage, cracks form in the Tetra-PZT thin film, resulting in the d_{31} dropping and the significantly increased dielectric loss. The MPB-PZT does not suffer from such performance degradation, and shows highest d_{31} and lowest dielectric loss at 100V. Hence, the MPB-PZT thin film with 100V pulse poling is adopted to realize the high performance ultrasonic MEMS devices.

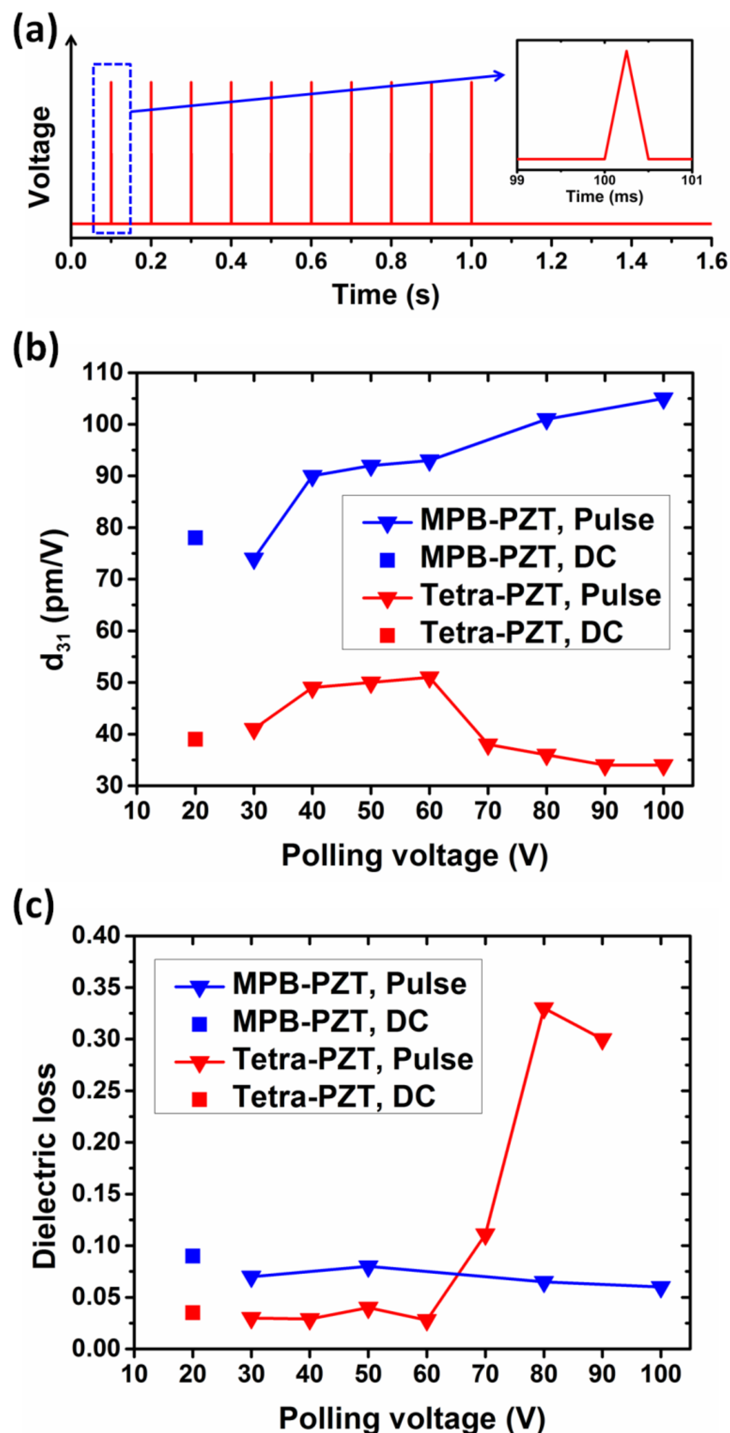

Figure 2.4 The waveform of unipolar pulse poling signals. This waveform is 1 kHz triangle voltage pulse with interval of 0.1s for 10 times; (b) The measured piezoelectric constant d_{31} of the PZT thin films after DC poling and pulse poling and; (c) The measured dielectric loss of the PZT thin films after DC poling and pulse poling.

2.2 Piezoelectric Material Etching

2.2.1 AlN thin film etching

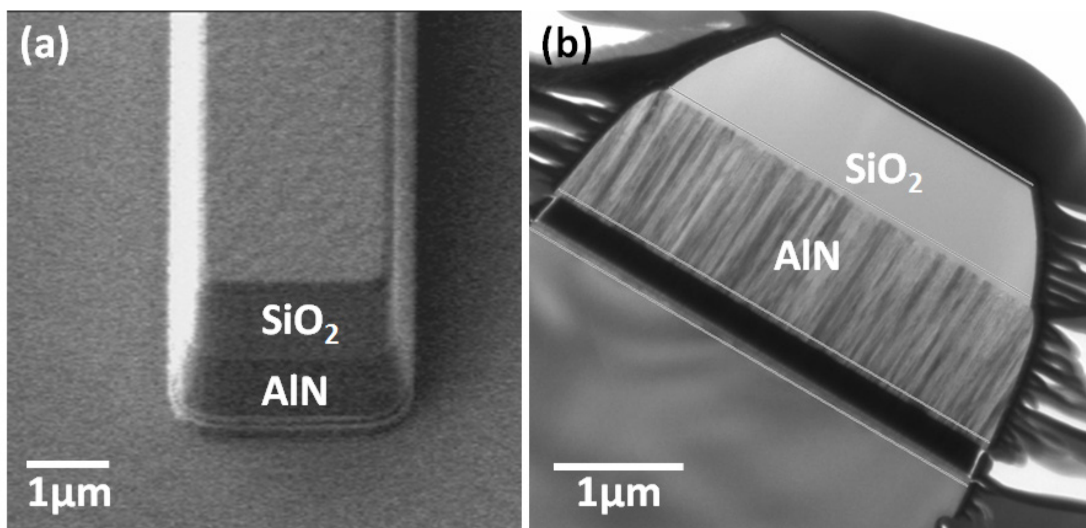

Figure 2.5 (a) The SEM image of the etched AlN thin film using SiO_2 as hard mask and; (b) cross-sectional view.

Wet etching is available for AlN thin film, by using hot phosphoric acid (60°C to 90°C) [93, 94]. However, due to its high chemical stability, the etching rate of AlN thin film could be very slow. For sputter-deposited high quality AlN thin films, the etching rate can be as low as 14nm/min. Therefore, reactive ion etching (RIE) technique is employed to etch the AlN thin film in this work, via physically ion bombardment with chemical to assist this process. The chlorine is used as the etchant, because aluminum fluoride is a non-volatile compound and extremely stable. The etching rate of AlN thin film is achieved at 0.23μm/min in BCl_3 plasma with a small percentage addition of Ar/N_2. In order to achieve a good profile, a plasma enhanced chemical vapor deposition (PECVD) SiO_2 layer is employed as the hard mask. Figure 2.5 shows the etched AlN thin film with SiO_2 hard mask.

2.2.2 PZT thin film etching

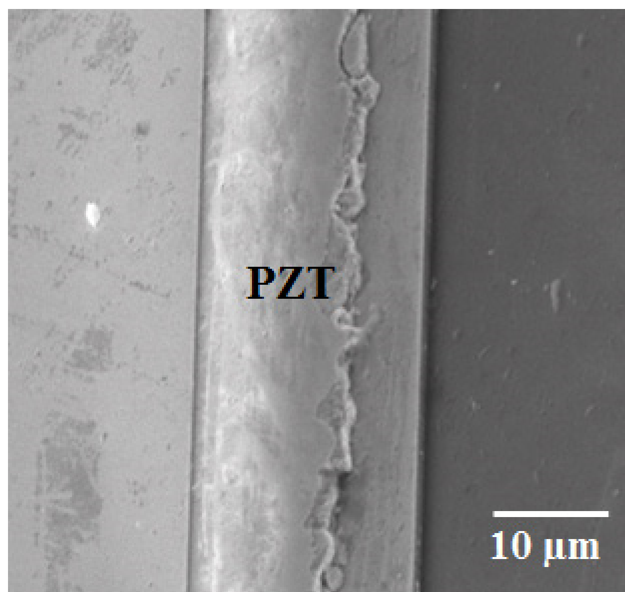

Figure 2.6 The SEM image of PZT thin film after wet-etching. The edge is zigzagged because the HCl tends to rapidly attack PZT along the grain boundaries.

Unlike the stable AlN, PZT thin film can be easily wet-etched by strong acids. The HCl based etchant is observed to dissolve PZT thin film very fast while it is safe to the photoresist. It is worth noting that HCl tends to rapidly attack PZT thin film along the grain boundaries and consequently the film edges after etching is zigzagged. To alleviate this unfavorable phenomenon, HF is added to the etchant solution. In this work, the PZT thin film is etched by a mixture of HF(0.9%)/HCl(8.2%)/H_2O(90.9%) at room temperature. However, a water in-soluble white residue (PbClF) is left due to the presence of HF. Such residue is removed by short exposure to HNO_3(50%)/H_2O(50%) solution. Figure 2.6 shows the PZT thin film after wet-etching. It is clearly shown that the edge is zigzagged because of the HCl in the etchant.

2.3 Integrated Fabrication Process Flow

The deposition and etching of piezoelectric materials have been discussed in previous sections. In this section, the integrated fabrication process flow will be described. The integrated process flows are divided into two categories based on the diaphragm releasing methods.

2.3.1 Backside deep-reactive ion etching (DRIE)

Backside deep-reactive ion etching (DRIE) is commonly used for the MEMS device releasing process. Except for releasing the functional diaphragm, the backside DRIE also create the channel for the sensors to be exposed to the environment. Usually the buried oxide (BOX) layer of silicon-on-insulator (SOI) wafer serves as the etching stop layer, because of the high etching selectivity of SiO_2. After the frontside process is completed, the hard masks are patterned using backside RIE. 1μm SiO_2 and 2μm photoresist (PR) serve as the hard mask. With the support of another dummy wafer attached on the frontsidee, the backside DRIE process is then completed by using high power etching tool. Two gases are used for the Bosch DRIE process: SF_6 and C_4F_8. SF_6 is used as the etchant for isotropic etching of silicon during one cycle, and C_4F_8 is used to form a Teflon-like passivation layer to protect the side wall during the other cycle. In this work, the acoustic wave sensors and PZT based pMUT are fabricated with backside DRIE releasing.

2.3.1.1 Acoustic wave sensors

The fabrication process sequence of the acoustic wave sensors are illustrated in Figure 2.7. Fabrication starts from an 8” SOI (100) wafer. This wafer is with 50μm (for SAW sensor) or 30μm (for Lamb wave sensor) silicon device layer, 1.4μm buried

oxide (BOX) layer and 600µm thickness handle silicon layer. Initially sputtering is used to grow an AlN piezoelectric layer (1.2µm for SAW sensor and 2µm for Lamb wave sensor) on the SOI wafer with a deposition rate of 50nm/min. Then a metal layer (Mo or Al) is deposited by e-beam evaporation and patterned to form IDT electrodes by RIE. After the front side process, the wafer is thinned down to a thickness of 400 µm by mechanical grinding. Next, a 1µm PECVD SiO_2 layer is deposited on the backside of the wafer as hard mask for release process, which is patterned by RIE. The Si substrate was etched by deep DRIE down to the BOX layer to release the membrane structure. Finally, the SiO_2 hard mask was removed using wet etching.

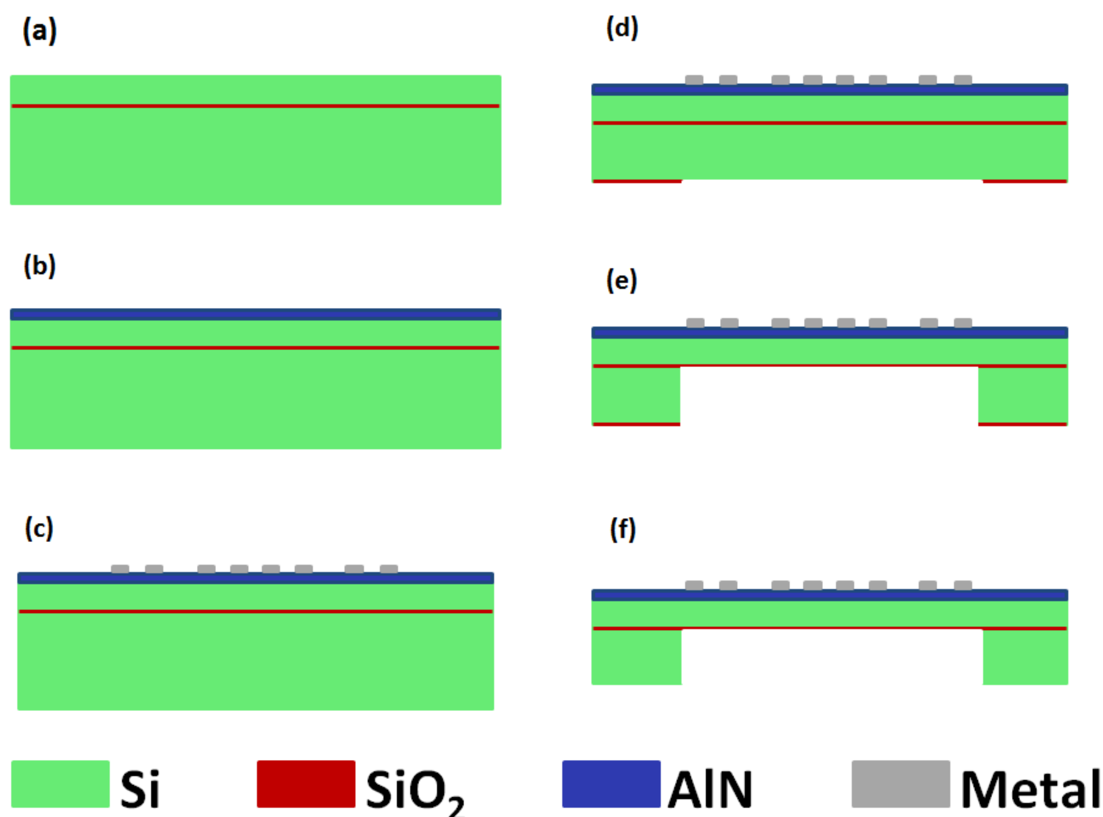

Figure 2.7 Fabrication process flow of the acoustic wave sensor: (a) SOI substrate with 30µm or 50µm device silicon layer; (b) deposition of AlN layer using sputtering;

(c) metal layer (Al or Mo) deposition and pattering to form IDT electrodes; (d) wafer thinning to 400μm, followed by 1μm SiO_2 hard mask deposition and pattering on backside; (e) backside Si DRIE release; (f) SiO_2 hard mask removal by wet etching.

2.3.1.2 PZT based pMUT

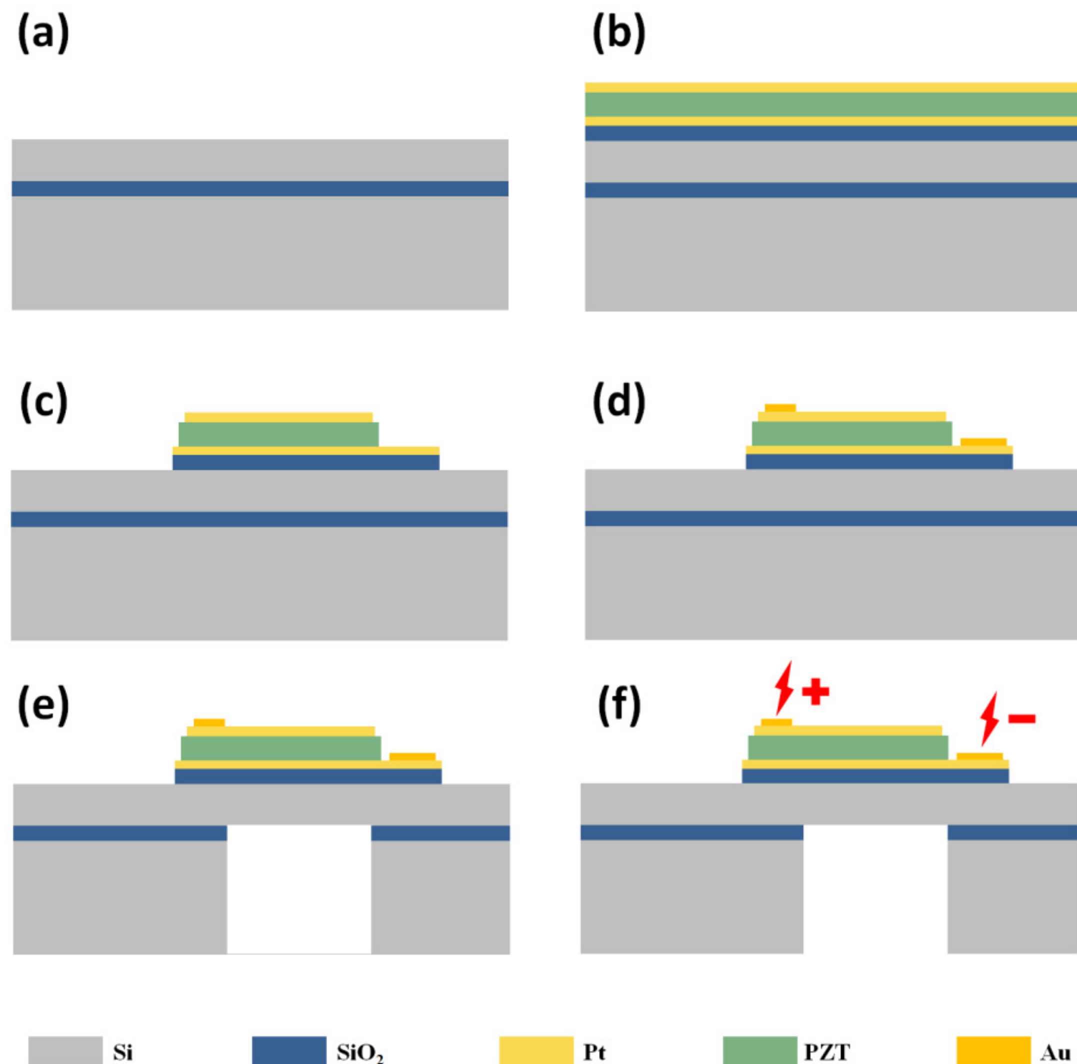

Figure 2.8 Fabrication process flow of the device: (a) SOI substrate with 5μm or 10μm device silicon layer and 400 μm handle silicon layer; (b) deposition of 1μm SiO_2/10nm Ti/200nm Pt/2μm MPB-PZT/10nm Ti/200nm Pt stack. The PZT thin film is deposited by sol-gel method, followed by RTA at 650°C for crystallization; (c) patterning of the stack. Ar ion milling, wet etching and RIE are for metal, PZT and SiO_2, respectively; (d) Au (100nm) wire bonding pads formation; (e) backside Si

DRIE to release the flexural membrane and; (f) pulse poling of PZT thin film at 100V.

The micro-fabrication starts from an SOI wafer, which has 5µm or 10µm device silicon layer, 1µm BOX layer and 400µm handle silicon layer, shown in Figure 2.8 (a). A 1µm SiO_2 thin film is firstly grown on the wafer for isolation. Prior to bottom electrode deposition, a 10nm Ti adhesion layer is applied. The Pt (200nm) bottom electrode is then deposited by DC magnetron sputtering. After that, the MPB-PZT thin film is deposited using sol-gel method [89]. A commercially available PZT solution is used as a precursor solution, where the Pb/Ti/Zr composition is 120/52/48. This PZT solution is spin-coated onto the wafer, followed by heating at 120°C and 250°C for drying and pyrolyzing. RTA at 650 °C is then applied for 2 minutes to crystallize the PZT thin film. The deposition, pyrolysis, crystallization processes are repeated by 16 times to form 2µm PZT thin film. Top electrode is formed by sputtering Pt (200nm)/Ti (10nm) on the PZT surface. Figure 2.8 (b) shows the deposited multilayer stack. The stack is patterned as shown in Figure 2.8 (c), using Ar ion milling, wet etching and RIE for etching the Pt/Ti, PZT and SiO_2, respectively. To form the wire bonding pads, a 100nm Au is deposited by DC magnetron sputtering and patterned by wet etching (Figure 2.8 (d)). Finally the flexural membrane is released by removing Si substrate and BOX from backside surface using DRIE as shown in Figure 2.8 (e). The poling process is after all the microfabrication steps are finished, in order to maintain the best piezoelectric performance. The 100V unipolar pulse poling voltage is applied to each device via the bonding pads for 1s, shown in Figure 2.8 (f).

2.3.2 Cavity SOI wafer

Cavity SOI wafer is a special SOI wafer with customized cavities predefined

under the BOX layer using photolithography. The released diaphragm by predefined cavities has a much better accuracy than that of backside DRIE. Moreover, the pitch of diaphragms can be very small for cavity SOI wafer, and therefore a pMUT array with high pixel density is possible. The vacuum cavity also serves as a functional structure to enhance the pMUT performance, which will be discussed in Section 5.1 in detail. All AlN based pMUTs are fabricated using cavity SOI wafer.

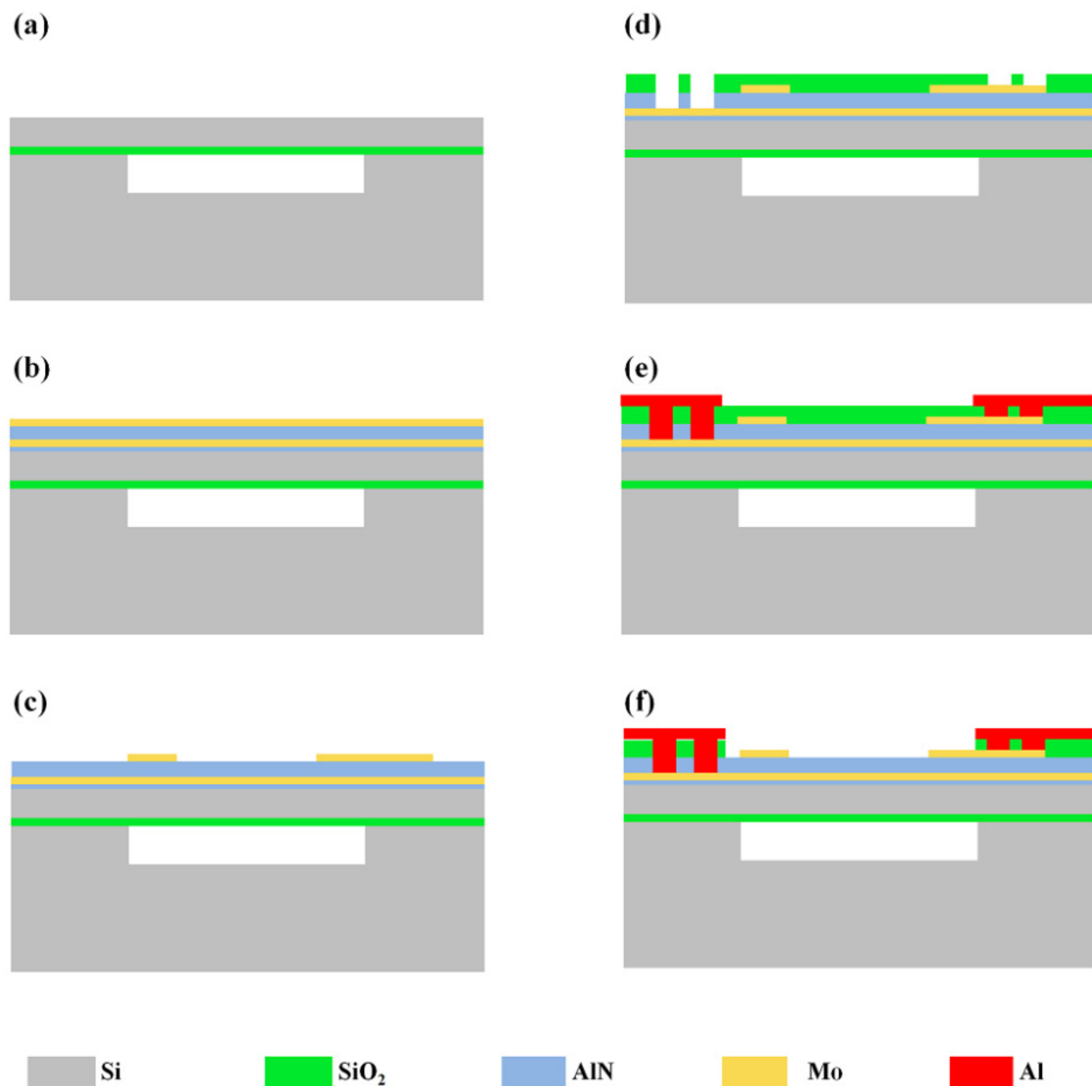

Figure 2.9 Fabrication process flow of the AlN based pMUT: (a) Formation of the cavity SOI wafer; (b) Deposition of Mo / AlN / Mo stack; (c) Patterning of top Mo layer; (d) Deposition of PECVD SiO_2 for isolation, and SiO_2 and AlN are etched to open contact via (bottom). The contact via (top) is then opened by etching SiO_2; (e) Deposition and patterning of Al metal layer for electrical connections and to form

bonding pads and; (f) Blank etching of oxide by RIE.

The fabrication of the AlN based pMUT starts from a commercially purchasable cavity SOI wafer. Square-shaped cavities are firstly defined in the handle wafer using photolithography. The depth of the cavities is 5μm. Then the cavity SOI wafer is formed by bonding the handle wafer with a 5 μm device Si wafer in vacuum, shown in Figure 2.9 (a). Prior to the deposition of Mo/AlN/Mo stack, a 20 nm AlN seeding layer is deposited by atomic layer deposition (ALD). This seeding layer helps to reduce the surface roughness of AlN layer, and consequently helps to improve the film quality of top Mo layer. Next the PVD is used to deposit the 0.2μm Mo / 1.2μm AlN / 0.2μm Mo stack on the AlN seeding layer, shown in Figure 2.9 (b). The top Mo layer is patterned using a 0.2μm PECVD SiO_2 layer as the hard mask. This hard mask is removed after Mo patterning using HF wet etching (Figure 2.9 (c)). A layer of 0.7 μm PECVD SiO2 layer is then deposited for isolation. This SiO_2 is firstly etched by RIE, followed by AlN anisotropic dry etching to open the bottom-to-top contact via. Then the SiO_2 layer is etched to open the top-to-top via, shown in Figure 2.9 (d). Subsequently, a 0.7 μm Al is deposited and patterned to form the electrical connections and bonding pads (Figure 2.9 (e)). Finally the oxide is blank etched by RIE dry etching to thin the membrane, shown in Figure 2.9 (f). As the selectivity of SiO2 and Al is very high, no obvious attack to Al layer is observed after the process.

It is noted that additional etching holes are applied to the membrane for the pMUT introduced in Section 5.2. For this type of pMUT, additional SiO_2 hard mask is deposited and patterned after the process shown in Figure 2.9 (e), and then the membrane is etched through. The hard mask is removed by blank etching using RIE, similar to Figure 2.9 (f).

Chapter 3 SAW Based MEMS Pressure Sensor

Pressure sensor is the most widely used MEMS device in the market [95]. Several harsh environment application areas, like automotive, aeronautic and oil-drilling industry, desire to have miniaturized pressure sensors with low power consumption, improved sensitivity and stability at high temperature and high pressure environment [96-102]. However, MEMS based sensing technology for such applications is not readily available; hence pressure sensor for harsh environment is gaining increasing research interest recently. Traditional silicon based piezoresistive pressure sensor can barely be employed in high temperature environment due to severe degradation in its accuracy and sensitivity [103]. Though SiC based pressure sensor for high temperature (> 300°C) application has been demonstrated, the accuracy is not satisfactory at high temperature and the cost is considerably high [104, 105]. Another approach for high temperature operation falls on quartz based resonators, which have been popularly used as high pressure sensors in harsh environment for a long time [106, 107]. However, quartz based resonator still suffers from considerable performance degradation due to the piezoelectric coefficient loss for temperature higher than 250°C [108]. Alternatively, AlN based acoustic wave pressure sensor has been reported to provide high stable performance at high temperature [109], and the piezoelectric coefficient of AlN remains relatively unaffected with increasing temperature. In addition, AlN is a CMOS compatible material and so enables high volume batch fabrication with potentially low cost as it can be monolithically

integrated with sensors and IC [110]. However, the temperature induced frequency drift is still significant in these devices, which may largely affect the sensor accuracy. In order to eliminate the adverse effect of temperature on the sensor performance, a dual mode acoustic wave pressure sensor has also been reported [111]. By temperature cancellation from the two modes, very accurate and solo pressure readout is achieved. Hence, AlN based acoustic pressure sensor is proven to be stable, accurate, and a low-cost solution, especially for high temperature applications.

Besides the high temperature, high pressure is another concern for harsh environment applications. To fulfill the high pressure requirement, previously reported AlN based acoustic pressure sensors employ relatively thick diaphragm. For the pressure sensing range of 300 PSI or even higher, thick diaphragms of 30μm or 50μm are used and this adversely affects the sensitivity of these devices. [111]. Therefore, to enhance the sensitivity of such pressure sensors is in great demand. Unfortunately, the study of the sensitivity mechanism of AlN based acoustic wave pressure sensor for harsh environment applications has not been reported to date.

In this chapter, AlN based SAW pressure sensors with different diaphragm shapes are developed, packaged and characterized. The sensors with circular and rectangular (small aspect ratio) diaphragms are found to provide positive pressure coefficient of frequency (PCF), while the sensor with rectangular diaphragm (large aspect ratio) shows negative PCF. Acoustoelastic effect plays a critical role in this pressure sensitivity difference. Longitudinal and lateral strains along SAW propagating direction have opposite contributions to the frequency change, and hence the sensor with rectangular diaphragm (large aspect ratio), which is laterally strained, shows the negative PCF. Approaches to further improve the sensitivity of AlN based SAW pressure sensors for harsh environment are also included in this chapter.

3.1 Design of SAW Based Pressure Sensor

3-D illustrations of the AlN based SAW pressure sensor is shown in Figure 3.1 (a). AlN thin film is adopted as the piezoelectric layer and the bottom Mo electrode helps to increase the electromechanical coupling efficiency. A set of IDT electrodes (50 pairs) made of Mo with 10.4μm periodicity is used for inducing SAWs. Propagating SAWs are reflected by the two Bragg reflectors placed on either side of the IDT electrodes and this gives rise to resonant modes. The 50μm thick supporting silicon layer aims to fulfill the high pressure requirement. To study the influence of diaphragm shape on sensitivity, three different pressure sensors are designed: circular diaphragm with diameter of 800μm (PS_A), rectangular diaphragm with size of 1000μm × 800μm (PS_B) and rectangular diaphragm with size of 2700μm × 800μm (PS_C). The three sensors share the same resonator design but different diaphragm shapes. Corners of rectangular diaphragm are rounded to avoid the high localized stress, making the sensors more reliable.

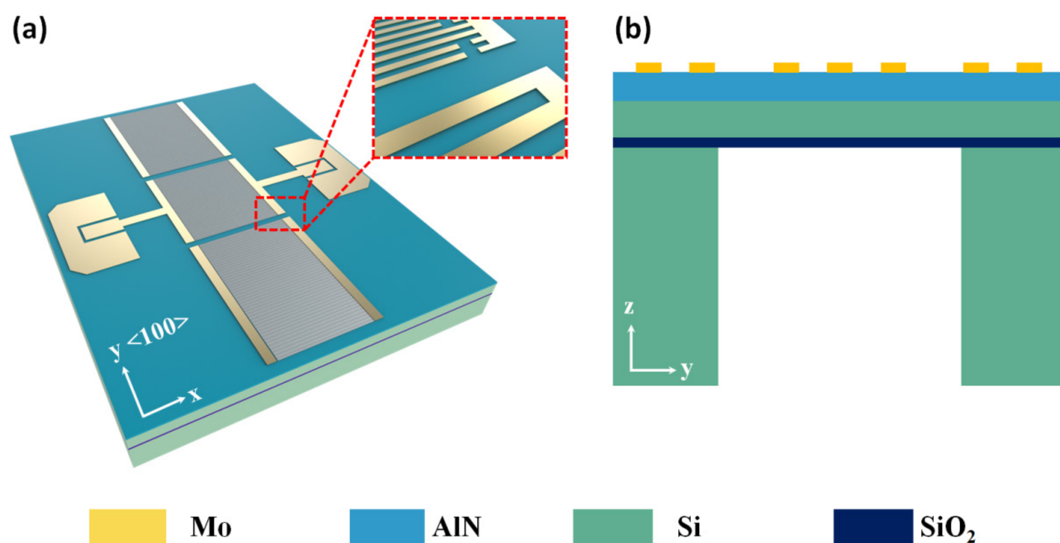

Figure 3.1 (a) The 3-D schematic illustration of the AlN based SAW pressure sensor; (b) Cross-sectional view of the illustration. All the devices are fabricated on (100) wafer and the SAW propagating direction is along <100>.

3.2 Device Characterization and Results

3.2.1 Device characterization

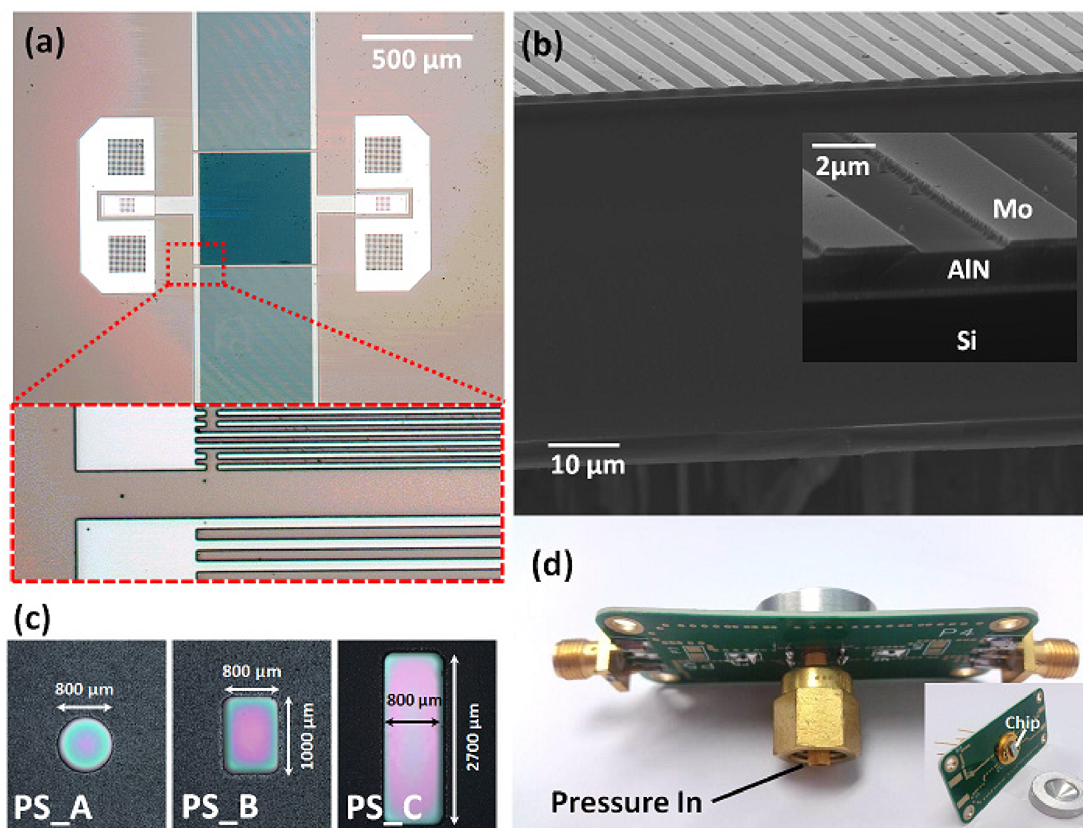

Figure 3.2 (a) Optical microscope (OM) image of fabricated pressure sensor; Secondary electron microscope (SEM) images, showing the 50µm thick silicon layer; (c) Backside view of the three pressure sensors showing the different diaphragm shapes and; (d) Packaged and assembled pressure sensor with printed-circuit-board (PCB) for testing. The pressure is applied using hydraulic controller through the tube and the SMA connectors are for signal readout.

The as-fabricated pressure sensors are shown in Figure 3.2 (a) – (b). Figure 3.2 (c) shows the backside cavities and the differently shaped diaphragms. The fabricated

pressure sensors are then packaged and assembled with printed-circuit-board (PCB) for testing as shown in Figure 3.2 (d). Since the pre-defined wavelength by IDT is 10.4μm, which is 1/5 less than the thickness of diaphragm (~56μm), SAW is expected to be induced.

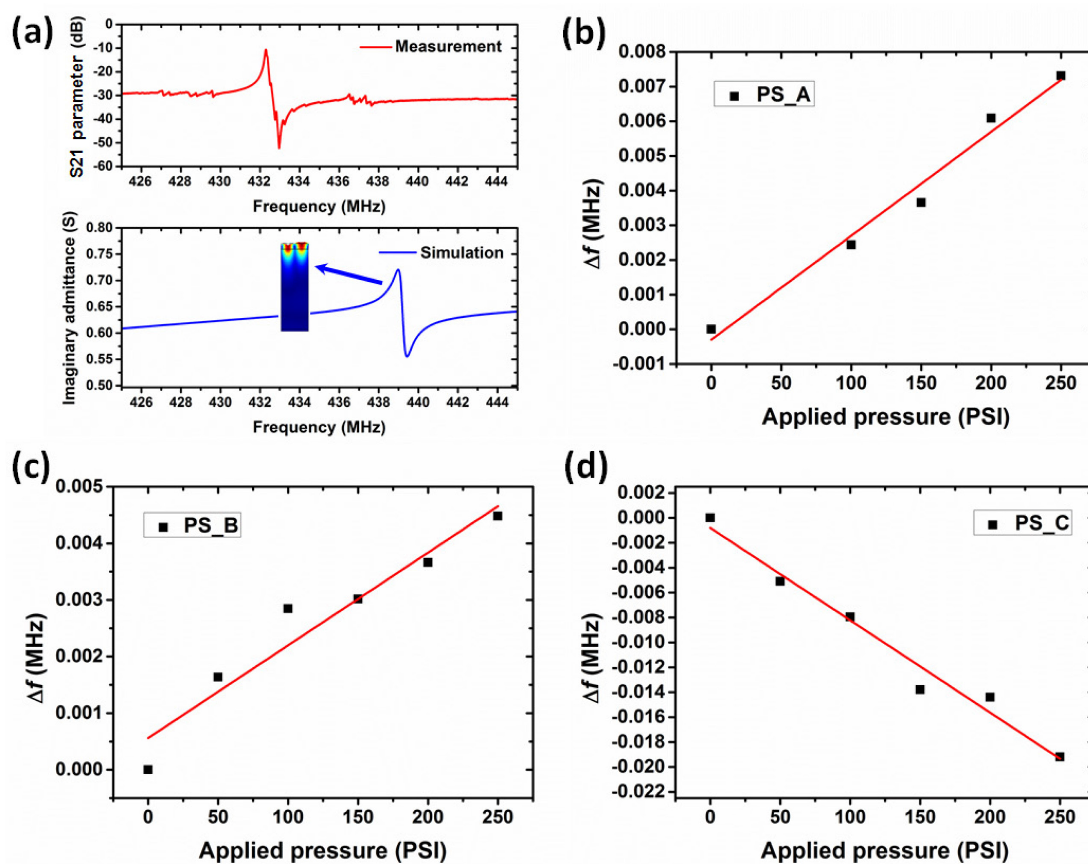

Figure 3.3 (a) Measured and simulated frequency responses of the pressure sensor. The mode shape indicates the induced acoustic wave is a SAW and; (b) – (d) The frequency change with respect to applied pressure for PS_A, PS_B and PS_C, respectively.

Agilent E5071B network analyzer is employed to measure the S parameters. Short-Open-Load-Through (SOLT) method is performed before testing to calibrate out the parasitic parameters introduced by PCB and bonding wires. The S21 parameter of the pressure sensor is extracted first and shown in Figure 3.3 (a).

Because the pressure sensors share the same resonator design, their behaviors without applying pressure are the same. This pressure sensor resonates at 432.29 MHz. Considering the pre-defined wavelength of 10.4μm, the phase velocity of the acoustic wave is derived as 4495.8 m/s. Such low velocity implies that the induced acoustic wave is a SAW, *i.e.* Rayleigh wave, which is expected [111]. A 2-D finite element analysis (FEA) model is also built by COMSOL Multiphysics software, using the Piezoelectric Devices model with Frequency Domain study. The simulated imaginary admittance of the resonator is shown in Figure 3.3 (a) as well, where the resonant frequency is 438.97 MHz and slightly higher than the measured result. The mode shape clearly shows that the induced acoustic wave is a SAW, and most of the displacement is confined within the depth of one wavelength near the surface.

3.2.2 Pressure testing

Pressure is applied to the sensors from backside using hydraulic pressure controller from 0 to 250 PSI. Even though the sensors function well at pressure over 700 PSI, a relatively lower pressure is applied to minimize the sensitivity change due to non-linear effects. Frequency changes with respect to the applied pressure are recorded and plotted in Figure 3.3 (b) to (d). The PCFs are derived as 0.071 ppm/PSI (30.02 Hz/PSI), 0.038 ppm/PSI (16.36 Hz/PSI) and -0.171 ppm/PSI (-74.13 Hz/PSI) for PS_A, PS_B and PS_C, respectively. The sensitivity behaviors of the three sensors seem quite different. PS_A and PS_B have positive PCFs while PS_C has negative PCF, and PS_A is more sensitive than PS_B.

3.3 Study of the Diaphragm Shape Effect on Sensitivity

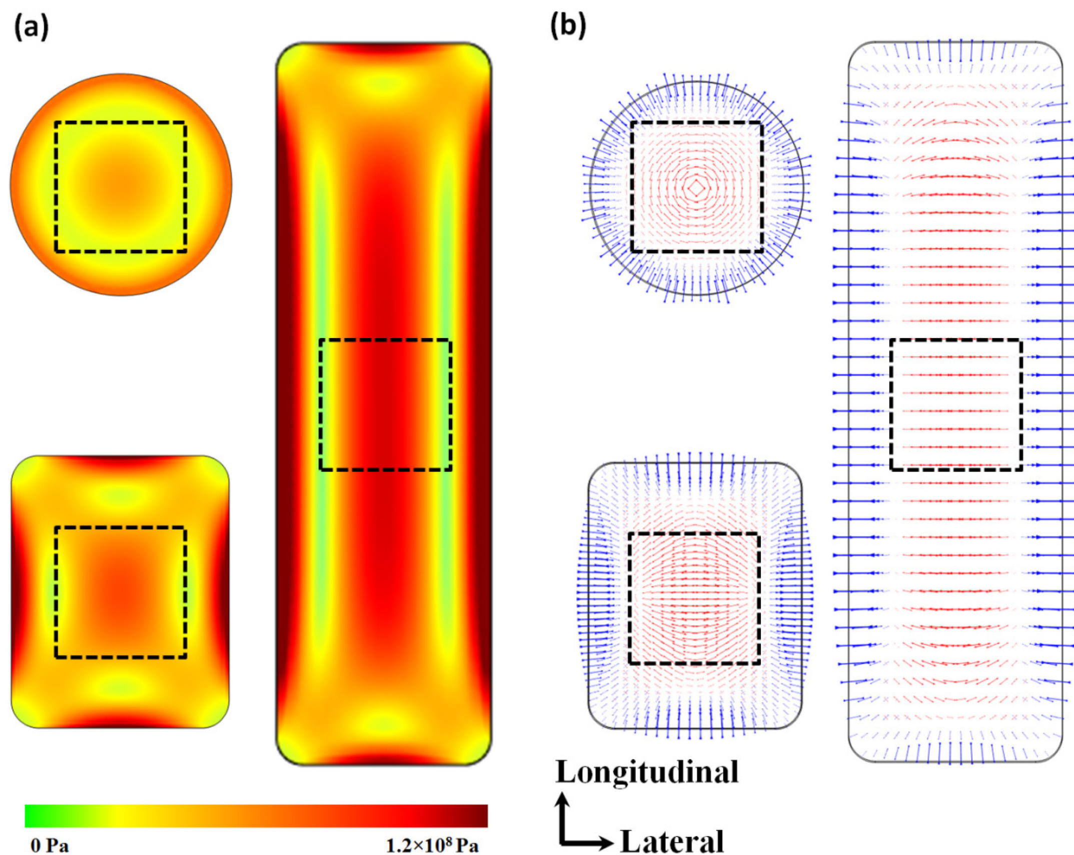

Figure 3.4 (a) Simulated Von Mises stress distributions of the three pressure sensors and; (b) The associated strain directions of the three pressure sensors. The dash lines indicate where the IDTs are located.

To investigate the mechanism behind such different sensitivity behaviors, another FEA model (Structural Mechanical Model) is built, and all the diaphragms are applied with 250 PSI pressure. The Von Mises stress distributions are shown in Figure 3.4 (a), and the associated strain directions are shown in Figure 3.4 (b). Since only the portion of diaphragm near the top surface displaces when SAW is propagating, the stresses and strains on the top surface are considered because they primarily affect the SAW phase velocity. Red and blue arrows represent for the tensile and compressive strains, respectively, and the dash lines indicate where the IDTs are located. It is clearly

shown that the IDTs in all three devices are bearing the same type of strain, *i.e.* the tensile strain. Thus, the negative PCF for PS_C should not be due to the type of strain. Furthermore, PS_A shows less strain than PS_B, and hence the higher PCF of PS_A should not be due to larger strain. Thus, the measured PCF variation for different diaphragm should be attributed to other non-obvious effects.

The frequency of a SAW resonator can be described as:

$$f_{SAW} = \frac{v_{ph}}{\lambda} \tag{3.1}$$

where, v_{ph} is the phase velocity and λ is the wavelength of the SAW. For the wavelength, which is determined by IDT periodicity, it may slightly change because of the strain. As all three pressure sensors are bearing tensile strain, the elongation in IDT will only result in a lower resonant frequency. However, both of PS_A and PS_B show a positive PCF, implying that the wavelength change may not be the major effect, but the phase velocity effect dominates the frequency change. In order to take the initial strain into account and obtain the phase velocity of SAW, a form of equations of motion is used as [112]:

$$\frac{\partial}{\partial x_i}[\sigma_{ik}u_{j,k} + T_{ij}] = \rho\frac{\partial^2 u_j}{\partial t^2} \tag{3.2}$$

Considering a piezoelectric medium, this equation becomes [113]:

$$\sigma_{ik}u_{j,ki} + c_{ijkl}u_{k,li} + e_{kij}\varphi_{,ki} = \rho\frac{\partial^2 u_j}{\partial t^2} \tag{3.3}$$

$$e_{ikl}u_{k,li} + \epsilon_{ik}\varphi_{,ki} = 0 \tag{3.4}$$

where T is the stress, σ is the initial stress, u the mechanical displacement, ρ the density , c the elastic moduli, e the piezoelectric moduli, ϵ the permittivity tensors and φ the electric potential. The subscripts i,j,k,l take on the values 1,2,3. Since acoustoelastic effect plays an important role in the phase velocity change, strain induced elastic moduli change must be considered. Thus the higher-order elasticity is introduced, and the stress-strain relation becomes non-Hookean as [114]:

$$\sigma = c\varepsilon + \frac{1}{2}c'\varepsilon^2 \tag{3.5}$$

where σ is the stress, ε the strain, c the linear elastic moduli and c' the third-order elastic moduli. The effective elastic moduli thus are strain-dependent and vary with increasing strain, changing the phase velocity. It is worth noting that the third-order elastic moduli of AlN can be ignored, because the bonds between crystallites in a thin polycrystalline film are very weak [115]. The third-order elastic moduli of Si, however, are very important and must be taken into consideration. Although the density of medium changes with strain as well (due to volume change), such effect only has minimum effect on the phase velocity based on previous study [113]. Hence, it is reasonable to neglect the density effect for our work.

Koleshko *et al.* have done a comprehensive study of strain effect of AlN based SAW device on silicon substrate [116]. Abovementioned set of equations are solved with boundary conditions using numerical method. Because silicon is a highly

anisotropic material and its third-order elastic moduli are anisotropic as well [117], the strain effect on phase velocity depends on the crystallographic plane of silicon wafer, direction of SAW propagation and direction of applied strain *etc.* The phase velocity after strain v_{ph} is defined as:

$$v_{ph} = v_0(1 + \gamma\varepsilon) \tag{3.6}$$

where v_0 is the phase velocity with zero strain, and a coefficient γ is introduced to describe the velocity sensitivity to strain. Since all the pressure sensors in this work are fabricated on a (100) Si wafer, the computation results for (100) Si plane is summarized in Table 3.1. The longitudinal strain means a homogenous uniaxial tensile strain applied along with the direction of SAW propagation, while the lateral means a tensile strain perpendicular to the direction of SAW propagation. As is shown in Figure 3.1, the SAW propagates along <100> direction for all the pressure sensors. For such case the longitudinal and lateral strains have opposite effects on the SAW phase velocity, *i.e.* longitudinal strain increases the velocity (γ = 0.8) while lateral strain decreases the velocity (γ = -0.3) as shown in Table 3.1. This could be the reason for different sensitivity behaviors of these sensors.

Table 3.1 Phase velocity sensitivity to strain γ for (100) Si plane [116]

SAW Propagation Direction	Longitudinal Strain	Lateral Strain
<100>	0.8	-0.3
<110>	1.9	0.3

The strain directions of the three pressure sensors are shown in Figure 3.4 (b). For the axially symmetric circular diaphragm (PS_A), it is equally strained in longitudinal and lateral directions. Due to the larger γ for longitudinal strain, the combined strain effect for PS_A is to increase the phase velocity, showing a positive PCF. Lateral strain effect cancels part of longitudinal strain effect, and results in lowering of the positive PCF compared to the one that only has longitudinal strain effect. The square diaphragm has the similar situation as the circular one, which also bears longitudinal and lateral strains of equal value. However, if the diaphragm is changed to rectangular shape, the strain starts becoming more lateral (PS_B). More lateral strain means the more significance of the cancellation effect. Though the combined strain effect still contributes to the increase of the velocity and frequency, PS_B shows a lower PCF than that of PS_A. As the aspect ratio of rectangular diaphragm increases, more region of diaphragm experiences the lateral strain (PS_C). It is clearly shown that the IDT of PS_C is entirely laterally strained, and thus only lateral strain effect attributes to its velocity change. Without the longitudinal strain effect, PS_C therefore shows a negative PCF. It is worth noting that the absolute PCF of PS_A is lower than that of PS_C. This could probably be due to the following reasons: 1. PS_C has larger diaphragm and larger strain for same applied pressure; 2. longitudinal strain induced elongation of IDT periodicity decreases the frequency of PS_A, which partially cancels the strain effect on velocity (increasing frequency), while on the other hand the lateral strain does not affect the IDT periodicity of PS_C and; 3. almost all strain for PS_C contributes to frequency decrease, while only half the induced strain in PS_A is longitudinal and contributes to the increase of the frequency.

3.4 Methods of Sensitivity Enhancement

As is discussed above, the frequency change of pressure sensor is attributed to different effects. These effects may work against each other and result in a relatively low sensitivity. Enhancing the primary effect and minimizing the reverse effect may result in further increase in the sensitivity without sacrificing the diaphragm thickness, *i.e.* the high pressure sensing range. For axially symmetric diaphragm design (PS_A), in-plane tilting the position of the IDT and reflectors by 45° and generating SAW propagating along <110> direction can help to increase the PCF. In this case, the velocity sensitivities to longitudinal strain and lateral strain become 1.9 and 0.3, respectively. The lateral strain does not cancel the effect of longitudinal strain but slightly enhances it, giving rise to a larger frequency change. Another possible approach is rotating the diaphragm of PS_C by 90°. The pressure induced strain becomes entirely longitudinal, resulting in a large positive PCF without cancellation from lateral strain effect. Finally, Table 3.2 summarizes the γ for (110) silicon plane. As the lateral strain does not change the IDT periodicity and affect the frequency for PS_C, if the silicon wafer is changed to (110), the maximum negative PCF may be achieved.

Table 3.2 Phase velocity sensitivity to strain γ for (110) Si plane [116]

SAW Propagation Direction	Longitudinal Strain	Lateral Strain
<110>	1.8	-1.1
<100>	0.9	-0.05

3.5 Summary

In conclusion, the influence of diaphragm shape on sensitivity of AlN based SAW pressure sensor is experimentally studied. Three pressure sensors with same SAW resonator design but different diaphragm shapes are fabricated, packaged and characterized. The sensors with circular diaphragm, rectangular diaphragm with small aspect ratio and rectangular diaphragm with large aspect ratio have PCFs of 0.071 ppm/PSI, 0.038 ppm/PSI, and -0.171 ppm/PSI, respectively. Diaphragm shape influences the longitudinal / lateral strain ratio. Longitudinal and lateral strains have opposite effects on phase velocity and frequency change for (100) silicon plane along <100> propagation direction, and so results in different sensitivity behaviors. By changing the silicon wafer plane, SAW propagation direction and longitudinal/lateral strain ratio, the reverse strain effect can be engineered. Hence, the sensitivity of the pressure sensor may be increased, without sacrificing its high pressure sensing range for harsh environment applications.

Chapter 4 Decoupled Viscosity and Density MEMS Sensor

Viscosity η and density ρ are two important physical parameters of a liquid, which are widely utilized for liquid identification. By determining these two parameters, components and corresponding concentrations of a liquid can be estimated as well. Viscosity and density sensors therefore attract many researchers' interests and have been developing since 1980s. Benefiting from advantages of high sensitivity, small size, real-time readout capability, robustness and low cost, acoustic wave sensor has been widely adopted for liquid viscosity and density sensing [118-126]. Various applications are successfully realized using viscosity and density sensors.

Nomura *et al*. reported a liquid flow sensing system in 2000, where the resonance frequency change to viscosity and density is used as a liquid sensor time response [127]. As is shown in Figure 4.1, the transient responses show a unique shape and the difference of transient responses depends on the type of dissolving molecules and concentration of aqueous solutions. Discrimination of liquids and estimation of their concentrations by determining viscosity and density are proven to be feasible.

In 2004 a smart tongue device based on the viscosity and density detection was proposed by Cole *et al.* for measurement of beverage properties [118]. With a very small amount of liquid, this smart tongue can clearly discriminate between the different samples (*e.g.* water, milk and orange juice). Further tests on commercial milk samples with different fat contents (whole milk with 4% fat, semi-skimmed with

2% fat, and skimmed milk with no fat) show the linear discrimination of skimmed-level. Even the freshness of whole milk samples can be determined using such smart tongue device, and five distinct clusters are shown in Figure 4. 2 (e).

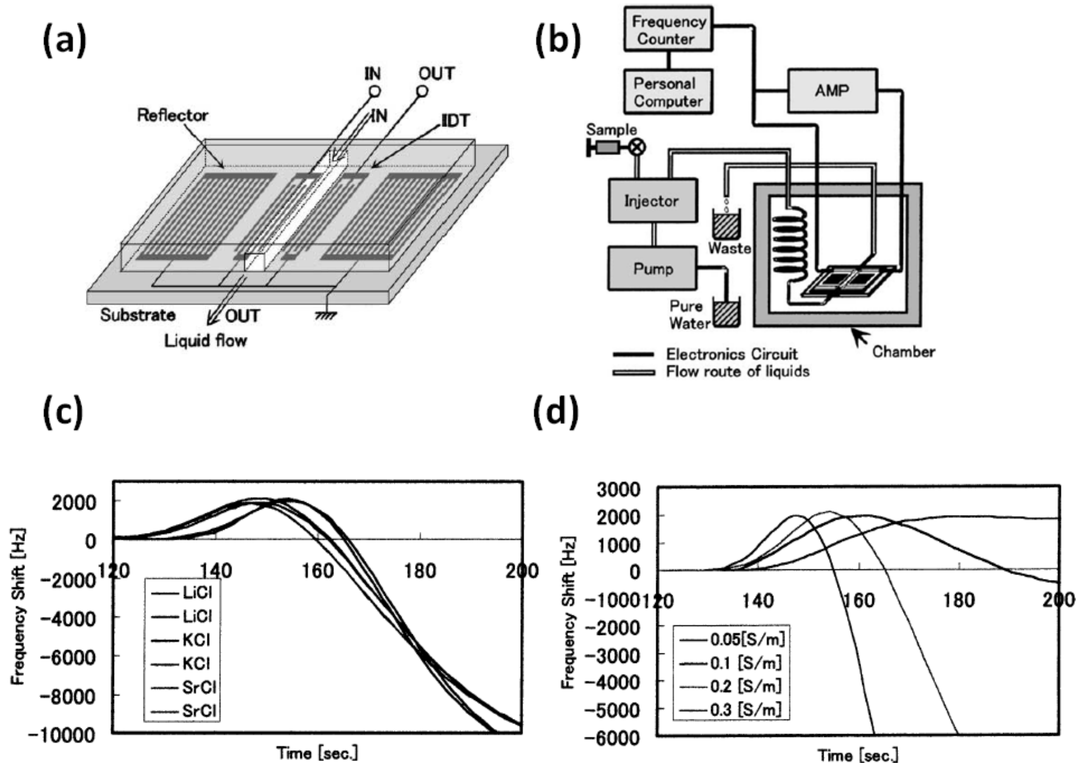

Figure 4.1 Liquid flow sensing system [127]: (a) geometry of viscosity & density sensor with liquid flow channel; (b) block diagram of the flowing system for the sensor measurements in liquid phase; (c) transient frequency responses of the sensor to various aqueous solutions (with constant concentration) and; (d) transient frequency responses of the sensor as a function of concentration for KCl aqueous solutions.

In 2012, Vivancos *et al.* developed an analytical system for determining surfactants and detergents in water [128]. Such system correctly classified three detergents without selective chemical or biology coating, while the detection limit was found to be as small as ca. 10 ppm, shown in Figure 4.3. Equipped with this

system, a household washing machine can automatically choose appropriate number of rinsing cycles, according to the concentration of residual detergents. With less detergent, less water and less energy consumption, the new generation washing machines will become smarter and greener.

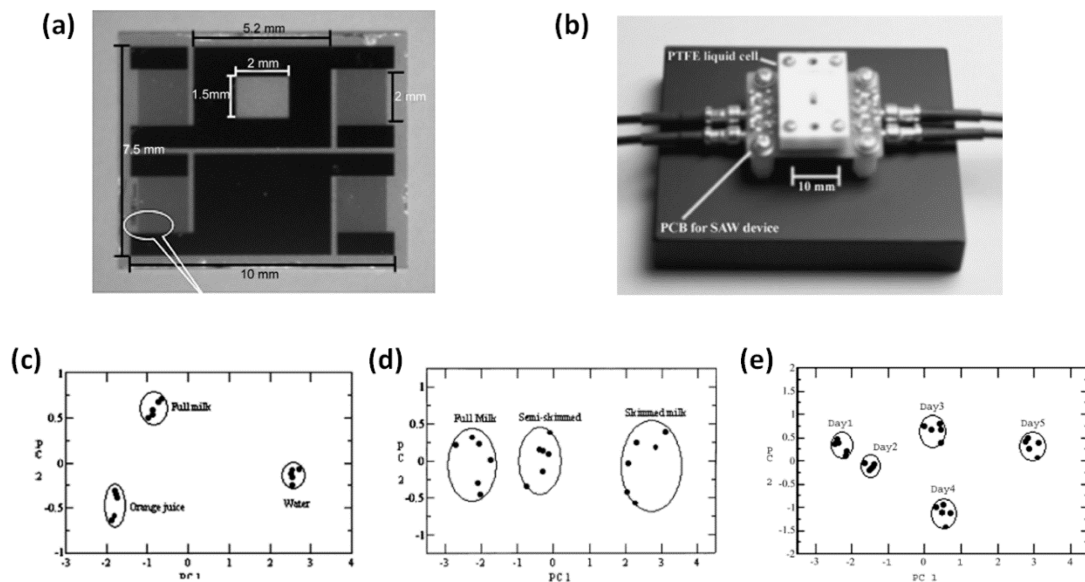

Figure 4.2 Viscosity and density detection based smart tongue device [118]: (a) photograph of fabricated device; (b) Photograph of the assembled device with the liquid reservoir used for experimental setup; (c) testing of different liquids showing excellent discrimination; (d) testing of milk samples with different skimmed-level and; (e) Testing of milk samples showing the effect of aging.

Nowadays, the biomedical applications based on viscosity and density sensor appear to be emerging. Xu *et al.* presented a viscosity sensor, monitoring *in-vitro* blood coagulation process in real time [129]. This sensor provides the coagulation time and the start/end of the fibrin generation, and accesses the clot strength, using the viscosity change of the blood sample (Figure 4.4). Monitoring the coagulation of whole blood is of great value for both the medical diagnosis of hemostasis disorders and clinical treatment / surgical procedure for cardiovascular diseases.

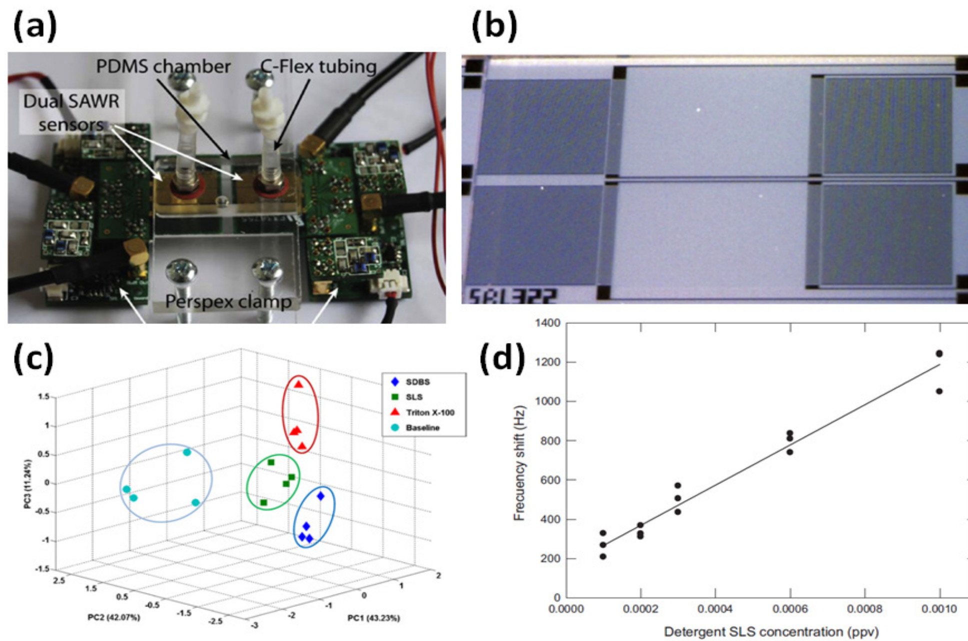

Figure 4.3 Analytical system for residual liquid detergent detection [128]: (a) photograph of the assembled system; (b) OM of fabricated sensor; (c) principal components analysis of different detergents and; (d) frequency response vs. different concentrations of detergent solutions.

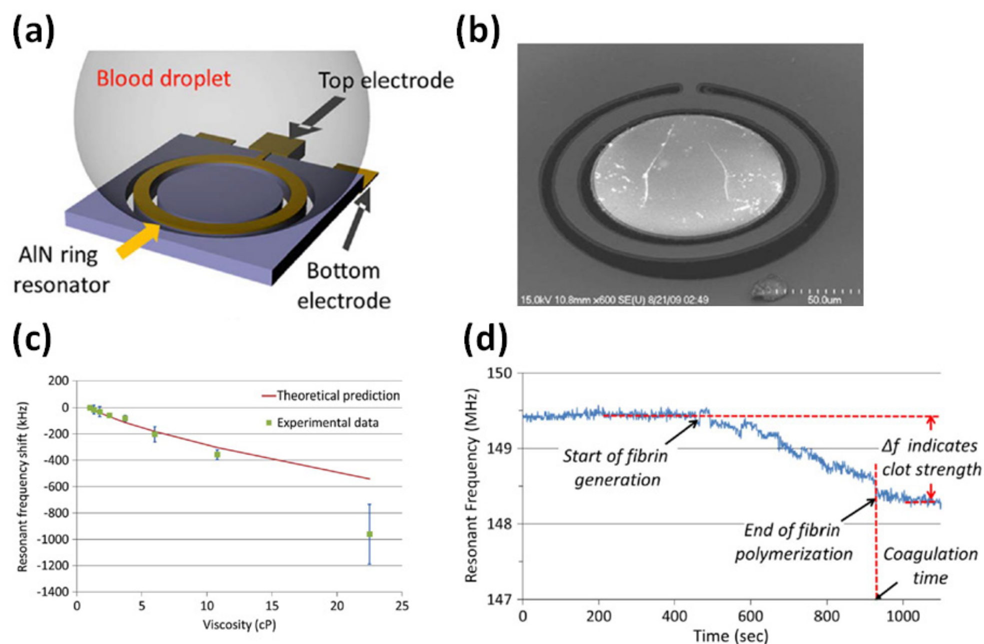

Figure 4.4 Real-Time monitoring of whole blood coagulation [129]: (a) Schematic illustration; (b) an SEM image of the fabricated device; (c) Viscosity characterization and; (d) Real-time monitoring the coagulation process of a citrated blood.

4.1 Motivation

Many successful applications using viscosity and density sensors have been achieved; however, the sensors themselves have limitations. The major limitation of conventional sensors is that they are not able to separately measure liquid's viscosity and density [130, 131]. The frequency response of such sensors is proportional to the square root of viscosity density product [127, 132, 133]. Although many devices are claimed as viscosity sensors, they actually assume that density is a constant and overlook its influence. This assumption may not always be true for real cases [134, 135]. To address such issue, Herrmann *et al.* proposes an approach using dual SAW sensors to decouple these two parameters η and ρ [136]. As shown in Figure 4.5 (a), one reference device with smooth surface is used to sense $(\eta{\cdot}\rho)^{1/2}$. The other device is corrugated by microfabricated sagittal trenches. Frequency response of the corrugated sensor is proportional to ρ and nearly non-sensitive to η. η then can be calculated from known $(\eta{\cdot}\rho)^{1/2}$ and ρ. The main drawback of this approach is the employment of dual-device, which significantly increases the cost and complexity. Challenges also come from the indirect differentiation method, making the signal processing difficult. Another trial to decouple the two parameters is proposed by Martin *et al.* using a Lamb wave sensor [137]. Because frequency related phase velocity of Lamb wave is mainly influenced by liquid density, frequency response of this sensor is found to be proportional to ρ in a relatively wide range of viscosity. On the other hand, attenuation response of this sensor still depends on $(\eta{\cdot}\rho)^{1/2}$. With measured ρ and $(\eta{\cdot}\rho)^{1/2}$, η hence can be derived. Although this approach realizes the separation of η and ρ with a single device, it is still an indirect method and the accuracy of attenuation measurement has no guarantee. In addition, phase velocity of Lamb wave is not solely determined by

liquid density. This device can only function when liquid viscosity is small and influence of liquid sound velocity is neglected. When the viscosity is large, measured data cannot be trusted, illustrated in Figure 4.5 (b). Zhou *et al.* makes an improvement on Lamb wave sensor, which successfully decouples the liquid sound velocity using multi-mode Lamb waves. Other problems of Lamb wave sensor are not addressed [138].

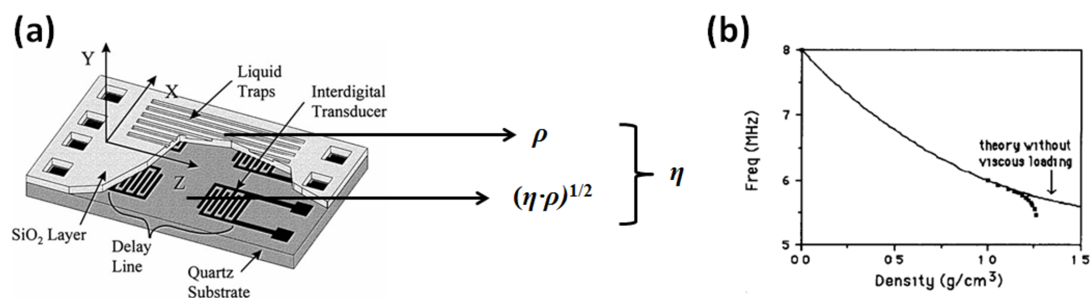

Figure 4.5 (a) Dual SAW sensors from [136]. $(\eta\cdot\rho)^{1/2}$ is measured using sensor with smooth surface while ρ is obtained by sensor with corrugated surface. η can be derived from the two values and; (b) frequency response of the Lamb wave sensor from [137]. Frequency response is assumed to be independent with liquid viscosity, but this is only valid when viscosity is small enough.

Another limitation is from the widely adopted delay line configuration [138-140]. Although Lamb wave sensor is a powerful device for liquid sensing [42-46], the delay line configuration has the issues of low quality factor, low stability and low reproducibility. Resonator configuration, on the contrary, provides a compact and rugged solution with high quality factor, which significantly reduces the complexity of signals readout [127]. Unfortunately, studies on Lamb wave resonator for liquid sensing are quite limited [141, 142]. Meanwhile, most of researchers mainly focus on the lowest mode of Lamb wave and pay no attentions to higher-order modes effects on liquids properties sensing by far.

In this chapter, a novel AlN based MEMS Lamb wave sensor is proposed, which

is able to directly measure liquid's η and ρ by using higher-order modes of Lamb wave. This unique feature realizes the easy separation of η and ρ by a single device at the first time. Resonator configuration is utilized to guarantee stable and easy-readout signals. Experimental results prove the sensor's capability of differentiating liquids such as DI water and ethanol, which are likely to be mixed up by conventional sensors.

4.2 Working Principles and Sensor Design

When a Lamb wave sensor is loaded with liquid, the phase velocity of its lowest asymmetric mode A_0, which is commonly employed for liquid sensing by conventional sensors, is given by [140]:

$$V_{ph} = \frac{2\pi}{\lambda}\sqrt{\frac{B}{M_{eff}}} \tag{4.1}$$

where λ is the wavelength of the acoustic wave, B the bending stiffness of the plate: $B=d^3E/[12(1-\upsilon^2)]$, d is the plate thickness, E is the Young's modulus, υ is the Poisson ratio. M_{eff} is the effective mass:

$$M_{eff} = M_{plate} + M_{den} + M_{vis} \tag{4.2}$$

M_{plate} is the unit plate mass, M_{den} is the mass loading due to liquid density, and M_{vis} is the viscous loading of the liquid. The corresponding frequency is expressed as:

$$f = \frac{v_{ph}}{\lambda} \tag{4.3}$$

The A_0 wave is a combination of longitudinal and transverse waves, where the motions of particles on the plate are in elliptical paths, having the components both perpendicular and parallel to the plate plane. The normal component along y-direction generates an evanescent pressure wave which displaces the liquid in the skin depth, and the liquid mass loading M_{den} lowers the phase velocity. Meanwhile the in-plane component along x-direction generates shear waves in liquid. The viscous loading contributes to the M_{vis} and lowers the phase velocity as well [137].

According to [40], the relative magnitude of the two components is a function of frequency-thickness product. At certain product value, one of the components becomes zero and the motion of particles is either entirely perpendicular or parallel to the plate plane. Especially for the higher-order modes of Lamb wave, at nascent frequencies of some particular modes, the motion of particles at the backside surface is either entirely perpendicular or parallel to the plate plane. The mode with perpendicular motion thus should be only sensitive to ρ, while the mode with parallel motion should respond to η. η and ρ therefore can be separately determined by using the two unique modes.

However, frequency of higher-order modes may be extremely high. In [143] authors reported first four modes with frequencies up to 4 GHz. Such high frequency will bring extra issues on signals readout and processing. In addition, high frequency is not preferred for viscosity sensing, as liquid are more likely to become viscoelastic in high frequency range. The viscoelastic effect will be discussed later. According to velocity dispersion curves, phase velocity of Lamb wave decreases with increasing plate thickness, which leads to a lower frequency. Therefore, a relatively thick plate is usually adopted to decrease the frequency of higher-order modes.

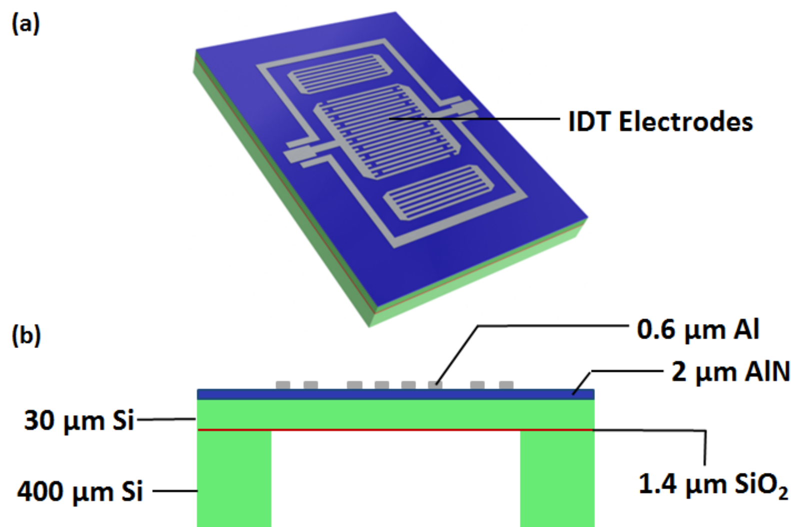

Figure 4.6 Schematic drawing of the directly decoupled viscosity and density sensor: (a) bird's view and; (b) cross-sectional view. The IDT electrodes induce the Lamb wave within the plate. Relatively thick device silicon (30µm) is employed for the plate to lower the frequency of higher-order modes.

Schematic drawing of the decoupled viscosity and density sensor is shown in Figure 4.6. A 2µm AlN layer is deposited as the piezoelectric material. This material has been well studied and widely utilized in acoustic wave resonator implementations, because of its efficient electromechanical transaction [144]. A set of IDT electrodes made of 0.6µm Al with 20µm periodicity ($= \lambda$) is used for Lamb waves' generation. Since the plate is not infinite, propagating Lamb waves will be reflected back at the lateral extremities, giving rise to resonant modes [145]. It is significant that a 30µm Si layer and a 1.4µm SiO_2 layer are attached below AlN layer. This AlN/Si/SiO_2 composite plate has a thickness of 33.4µm in total, which is about 1.5 times the Lamb wavelength 20µm. Eq. (4.1) is no longer valid for such situation because it is only valid when the plate thickness $d << \lambda$ [140]. A 2-D finite element model therefore is employed for analysis in this research.

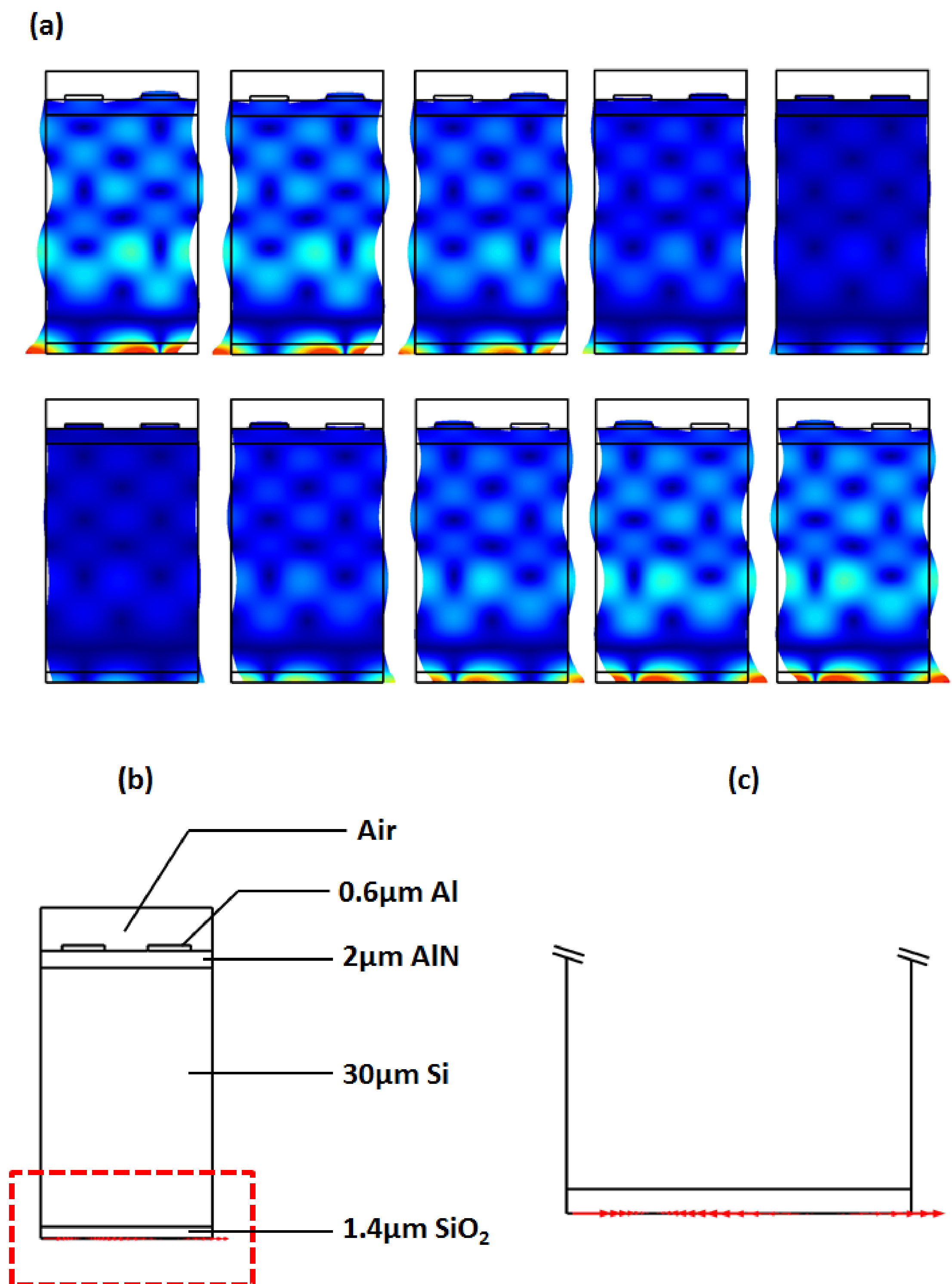

Figure 4.7 Simulation results of Mode 1: (a) mode shape; (b) velocity vectors on backside surface and; (c) zoom-in view of velocity vectors. Motion of particles on backside surface is entirely in-plane, generating shear waves in liquid.

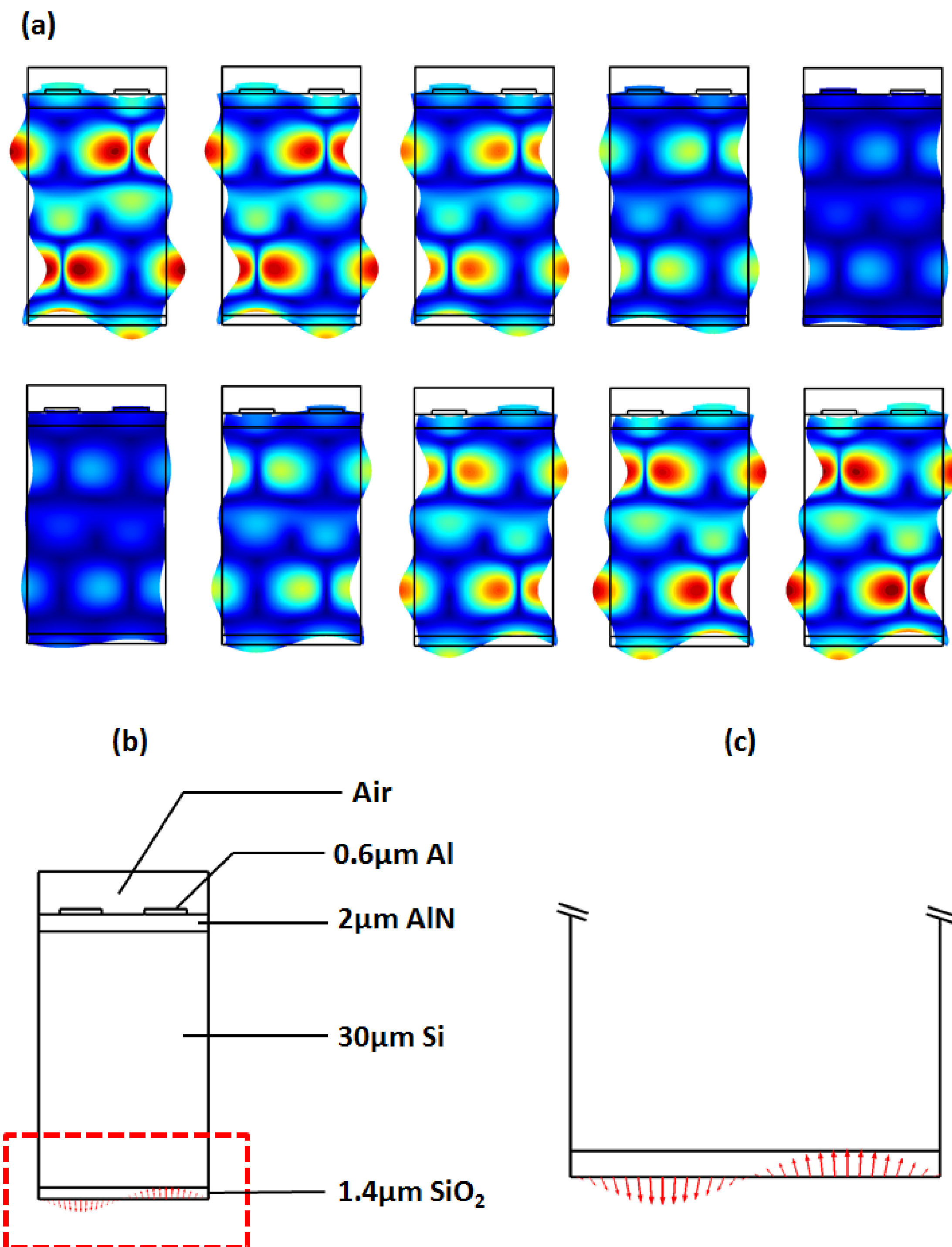

Figure 4.8 Simulation results of Mode 2: (a) mode shape; (b) velocity vectors on backside surface and; (c) zoom-in view of velocity vectors. Motion of particles on backside surface is out-of-plane, generating longitudinal waves in liquid.

Admittance and resonance mode shapes of higher-order modes are simulated using COMSOL multi-physics software. Only those modes which can be electrically excited are considered. Two noteworthy modes are found in the simulation, denoted as Mode 1 and Mode 2. Shape of Mode 1 is shown in Figure 4.7 (a) and the velocity vectors of backside surface are shown in Figure 4.7 (b) and (c). The motion of the backside surface is in-plane and velocity vectors are entirely parallel to the plate plane without any normal components. For Mode 2, the motion of the backside surface is out-of-plane, shown in Figure 4.8 (a). As can be seen from Figure 4.8 (b) and (c), most of velocity vectors are perpendicular to the plate plane. Non-perpendicular vectors are rare and weak, of which the influences are quite limited. As aforementioned, Mode 1 with parallel motion can be used to sense viscosity, while Mode 2 with perpendicular motion can be used to sense density of a liquid.

To further study the two modes, a layer of fluid is defined at the bottom of the device. The interface “Acoustic-Piezoelectric Interaction” with frequency domain study is employed to simulate the interaction between the device and fluid. It is worth noting that the fluid is modeled as “Viscous”, which takes fluid’s both density and viscosity into consideration. However, due to the software limitation, viscosity lowers the peak amplitude but does not influence the frequency at all. Only the density contributes to the frequency shift of the device. Simulated frequency responses to density change of Mode 1 and 2 are shown in Figure 4.9. Behaviors of these two modes are much different. Frequency of Mode 1 does not shift at all, while frequency of Mode 2 decreases with a sensitivity of -2478 ppm / g/cm^3. Such simulation results prove that liquid density has no influence on frequency shift of Mode 1, thus any frequency shift of Mode 1 should be contributed by viscosity.

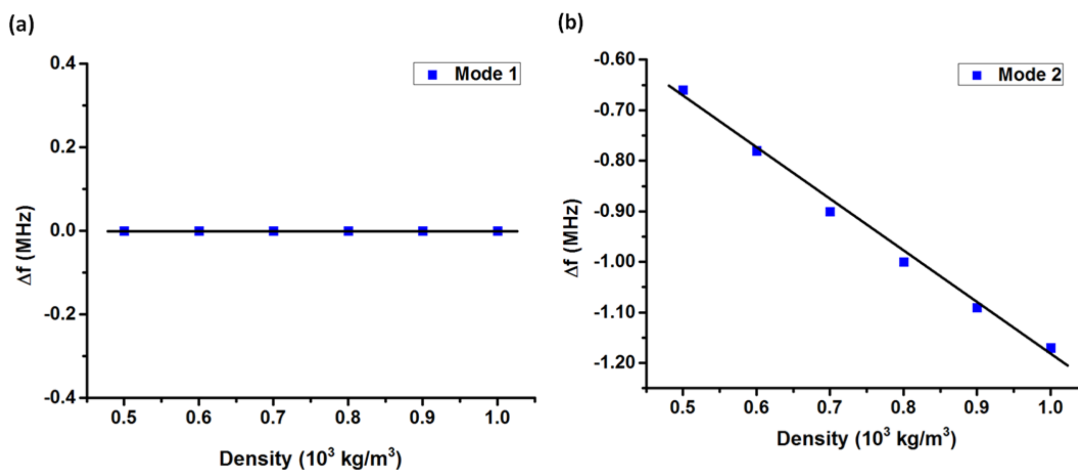

Figure 4.9 Simulated relative frequency shifts to the density of (a) Mode 1 and (b) Mode 2. Frequency of Mode 1 does not shift to density at all, which can be used for viscosity sensing.

4.3 Experimental Results and Discussions

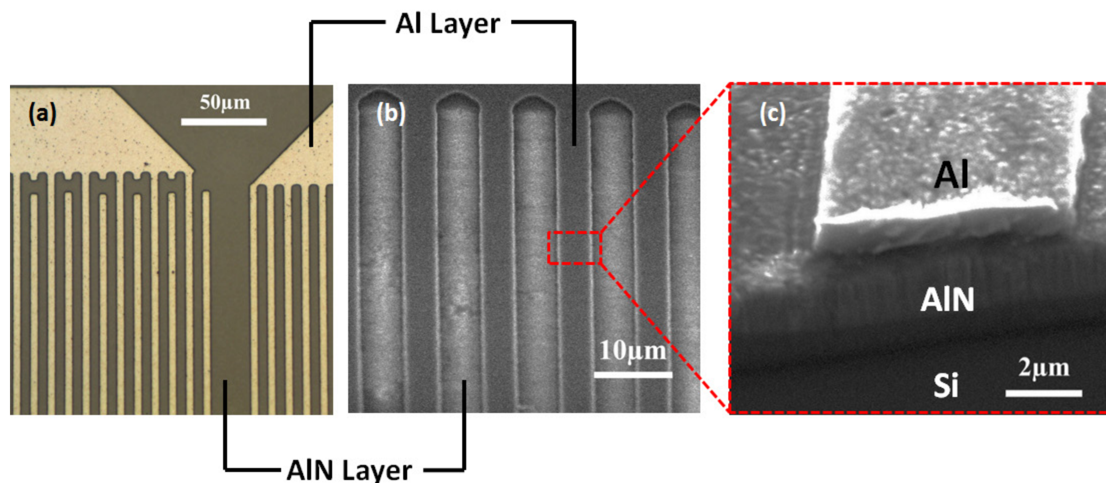

Figure 4.10 The fabricated decoupled viscosity and density sensor: (a) optical microscope photograph; (b) scanning electron microscope (SEM) photograph; and (c) cross-sectional SEM photograph.

The fabricated device is shown in Figure 4.10. Both optical microscope and SEM images indicate the well patterned electrodes. The bright regions between electrodes

in Figure 4.10 (b) are probably due to electrons charging on AlN dielectric layer. Cross-sectional SEM image of the device is given in Figure 4.10 (c).

4.3.1 Testing setup

The fabricated device is mounted on a PCB with a through hole (3 mm in diameter) in the center as shown in Figure 4.11 (a, c). This hole enables backside surface of the released membrane expose to the environment. Liquid under test is injected through the hole and contacts with the bottom surface. All the bonding wires are sealed and protected by silicone, illustrated in Figure 4.11 (b). Silicone sealing prevents bonding wires from the possible influences of splashed liquid or external stuffs. Even a small amount of liquid on bonding wires can result in significant signal fluctuation due to the perturbation on parasitic parameters such as capacitance. Hence silicone sealing is a key step to ensure the stable signals. Furthermore, to eliminate the parasitic effects brought by PCB package and cables, a PCB calibration kit with open, short, through and load (50 Ω) configurations is fabricated as well, shown in Figure 4.11 (d). These configurations are of exactly the same layout with the testing PCB package.

The testing is conducted by measuring the S11 parameter in the range of 400 MHz to 550 MHz using an Agilent E5071B network analyzer under a fixed room temperature of 24°C. The maximum sweeping points of this instrument is 16001, which implies the frequency resolution is limited to about 10 kHz. Calibration is first performed with the kit mentioned above. The open circuits S11 after calibration is greater than -5 dB. This indicates that most of signals are reflected back and interferences from PCB and cables are minimized.

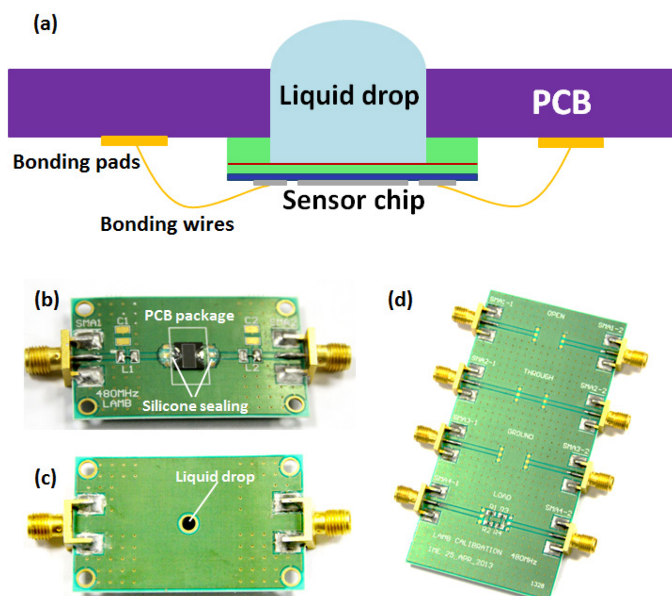

Figure 4.11 (a) Schematic drawing of packaged sensor with loaded liquid under test; sensor mounted on the holed PCB with sealed bonding wires by silicone (b) front side and (c) backside; (d) PCB calibration kit for eliminating the interferences from cables and PCB package.

4.3.2 Device testing in air

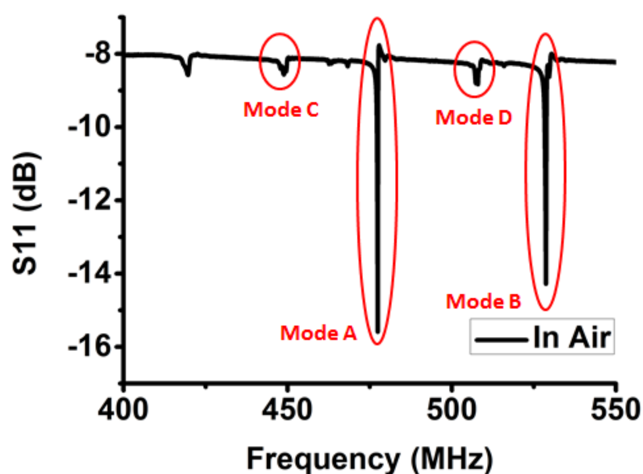

Figure 4.12 S11 parameter in the range of 400 MHz to 600 MHz, measured in air using Agilent E5071B network analyzer. The signal is quite stable while high Q-factor makes easy and accurate frequency determination possible

S11 parameter in air is firstly recorded as in Figure 4.12 for the reference, and all shifted frequencies will be compared with this. Benefited from the thick stack plate, five higher-order Lamb wave modes are generated within the 150 MHz bandwidth. In addition, high quality factors improve the accuracy of the frequency shift measurement and make an easy-readout possible.

4.3.3 Liquids testing

4.3.3.1 Liquids testing using DI water, acetone ethanol and IPA

Four liquid samples are firstly adopted for the testing: deionized water (DI water), acetone, ethanol and isopropyl alcohol (IPA). Mechanical properties viscosity η, density ρ and square root viscosity-density product $(\eta\cdot\rho)^{1/2}$ of the four liquids are summarized in Table 4.1. Each liquid is dripped into the PCB hole (shown in Figure 4.10 (c)) and directly contacts with backside surface of the sensor. When the signal is stable with no fluctuation, S11 parameter is recorded thereafter. Frequency responses of all five modes are studied, and four out of them are noteworthy, denoted as Mode A to D.

Table 4.1 Summary of mechanical properties of air and chemicals

Samples	η (mPa·s)	ρ ($\times 10^3$ kg/m^3)	$(\eta\cdot\rho)^{1/2}$ (kg·m^{-2}·s$^{-1/2}$)
Air	0.019	0.001	0.005
DI Water	0.894	1.000	0.946
Acetone	0.306	0.791	0.492
Ethanol	1.070	0.789	0.921
IPA	1.960	0.786	1.241

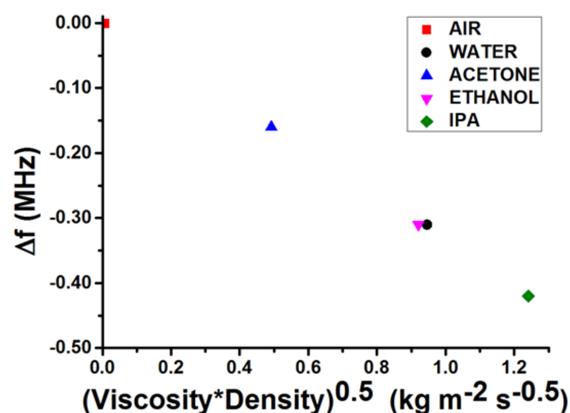

Figure 4.13 Relative frequency shifts to the square root of viscosity-density product of Mode A in DI water, acetone, ethanol and IPA. DI water and ethanol share the same frequency response.

Frequency response of Mode A and Mode B behaves similarly, and linear correlation between frequency and $(\eta \cdot \rho)^{1/2}$ is revealed. Such behavior is similar to conventional sensors. The frequency response of Mode A is plotted in Figure 4.13 as an example. These two modes are not able to differentiate the coupled influence of viscosity and density. Although DI water and ethanol have different viscosities and densities, their products are very close to each other (as shown in Figure 4.13). The two liquids therefore can hardly be differentiated using these conventional modes.

Figure 4.14 shows the frequency response of Mode C, which behaves like the Mode 1 in simulation (see Figure 4.7). This mode reveals almost linear frequency shift relationship with η of liquids, without influence of density change. Thus DI water and ethanol are clearly distinguished due to the viscosity difference. On the contrary, frequency response of Mode D seems sensitive to ρ only, corresponding to Mode 2 in simulation (see Figure 4.8). Acetone, ethanol and IPA are three liquids which have almost the same ρ but largely different η. As is demonstrated in Figure

4.15, frequency responses of such three liquids are overlapped together and this indicates that Mode D is non-sensitive to η. As a result, viscosity and density of a liquid are separately detected by using Mode C and Mode D, while the corresponding viscosity and density sensitivity are calculated as -569 ppm / mPa·s and -748 ppm / g/cm^3, respectively. The sensitivity is derived as the frequency shift divided by the frequency for the particular mode.

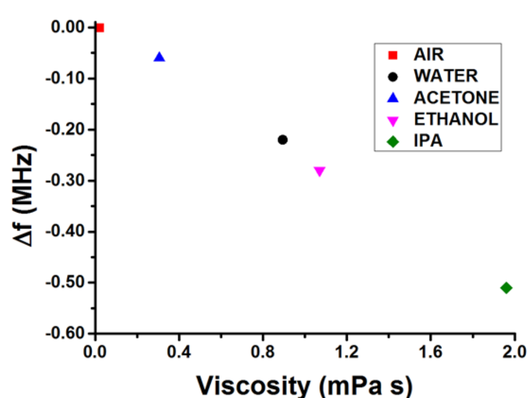

Figure 4.14 Relative frequency shifts to the viscosity of Mode C in DI water, acetone, ethanol and IPA. DI water and ethanol are discriminated due to their different viscosities.

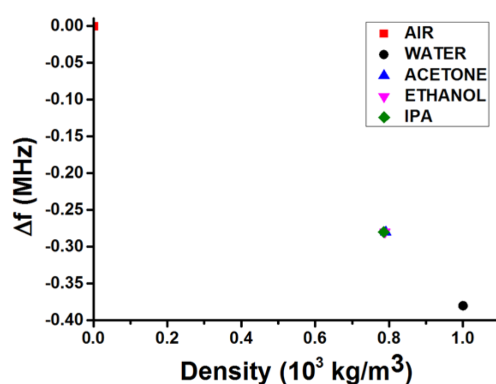

Figure 4.15 Relative frequency shifts to the density of Mode D in DI water, acetone, ethanol and IPA. Acetone, ethanol and IPA cannot be differentiated because of the almost same density, indicating frequency response of Mode D is not influenced by viscosity.

4.3.3.2 Liquids testing using glycerol-water mixtures

Table 4.2 Summary of mechanical properties of glycerol-water mixtures

Glycerol Volume Concentration (%)	η (mPa·s)	ρ ($\times 10^3$ kg/m^3)	$(\eta \cdot \rho)^{1/2}$ (kg·m^{-2}·s$^{-1/2}$)
0	0.894	1.000	0.946
10	1.221	1.029	1.121
20	1.732	1.060	1.354
30	2.575	1.089	1.673
40	4.058	1.118	2.130
50	6.879	1.144	2.806

To further characterize the sensor performance in high-viscosity range, glycerol-water mixtures are utilized. Glycerol-water solutions as standard Newtonian liquids are widely used for viscosity sensor testing. By changing the glycerol/water ratio, viscosity of these solutions ranges from 1 to 1500 mPa·s at room temperature, while the density only changes from 1 to 1.29 g·cm^{-1} [146]. Mixtures with glycerol volume concentration from 0 to 50% are made for testing, using G5516 glycerol (≥99%) from Sigma-Aldrich®. Viscosity η, density ρ and square root viscosity-density product $(\eta \cdot \rho)^{1/2}$ of the glycerol-water mixtures are calculated and summarized in Table 4.2.

Highly viscous liquids like glycerol-water mixtures tend to deviate from Newtonian behaviors, becoming viscoelastic. Response of most viscosity sensors leaves the linear dependence, when liquid viscosity goes beyond a certain value due to viscoelastic effect [147]. For example, the response of the device reported in [148]

starts becoming nonlinear from about 3.6 mPa·s. This turning point is related to the device operating frequency, which becomes higher for lower frequency. In terms of current work, fully linear correlation of Mode C is observed in Figure 4.16 (b), with liquid viscosity up to 7 mPa·s. Such linear behavior may be partially due to the moderate operating frequency. It is also worth noting that although the liquid viscosity changes largely, frequency shift of Mode D is very small and proportional to the slightly changed density, shown in Figure 4.16 (c). There is no deviation from the linear dependence is observed and this implies that Modes D is highly independent of liquid viscosity.

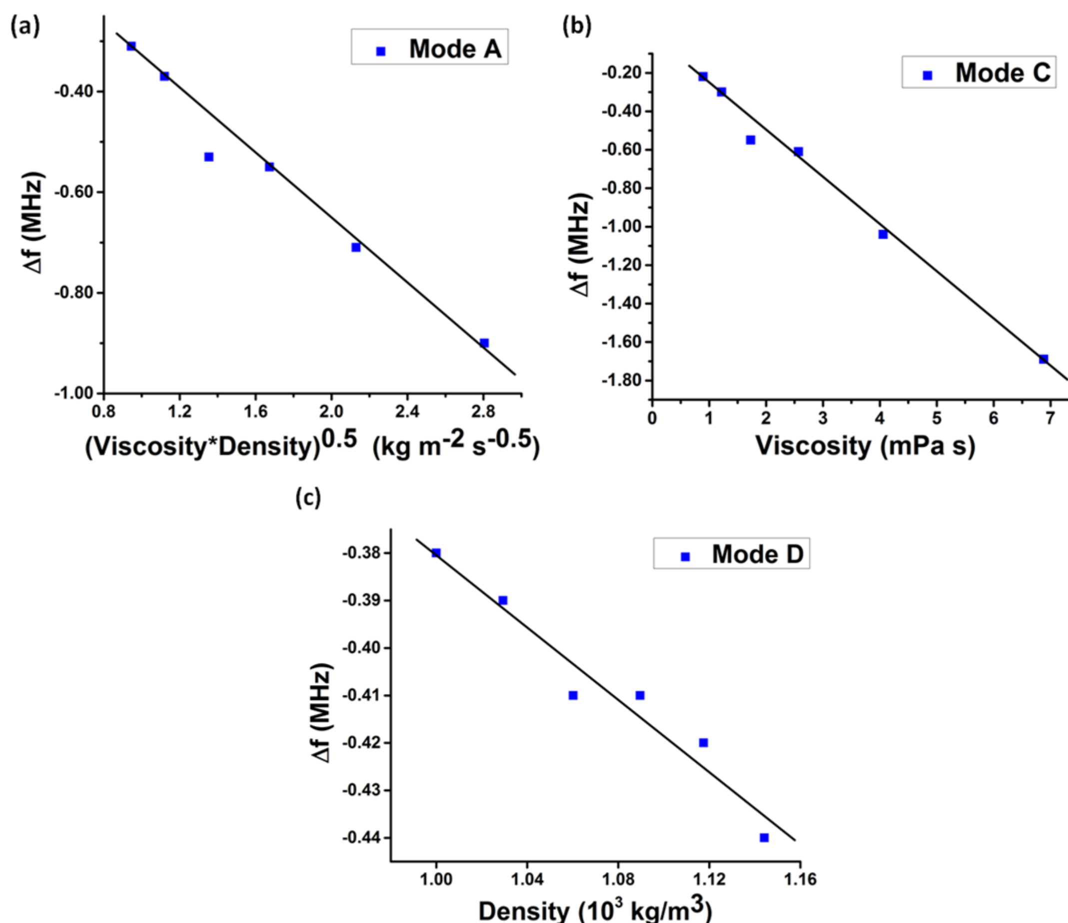

Figure 4.16 Relative frequency shifts in glycerol-water solutions with volumic concentration from 0% to 50%: (a) Mode A to the square root of viscosity-density product; (b) Mode C to the viscosity and; (c) Mode D to the density.

4.3.3.3 Liquids testing using NaCl solutions

Table 4.3 Summary of mechanical properties of NaCl solutions

NaCl Mass Concentration (%)	η (mPa·s)	ρ ($\times 10^3$ kg/m^3)	$(\eta \cdot \rho)^{1/2}$ (kg·m^{-2}·s$^{-1/2}$)
0	0.894	1.000	0.946
4.76	0.959	1.040	0.998
9.09	1.042	1.068	1.055
13.04	1.142	1.095	1.119
16.67	1.260	1.132	1.195
20.00	1.396	1.157	1.271

NaCl solutions with different concentrations are also made for testing, by dissolving 0.5 – 2.5 g NaCl into 10ml DI water. Volume changes due to dissolved NaCl are considered for calculation as well. Both viscosity and density of NaCl solution slightly increase with NaCl concentration, summarized in Table 4.3 [149]. NaCl solutions are mainly used to study the minimum detection limit of this decoupled viscosity and density sensor. The frequency shifts due to NaCl solutions are extremely small. Such small shifted frequency already approaches to the frequency resolution of network analyzer, illustrated in Figure 4.17. Minimum detectable viscosity and density changes of this sensor are 0.065 mPa·s and 0.025 g/cm^3, respectively.

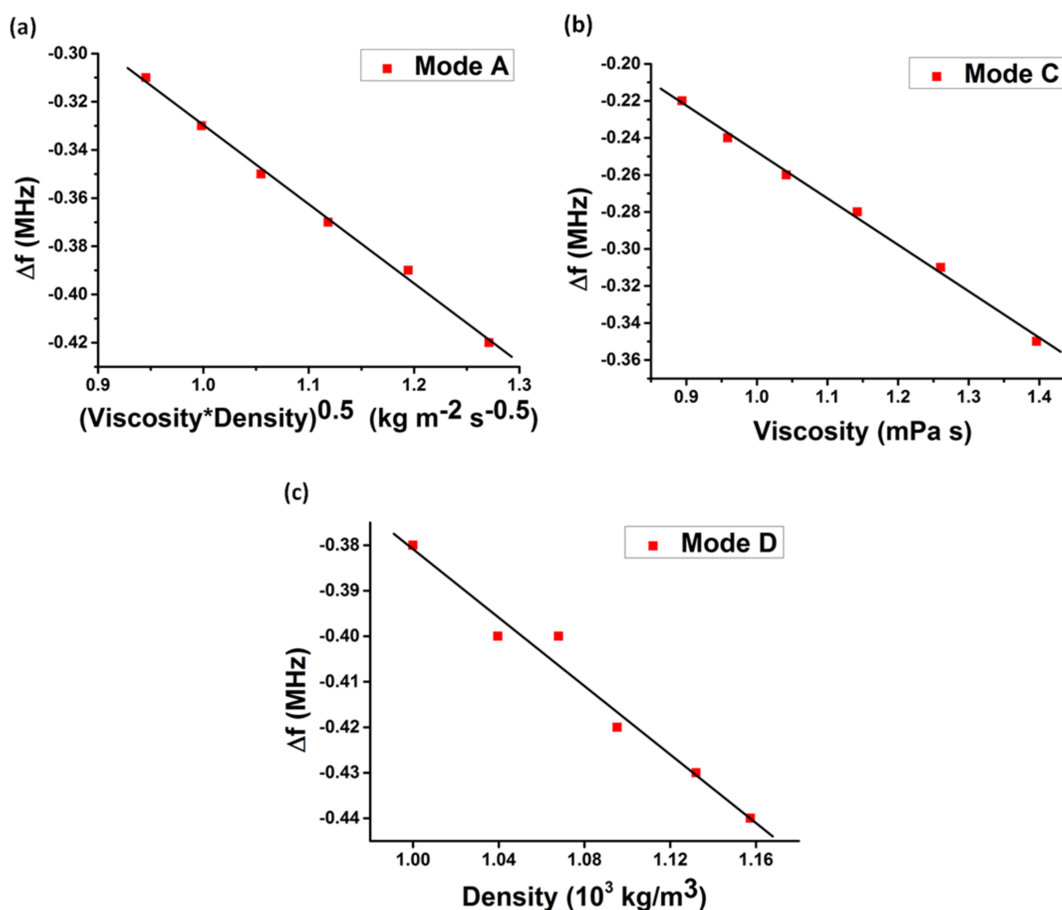

Figure 4.17 Relative frequency shifts in NaCl-water solutions with mass concentration from 0% to 20%: (a) Mode A to the square root of viscosity-density product; (b) Mode C to the viscosity and; (c) Mode D to the density.

4.3.3.4 Potential applications as a label-free liquid sensor

As mentioned above, conventional acoustic wave sensors have many limitations when used as label-free liquid sensors. Frequency responses to liquids like DI water and ethanol are probably overlapped as shown in Figure 4.13. Such liquids may be determined as the same one by conventional sensors. Whereas, with the decoupled viscosity and density sensor, a novel 2-D method for label-free liquid detection is available by plotting frequency response of Mode C vs. that of Mode D, demonstrated in Figure 4.18. In this plot, DI water and ethanol can be easily differentiated because

of different viscosities and densities. Acetone, ethanol and IPA share almost the same density and form a horizontal line in the plot. This 2-D method may have wide applications in oil industry. Diesel fuels with different Cetane numbers have relatively constant density but varying viscosity [136]. The Cetane number can be determined by measuring the viscosity. Meanwhile, if the diesel fuel is unexpectedly mixed into water, it should be detected due to the density difference. By using this 2-D method, Cetane number and water percentage may be simultaneously obtained.

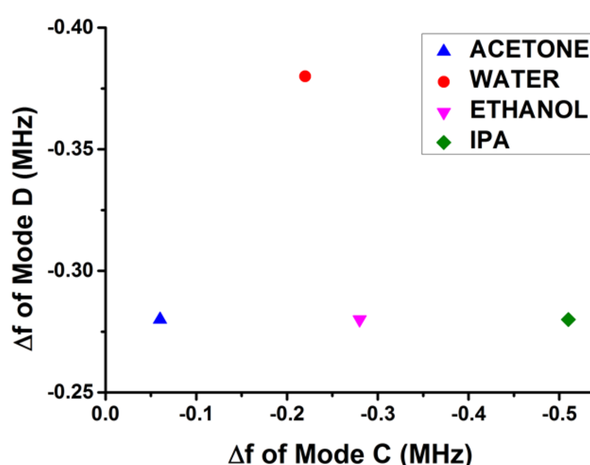

Figure 4.18 A novel 2-D method for label-free liquid detection. Frequency responses of Mode C and Mode D are plotted in X-axis and Y-axis, respectively. Liquids with same viscosity-density product or same density can be easily discriminated by this method.

4.4 Summary

In this chapter, a directly decoupled viscosity and density sensor using Lamb wave resonator is proposed. AlN MEMS resonator based sensor is capable of generating stable signals with high quality factor. Higher-order modes of Lamb wave are utilized for viscosity and density detection. Two unique modes (Mode C and Mode D) are found with backside surface particle motions either parallel (Mode C) or

perpendicular (Mode D) to the plate plane. Frequency response of Mode C is dominated by viscosity with a sensitivity of -569 ppm / mPa·s, while that of Mode D is solely determined by density with a sensitivity of -748 ppm / g/cm^3. Decoupled viscosity and density sensing is achieved by a single device. Without suffering from viscoelastic effects, viscosity dependence of this sensor remains linear with liquid viscosity up to 7 mPa·s. The minimum detectable change for viscosity (0.065 mPa·s) and density (0.025 g/cm^3) are quite small. A novel 2-D liquid detecting method based on the sensor is proposed. DI water and ethanol are clearly differentiated by this method. Potential applications of such 2-D method in the oil industry are shown as well.

.

Chapter 5 Highly Efficient pMUT with Enhanced Performance

As is discussed in Section 1.3.2, pMUT overcomes all the inherent drawbacks of cMUT, and particularly it operates at a much lower voltage [65]. The pMUT seems to be a promising solution for future ultrasonic applications. Unfortunately, performances of previously reported pMUTs are much poorer than the expectation. Their coupling efficiency between electrical and mechanical domain is significantly lower than the prediction from Finite Element Model (FEM) [50, 65, 150-152]. This problem is mainly attributed to the residual stress of the fabricated devices, because any residual stress may hamper the membrane vibration. Since fabrication of pMUT usually contains several high temperature processes, the residual stress in pMUT membrane can hardly be reduced. As a consequence, the performance of the pMUT, in particular the transmitting sensitivity, is far from satisfactory [50, 153]. A few attemps are made to address this stress issue. Mo *et al*. try to reduce the membrane buckling by removing the buried oxide layer. However, the improvement of device performance is quite limited [154]. Muralt *et al.* try to optimize the fabrication process and use compressively stressed oxide layer to balance the PZT layer with tensile stress [65]. Although a relatively flat membrane is achieved through the stress compensation, the transmitting sensitivity is still unsatisfactory. Because the membrane vibration is very sensitive to the residual stress, even a non-obvious membrane deflection may drastically lower the transmitting sensitivity. A large DC

bias is also introduced to balance the undesirable residual stress. Although the sensitivity is improved, this requires pMUT to be operated at high voltage similar to the cMUT [155, 156]. Therefore, researchers have to employ another bulk ceramic based ultrasonic transducer for ultrasound transmission, or even suggest the pMUT may only be used for ultrasound receiving for practical application [153]. Therefore, enhancement of pMUT transmitting sensitivity, *i.e.* increasing the transmitted acoustic pressure, is always desirable.

In this chapter, we design, fabricate and characterize two AlN based novel pMUTs, aiming to achieve higher performance. The first pMUT realizes a zero-bending membrane, and its transmitting sensitivity is 450% higher than the reference pMUT. The second pMUT employs etching holes to realize a piston-like membrane motion during vibration, which helps to generate higher ultrasound pressure.

5.1 Zero-Bending Membrane pMUT

5.1.1 Design consideration

5.1.1.1 Stress influence on transmitting sensitivity

To predict the performance of pMUT, several analytical models are proposed [157-159]. The pMUT is modeled as a uniform circular thin plate with clamped boundary conditions. If the pMUT works at transmitting mode (*i.e.* the effects from external acoustic pressure can be neglected), the plate deflection $w(r)$ at a radial position r can be described in the general form as:

$$D\nabla^2\nabla^2 w(r) + \rho_s \frac{\partial^2 w(r)}{\partial t^2} = \nabla^2 M^p \tag{5.1}$$

$$D = \int \frac{E(z)z^2}{1-\upsilon(z)^2} dz \tag{5.2}$$

$$\rho_s = \int \rho(z)dz \tag{5.3}$$

where D is the modulus of flexural rigidity, ρ_s is the area plate density, E is the Young's modulus, υ is the poison's ratio, and M^p is the piezoelectric moment induced by input voltage [158]. E and υ vary with z-direction because of the different materials at each layer. However, this model does not take residual stress into consideration. Influence of residual stress on pMUT performance is still not clear. Sammoura *et al.* firstly modify such model and introduce the effect of residual stress as [81, 160]:

$$D\nabla^2\nabla^2 w(r) - T^s\nabla^2 w(r) + \rho_s \frac{\partial^2 w(r)}{\partial t^2} = \nabla^2 M^p + \nabla^2 M^s \tag{5.4}$$

$$T^s = \int \sigma(z)dz \tag{5.5}$$

where T^s is the overall plate tension caused by the residual stresses, σ is the residual stress at different layers and M^s is the residual moment about the neutral plane. Calculated results of the model indicate that the residual moment imbalance may cause buckling, and even lesser imbalance could adversely affect the transmitting sensitivity. With an overall plate tension of only 1000 N/m (tensile), the deflection per voltage at the center of membrane reduces by 8.4% [160]. It is worth noting that the results do reveal that compressive stress can help to enhance the sensitivity. Some researchers also report that compressively stressed pMUTs with large upwards

buckling have significantly higher transmitting [161] and receiving [162] sensitivities. However, large compressive stress and large buckling make the membrane very fragile. Intentionally introducing compressive stress could lower the yield rate, which is not preferred for volume fabrication. Considering both the performance and reliability, minimizing the overall plate tension and enabling flat membrane may be an effective and reliable way to enhance the transmitting sensitivity of pMUT.

5.1.1.2 Realizing zero-bending membrane

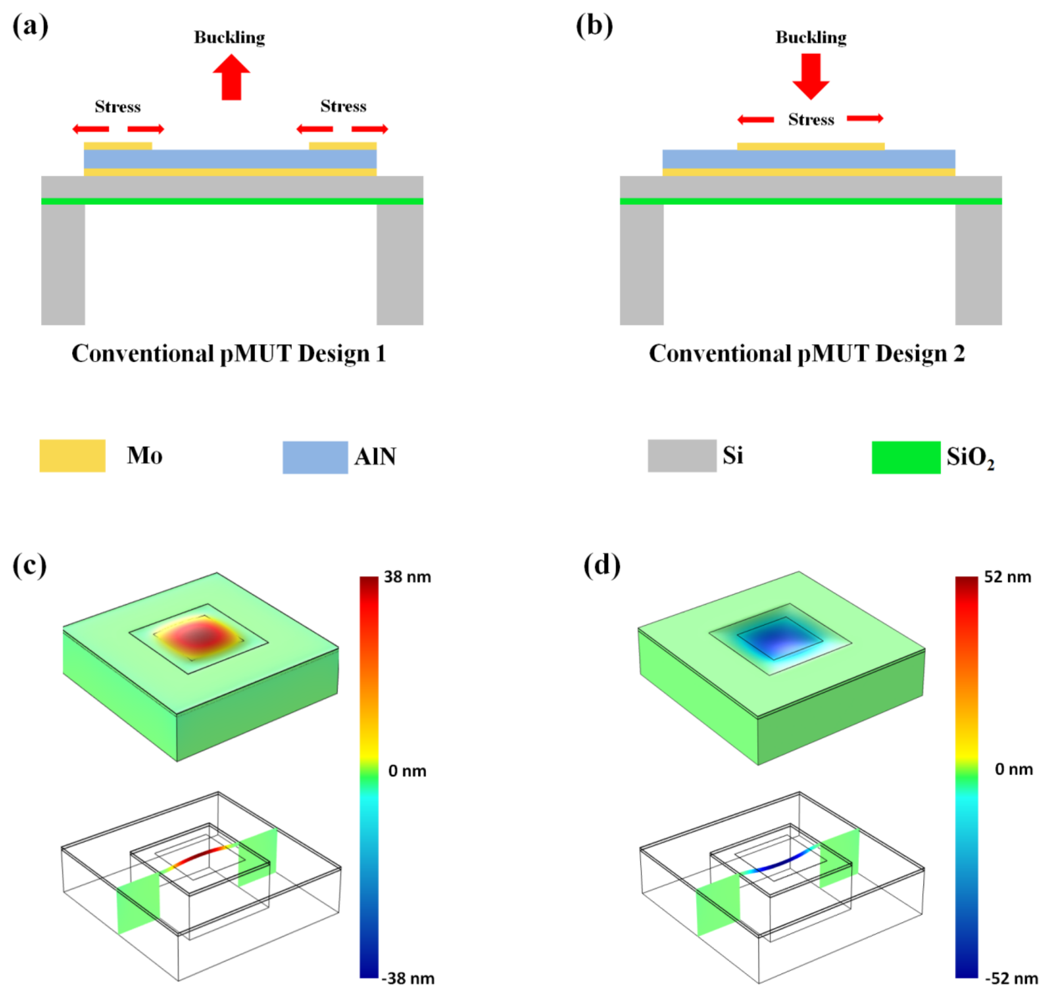

Figure 5.1 Two typical conventional pMUT designs with: (a) Frame-like top electrode; (b) Central top electrode. The simulation results of residual stress induced buckling: (c) Design 1 and; (d) Design 2.

Only the stress-free AlN layer is not sufficient for a high performance pMUT, because the degradation of the transmitting sensitivity is attributed to the residual stress of every layer, according to Eq. (5.5). In addition, the stress distribution also changes because of the buckling, and the stress-free layers may become stressed after buckling. Finally, different designs and structures of pMUT affect the buckling as well. Analysis of the buckling and stress distribution should be considered case by case.

Figure 5.1 (a) and (b) show the two typical designs of pMUT, where the Design 1 has the frame-like electrode, while the Design 2 has the central electrode. According to previous studies, the curvature at the center of deflected membrane has the opposite sign from that at clamped borders. The sign changes at the position of about 65% of the radius [16]. Partially covered top electrode thus has the optimal performance, and both the frame-like electrode (outer) and the central electrode (inner) are identically the best [16, 49]. Therefore these two pMUT designs are adopted for the study.

Table 5.1 Material properties applied in the FEM

Material	Young's modulus	Poisson's ratio	Residual stress	Thickness (μm)
Mo	312 GPa	0.3	470 MPa (Tensile)	0.2
AlN	340 GPa	0.24	~0 MPa	1
Si	170 GPa	0.28	0 MPa	5
SiO_2	60 GPa	0.17	-200 MPa (Compressive)	1

An FEM with a membrane size of 200μm is built using COMSOL Multiphysics software, where the solid mechanics physics is employed. The parameters used for simulation are summarized in Table 5.1. Figure 5.1 (c) and (d) show the simulated

membrane deflections due to residual stresses for Design 1 and Design 2, respectively. With the stress-free AlN layer, the buckling is still not negligible. Such buckling may reversely affect the transmitting sensitivity. It is worth noting that the buckling directions of these two designs are opposite. Although the metal layer is very thin, it usually has very large tensile stress. So the buckling direction is mainly determined by the layout of top metal electrode. Simply removing the backside oxide layer [21], or adding additional oxide layer [16] can hardly alleviate the buckling, or may even worsen the situation. Therefore those trials to improve the pMUT performance are not very successful.

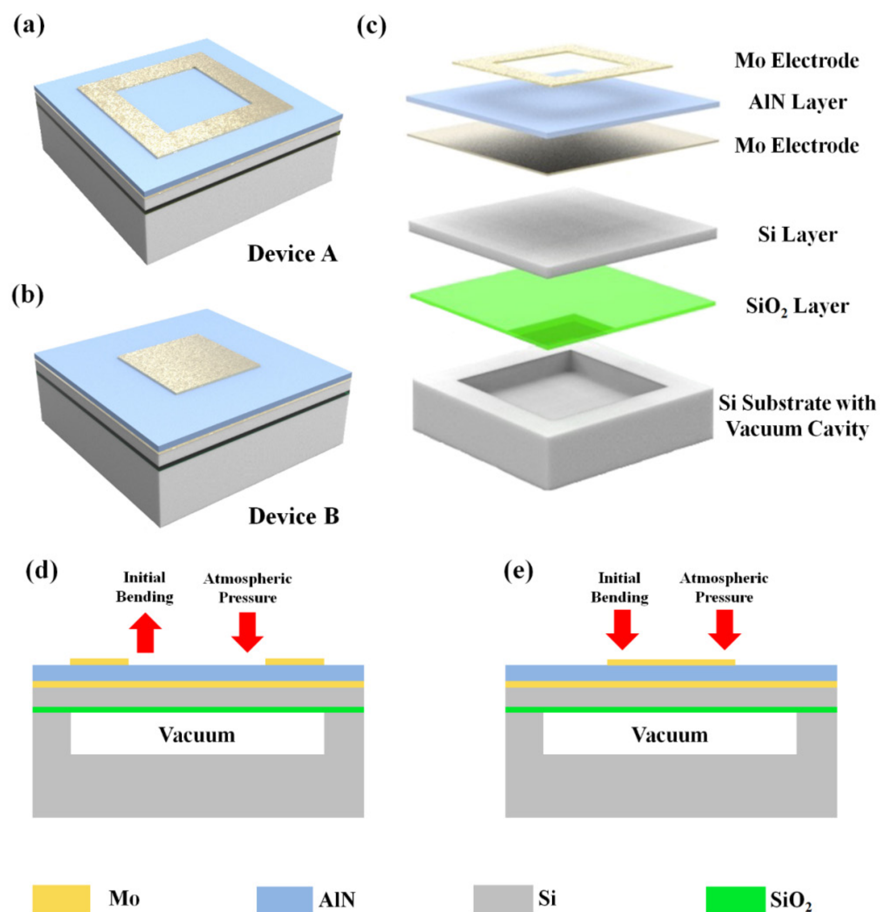

Figure 5.2 3-D schematic drawings of: (a) & (c) the zero-bending pMUT, denoted as Device A; (b) Reference pMUT, denoted as Device B and; (d) & (e) Comparison of Device A and B. Vacuum pressure can compensate the initial bending of Device A, but aggravate the initial bending of Device B.

The 3-D schematic drawings of the zero-bending pMUT are shown in the Figure 5.2 (a) and (c), denoted as Device A. The frame-like top electrode is adopted for the zero-bending pMUT. Compared to the conventional design, an integrated vacuum cavity is fabricated under the membrane. As aforementioned, the pMUT with frame-like top electrode tends to bend upwards due to the residual stress. Meanwhile, the integrated vacuum cavity induces downwards atmospheric pressure, which pushes the membrane back. The initial bending of such pMUT therefore is compensated as shown in the Figure 5.2 (d). Device B with the central top electrode (see Figure 5.2 (b)) is taken as the reference. Since the pMUT with central top electrode tends to bend downwards and the vacuum induced atmospheric pressure is also the same direction, hence cannot balance the initial bending, but aggravates it, shown in Figure 5.2 (e). Although the transmitting sensitivities of Device A and Device B should have been the same, the Device A with flat membrane is expected to have significantly higher sensitivity than the buckled Device B.

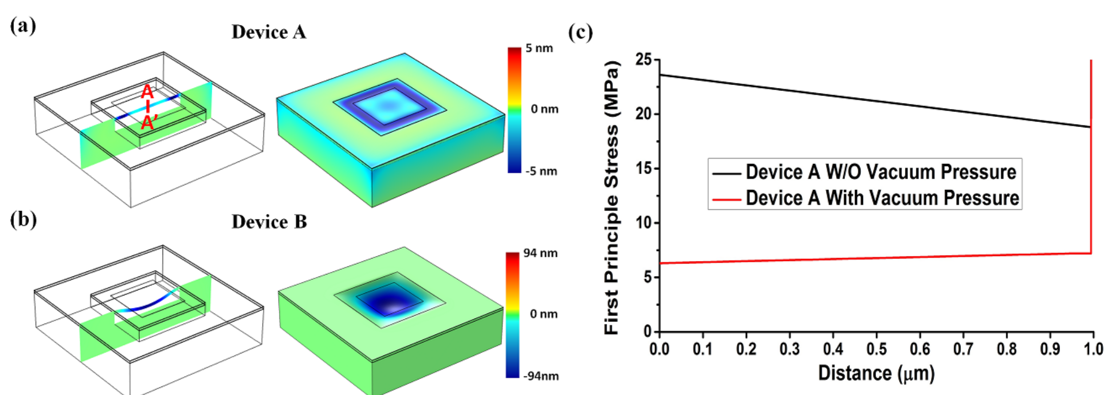

Figure 5.3 Simulation results of membrane deflection: (a) Device A; (b) Device B and; (c) Stress distribution in the AlN layer of Device A along A-A' direction before and after vacuum pressure compensation.

The membrane deflection of Device A is studied by simulation as well. As can be seen from Figure 5.3 (a), the membrane of Device A becomes flat, and the deflection is minimized to less than 5nm. The stress distribution in the AlN layer of Device A along A-A' direction is also extracted and shown in Figure 5.3 (c). The abrupt increasing of stress at 1μm is due to the extremely high initial stress in Mo layer. Despite that the residual stress of AlN layers is set to be zero (see Table 5.1); the simulated stress in the AlN layer is still considerably high, because the initial buckling forces the AlN layer to be re-stressed. If the vacuum pressure is applied to the membrane and it becomes flat after the compensation, the stress in AlN layer significantly reduces to only 6 MPa. With the help of nearly stress-free AlN thin film, frame-like top electrode layout and integrated vacuum cavity, a zero-bending pMUT with minimized stress is possibly available. Figure 5.3 (b) shows the reference pMUT (Device B) with applied vacuum pressure. As expected, it buckles with maximum central deflection of 94nm.

5.1.2 Device characterization and discussion

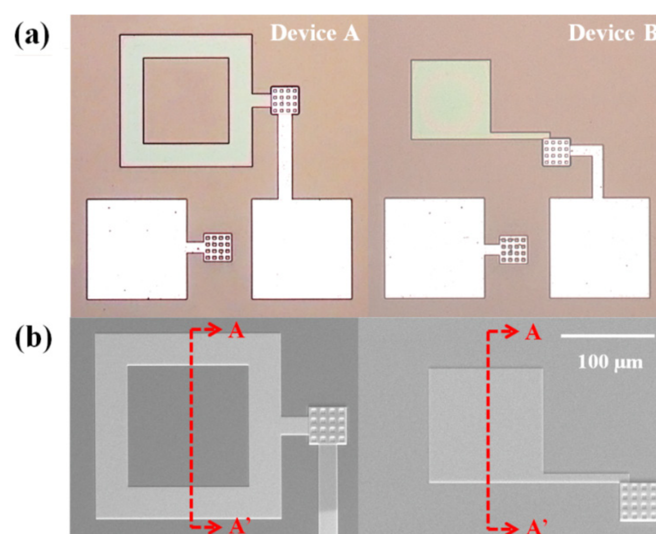

Figure 5.4 The fabricated pMUT devices: (a) OM images and; (b) SEM images.

The as-fabricated zero-bending pMUT (Device A), as well as the reference pMUT (Device B) are shown in Figure 5.4. The integrated vacuum cavity is clearly shown in Figure 5.5, under the pMUT membrane.

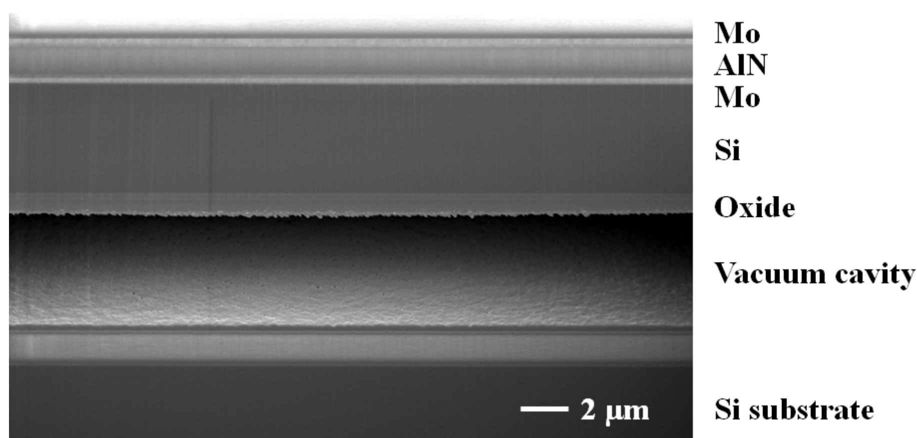

Figure 5.5 The cross-sectional view of SEM image, showing the integrated vacuum cavity.

Both pMUTs are firstly characterized using DHM-R2100 holographic MEMS analyzer by Lyncée Tec Ltd. This MEMS analyzer is able to capture both stationary and dynamic 3-D surface images of the device, with vertical resolution of sub nm level. The surface profile, deflection and dynamic motion of the MEMS device then can be extracted from such 3-D images. Figure 5.6 (a) shows the 3-D images of Device A and Device B. As is expected, the Device A has a flat membrane, while the membrane of Device B is bent downwards. The 200nm steps are the top electrodes. The surface profiles of both devices are also extracted and plotted in Figure 5.6 (b). It is clearly shown that the membrane of Device A is perfectly flat and the 200nm steps are the top electrode. The maximum deflection at the center of membrane is less than 10nm, or less than 0.005% (deflection/membrane size). Benefited from the stress-free AlN thin film, frame-like top electrode and integrated vacuum cavity, the residual

stress induced initial bending is successfully compensated. This extremely small initial bending therefore can be treated as zero bending. On the contrary, the membrane of Device B has a maximum deflection of 96nm. These measured surface profiles match with the simulation results in Figure 5.3 very well.

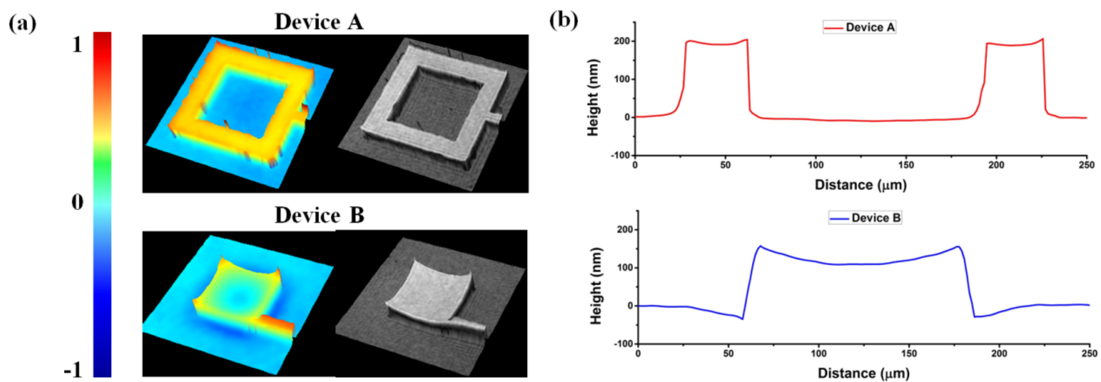

Figure 5.6 (a) The 3-D images captured by holographic MEMS analyzer and; (b) The extracted surface profiles. Maximum deflection of the Device A is less than 10nm, which is considered as zero-bending, and the deflection of Device B is 96nm. The measured profiles match the simulation results very well.

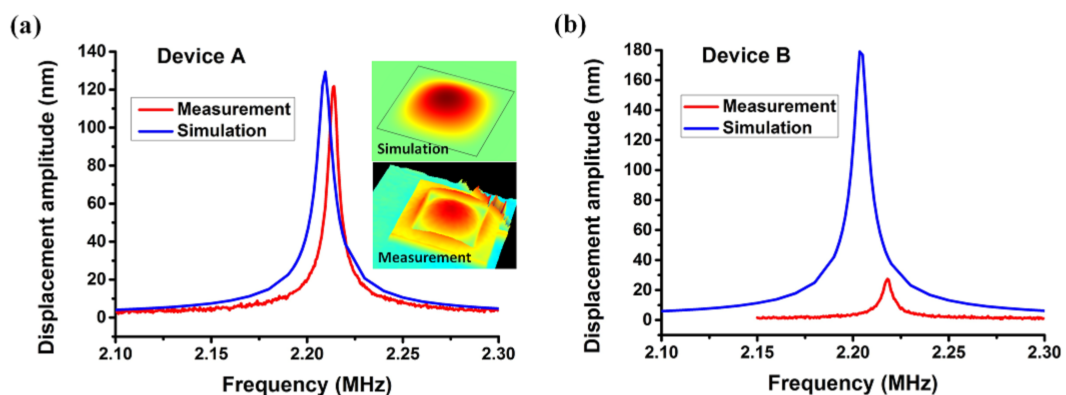

Figure 5.7 Simulated and measured frequency responses of displacement amplitude with 1 V AC excitation for: (a) Device A and; (b) Device B. The inset shows the vibration mode shapes from both simulation and measurement.

The zero-bending pMUT (Device A) then is excited by 1 V electrical AC signals

to evaluate its transmitting performance using the stroboscopic module. The displacement amplitude with frequency is plotted in Figure 5.7 (a). Since all the displacement amplitudes are measured with 1V excitation, the displacement amplitude per volt is also taken as transmitting sensitivity. The results of FEM simulation are shown as well for comparison. The piezoelectric devices physics is employed for this FEM, where the 1μm AlN layer is defined as the piezoelectric material with d_{31} of -1.72pC/N. The remaining parts of the model are defined as linear elastic material with properties shown in Table 5.1. To achieve reasonable results, loss and damping effects are also considered. The loss factor for electrical permittivity (dielectric loss) is set to be 0.01, while the loss factor for damping (linear elastic material) is set to be 0.002. The damping effect is mainly attributed to the anchor loss and air damping. It is worth noting that no initial stresses are considered in this FEM, and hence the simulated transmitting sensitivity is taken as the ideal value. The measured amplitude at the resonant frequency is 123nm, while the simulated amplitude is 129nm. It is clearly shown in Figure 5.7 (a) that the measured curve is very close to the simulation result, which means a nearly ideal transmitting sensitivity is achieved for the zero-bending pMUT. Such pMUT achieves 94.5% of the ideal transmitting sensitivity.

In terms of the reference pMUT (Device B), however, the transmitting sensitivity is much poorer than the zero-bending pMUT, shown in Figure 5.7 (b). As aforementioned, theoretically these two devices should have the same transmitting sensitivity, and is also proven by simulation results. Unfortunately, the reference pMUT fails to achieve a comparable transmitting sensitivity with the zero-bending pMUT, which largely deviates from the ideal performance. The displacement

amplitude of the reference pMUT is measured as only 27nm, or 22% of the zero-bending pMUT. Such performance degradation is mainly because of the non-zero initial bending (Figure 5.6). The slightly higher resonant frequency of the reference pMUT also indicates its membrane stress is larger than the zero-bending pMUT, as the membrane stiffness is increased due to the stress. Therefore, the zero-bending pMUT is proven to perform much better than the reference pMUT, with enhanced transmitting sensitivity of more than 450 % with respect to the reference pMUT.

Table 5.2 Comparison of the transmitting sensitivity

Device	Size (μm)	Thickness (μm)	Transmitting Sensitivity (nm/V)	Sensitivity per Area ($nm/V/mm^2$)
This work	200	7.4	123	3075
Ref. [163]	190	3.3	45	1587
Ref. [151]	350	2.4	210	2182
Ref. [164]	400	7.7	40	318
Ref. [165]	400	2.3	60	477
Ref. [69]	400	2.3	250	1989
Ref. [62]	1456	3.2	450	270
Ref. [66]	25	1.5	2.5	5092*

* Extremely thin membrane

Table 5.2 summarizes previously reported AlN based pMUT devices. In general, the zero-bending pMUT presented in this work performs much better than most of other pMUTs. Especially for the pMUTs reported in Ref. [163] and [164], those highly responsive pMUTs employ sophisticated 3-D membrane structure to further

enhance the sensitivity, the sensitivity of the zero-bending pMUT is still twice and 10 times of the pMUTs in [163] and [164], respectively. It is worth noting that the pMUT in Ref. [66] has very high sensitivity. This may be due to the extremely thin membrane. Since its AlN and supporting SiO_2 layers are only 0.75μm and 0.8μm, its ideal transmitting sensitivity should be much higher than the zero-bending pMUT (1μm AlN, 5μm Si and 1μm SiO_2). A FEM simulation is performed to investigate its ideal sensitivity using the above parameters. Simulation results indicate that the pMUT in Ref. [66] can potentially achieve a sensitivity of 14nm/V, or 28520nm/V/mm^2. In fact, such pMUT only achieves 18% of its ideal sensitivity, which is significantly lower than the 94.5% of zero-bending pMUT.

Figure 5.8 shows the impedance measurement results of the zero-bending pMUT, performed using Agilent 4294A precision impedance analyzer. The electromechanical coupling coefficient k_{eff}^2 can be derived from resonant frequency f_r and anti-resonant frequency f_a through following relation [166]:

$$k_{eff}{}^2 = \frac{f_a^2 - f_r^2}{f_a^2} \tag{6}$$

This parameter directly reflects the electrical-mechanical energy conversion efficiency of the device. The in-air k_{eff}^2 is calculated as 0.406%. Such value is significantly better than a previously reported AlN based pMUT, where the measured coefficient is only 0.056% [151]. Considering the zero-bending pMUT is wire-bonded for testing, the coupling coefficient may be further improved by eliminating the parasitic capacitances from bonding pads and wires. As is shown in Figure 5.8 (b), the zero-bending pMUT also performs well in DI-water. The resonant frequency drops to 1.04 MHz, which is still within the commonly used frequency range.

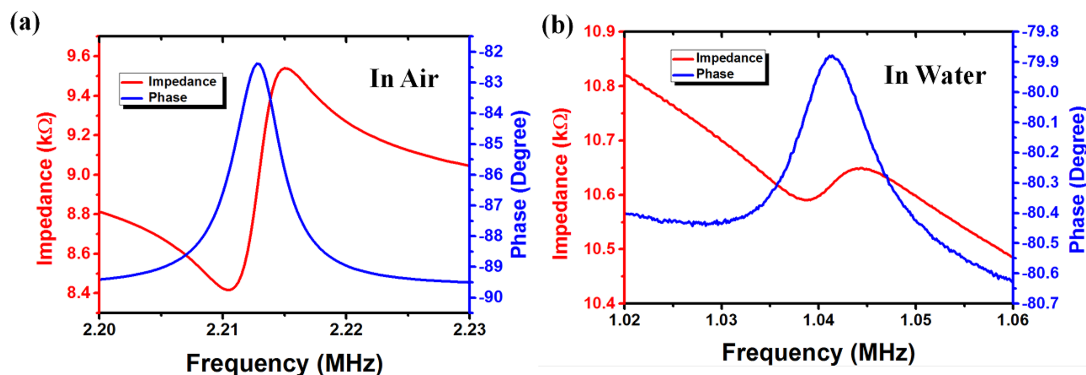

Figure 5.8 The impedance measurement results of the zero-bending pMUT (Device A): (a) measured in air and; (b) measured in DI water.

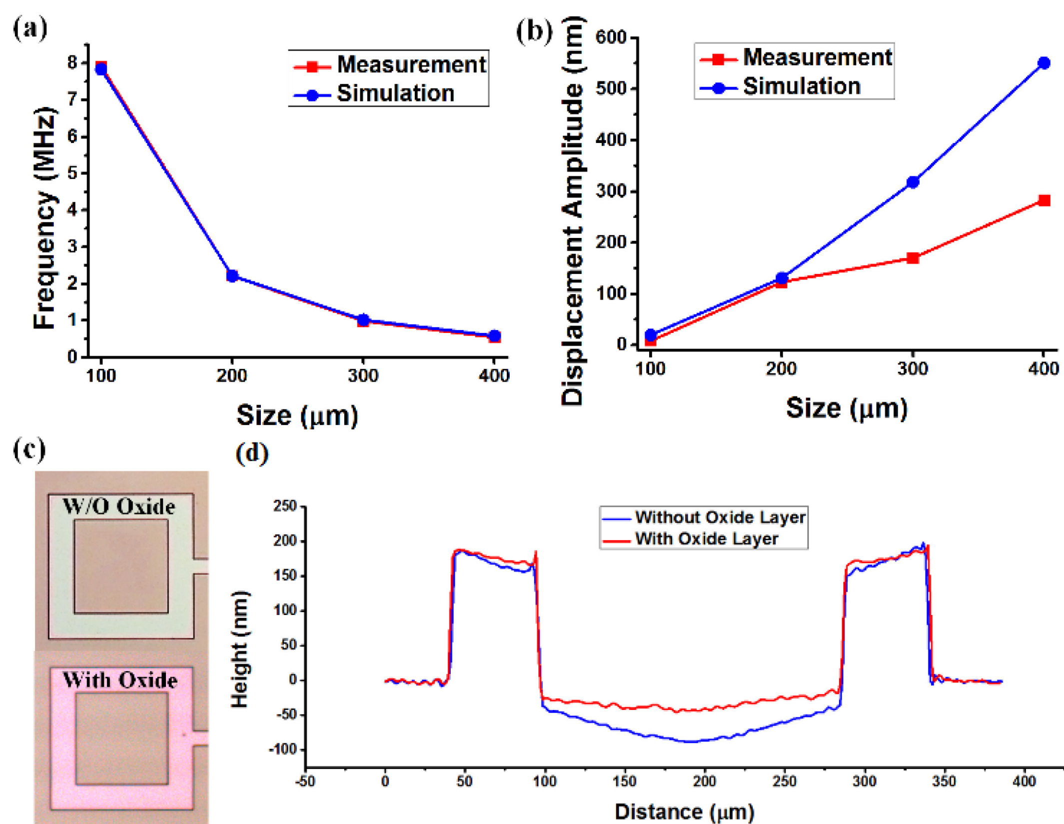

Figure 5.9 Simulation and measurement results of the pMUTs (frame-like top electrode) with different sizes: (a) The resonant frequency and; (b) The displacement amplitude. The 300μm pMUTs with and without 0.7μm oxide layer: (c) Optical microscope images and; (d) measured surface profiles.

The pMUTs (frame-like top electrode) with different sizes are fabricated and

studied as well. As can be seen from Figure 5.9 (a), the resonant frequency decreases with the size as expected, and agrees very well with the simulation results. However, for the displacement amplitude, the measurement results start deviating from the simulation results at 300μm, and such deviation increases with the membrane size (see Figure 5.9 (b)). The 300μm and 400μm pMUTs are not able to achieve the best transmitting sensitivity as the 200μm pMUT. To investigate the reason of the performance degradation, the 300μm pMUT is taken as an example. Its surface profile is extracted and shown in Figure 5.9 (d). As is shown, such device is no longer a zero-bending pMUT, but with a maximum membrane deflection of 88nm. Because the vacuum force is proportional to the membrane area, it increases with the membrane size. Meanwhile, the residual stress in membrane remains a constant. Therefore the significant initial buckling is observed for 300μm pMUT. The performance degradation is probably due to such initial buckling. As expected, the vacuum force of the 400μm pMUT is even larger, and hence the performance degradation becomes more severe for the 400μm pMUT.

To alleviate this performance degradation, another batch of devices is also fabricated. For these devices, the last step of process, *i.e.* blank etching of the top oxide layer, is skipped. Compared to previous discussed pMUT, additional 0.7μm PECVD oxide layer is left on the surface. As is shown in Figure 5.9 (c), the color of the Mo electrode changes from green to purple, because of the oxide thin film. Since the oxide layer usually contains compressive stress, it forces the membrane to bend upwards. Therefore, the additional oxide layer may help to reduce the downwards initial bending. Figure 5.9 (d) shows the surface profiles of 300μm pMUTs with and without oxide. With the help of the top oxide layer, the maximum membrane

deflection reduces to 42nm. Although this pMUT is not perfectly zero-bending, the performance degradation should be alleviated due to the relatively flat membrane. Figure 5.10 shows the transmitting sensitivity of the 300μm pMUTs, with and without top oxide layer. Benefited from the relatively flat membrane, the pMUT with oxide layer achieves 69.19% of ideal sensitivity, which is 13% better than the pMUT without oxide. Hence, if a larger membrane is required for lower operation frequency, additional top oxide layer may be applied to minimize the performance degradation.

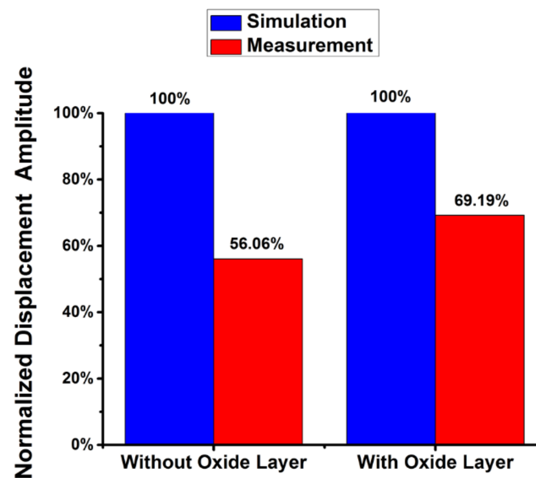

Figure 5.10 Transmitting sensitivity comparison of 300μm pMUTs: (a) without top oxide layer and; (b) with top oxide layer. The displacement amplitude is normalized to the simulation result, i.e. the ideal displacement amplitude.

5.2 pMUT with Piston-Like Membrane Motion

Another possible method for increasing the transmitted ultrasound pressure is to enable a piston-like membrane motion. Usually the classical pMUT has a Gaussian-like mode shape. For such mode shape, only the center of membrane is able to achieve the maximum displacement amplitude. If a piston-like mode shape can be

realized, the membrane remains flat during vibration, and larger portion of membrane can oscillate with the maximum amplitude. Hence more acoustic medium (*e.g.* air, water, or soft tissue) can be pushed back and forth, generating higher ultrasonic pressure. The piston-like vibration has been realized with a cMUT, which is proven to offer several advantages [167]. However, reported pMUT with piston-like membrane motion is very limited.

5.2.1 Concept and design

5.2.1.1 Perforated membrane

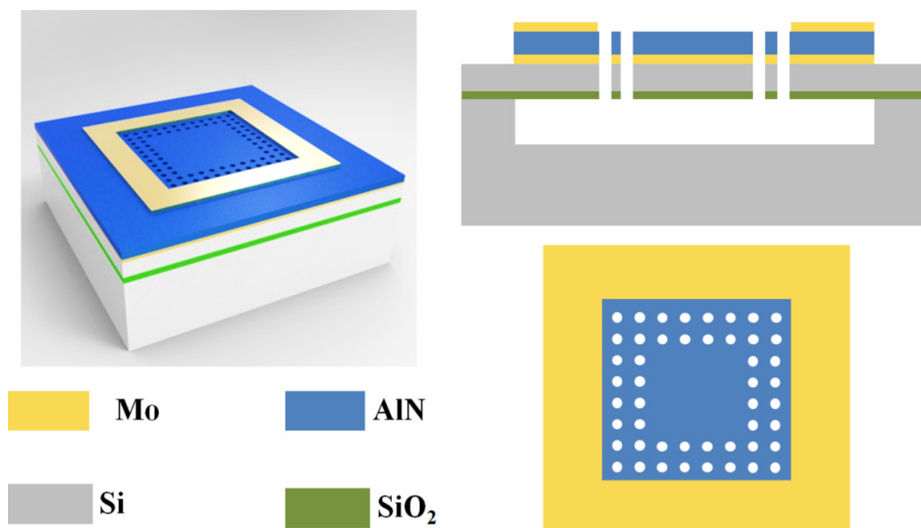

Figure 5.11 Illustrations of the piston-like pMUT. The etching holes located inner top electrode, are through all layers.

The structure of the proposed piston-like pMUT is illustrated in Figure 5.11. The frame-shaped top electrode partially covers the surface, with coverage of 35%. This top electrode design ensures the maximum electromechanical coupling for pMUT [65]. In order to realize piston-like mode shape, stiffness difference should be introduced to the membrane. One reported approach is to attach an additional silicon

mass on the center of membrane to stiffen the central portion of membrane [167]. But this may be only suitable for cMUT. Wafer bonding and handle wafer removal processes are employed to realize the silicon mass, which is not standard or necessary processes for pMUT. In addition, the composite membrane of pMUT is relatively thick, and hence the additional mass has to be even thicker to enable the piston-like mode shape. This may bring in undesirable effects on the frequency and performance.

Therefore, in this work a new approach is proposed to introduce the stiffness difference. Compared to the classical pMUT, 5 μm etching holes are fabricated inner the top electrode, which are through the released membrane as shown in Figure 5.11. The perforated portion becomes more flexible and most of the deflection is confined within this softened region. Benefited from such softened region, the central ridged region hence suffers small deflection and remains flat. The central region moves up and down like a piston during vibration.

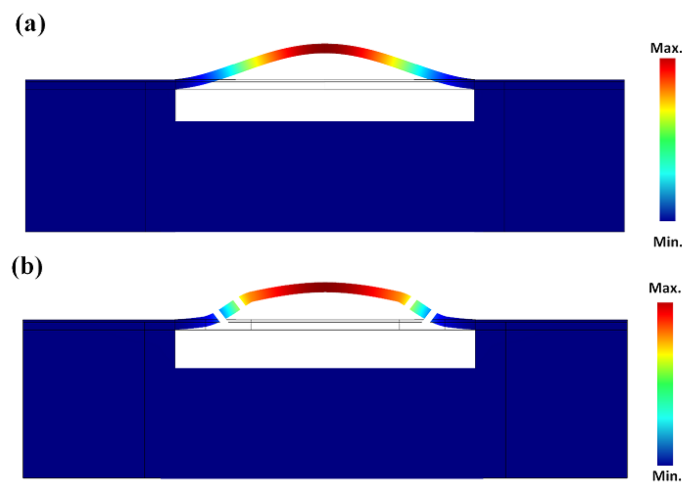

Figure 5.12 Simulated mode shapes by FEA modeling: (a) classical pMUT and; (b) piston-like pMUT. With the help of etching holes, the mode shape has a relatively flat surface.

Figure 5.12 shows the simulated mode shapes using FEA model by COMSOL. The mode shape of classical pMUT is shown in Figure 5.12 (a), which is

Gaussian-like. Meanwhile, with the help of etching holes, the membrane surface becomes relatively flat, shown in Figure 5.12 (b).

5.2.1.2 Advantages of using etching holes

To avoid the ventilation of two sides of the membrane, the etching holes need to be finally sealed. The 5μm etching holes ensure that they can be sealed by a thin polymer layer. According to previous studies, neither Parylene [66] nor PDMS [168] thin film on the surface affects the pMUT performance largely. For the piston-like pMUT reported in [165], the SiO_2 layer is intentionally not fully etched and 0.02μm SiO_2 is left to avoid ventilation. However, without pre-designed stop layer, such thin SiO_2 layer can nearly be ensured using time control. Once the SiO_2 is etched through, the large trenches may not be able to re-seal. In addition, as the membrane in [165] is supported by three beams, its resonant frequency is significantly lowered than classical pMUT. Higher frequency for diagnostic ultrasonic imaging (2 to 10 MHz) may be difficult to realize with such design. The etching holes, however, nearly influence the resonant frequency of pMUT. Hence, employment of etching holes to enable piston-like membrane motion is a more advantage approach.

5.2.2 Device characterization and discussion

The fabricated pMUTs are shown in Figure 5.13 (a) and (b). The pMUTs with two and three rows of etching holes are denoted as *Device B* and *Device C*, respectively. A classical pMUT without etching holes is also fabricated for reference, denoted as *Device A*. Figure 5.13 (c) shows the etching holes through the membrane, with diameter of 5μm. Such small diameter ensures the holes are able to be re-sealed. The cross-sectional view of the membrane is shown in Figure 5.13 (d), which contains

0.2μm Mo, 1μm AlN, 5μm Si and 1μm SiO_2. All the pMUTs share the same dimension of 200μm.

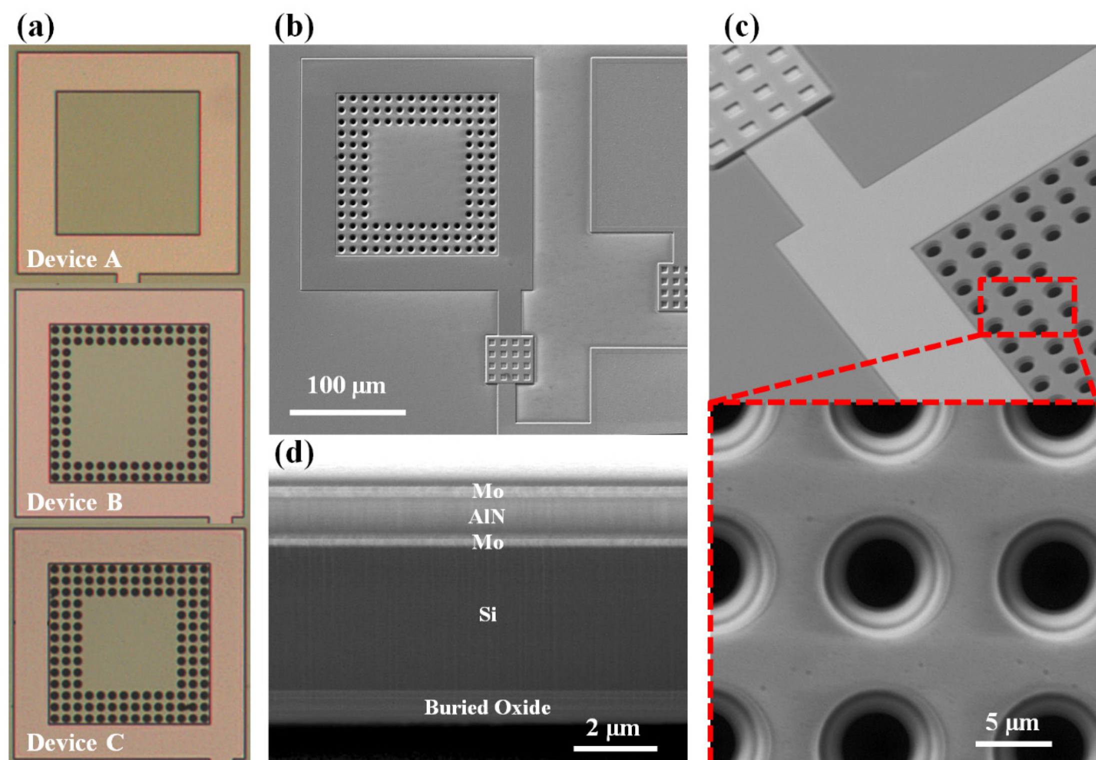

Figure 5.13 (a) The optical microscope images of fabricated pMUTs. The classical pMUT is denoted as Device A, and the piston-like pMUTs with two and three rows of etching holes are denoted as Device B and Device C, respectively; (b) the SEM image of Device C; (b) SEM images showing the etching holes and; (d) cross-sectional view of pMUT membrane.

Digital holographic MEMS analyser (DHM-R2100 from Lyncée Tec) is employed for device characterization. Surface profiles of *Device A* to *C* at their resonance are extracted and plotted in Figure 5.14 (a). As is expected, the mode shapes of *Device B* and *C* become much flatter. For *Device B*, its profile at maximum deflection is still slightly curved; meanwhile the profile of *Device C* remains flat at the maximum deflection. Comparison of the surface profiles (*Device C* and *A*) is

shown as well. It is clearly shown that larger portion of membrane is able to achieve the maximum amplitude for *Device C*. Captured 3-D images of *Device C* are shown in Figure 5.14 (b) as well, and the central region of membrane moves like a piston.

Frequency responses of displacement amplitude with 1 V excitation are shown in Figure 5.14 (c). Considering the 2.24 MHz resonant frequency of *Device A*, frequency of the piston-like pMUT does not decrease but slightly increases. This is mainly attributed to the etching holes and their location. When the membrane of a classical pMUT deflects, the portion covered by top electrode has the largest strain, while the portion inner the electrode has minimum strain [65]. Therefore, etching holes locating inner top electrode have minimum influence on the spring constant of the membrane. On the other hand, since part of the membrane is etched, its mass reduces accordingly. Resonant frequency hence slightly increases with the number of etching holes (2.29 MHz and 2.31 MHz for *Device B* and *C*, respectively). For such piston-like pMUT using etching holes, the resonant frequency can be predicted by well-established analytical and FEA models prior to fabrication, and higher frequency for diagnostic ultrasonic imaging (2 – 8 MHz) is able to be realized by changing the dimension. In contrast, for the piston-like pMUT reported in [165], the grooves locate where the membrane has largest strain, which significantly lowers the spring constant and results in much lower frequency. Figure 5.14 (c) provides the comparison of the three devices. The relatively higher displacement amplitude of *Device A* could be caused by less air damping. The lower Q in *Device B* and *C* should be attributed to the larger effective vibration area, which results in larger damping. The two piston-like pMUTs do not show significant difference in Q factor, and therefore the higher displacement sensitivity of *Device C* is not caused by larger Q. In fact, Q factor of *Device C* is slightly lower than *Device B*, which may be resulted from more etching holes and

more air damping. Considering the flatter mode shape of *Device C*, piston-like pMUT with three rows of etching holes is a superior design.

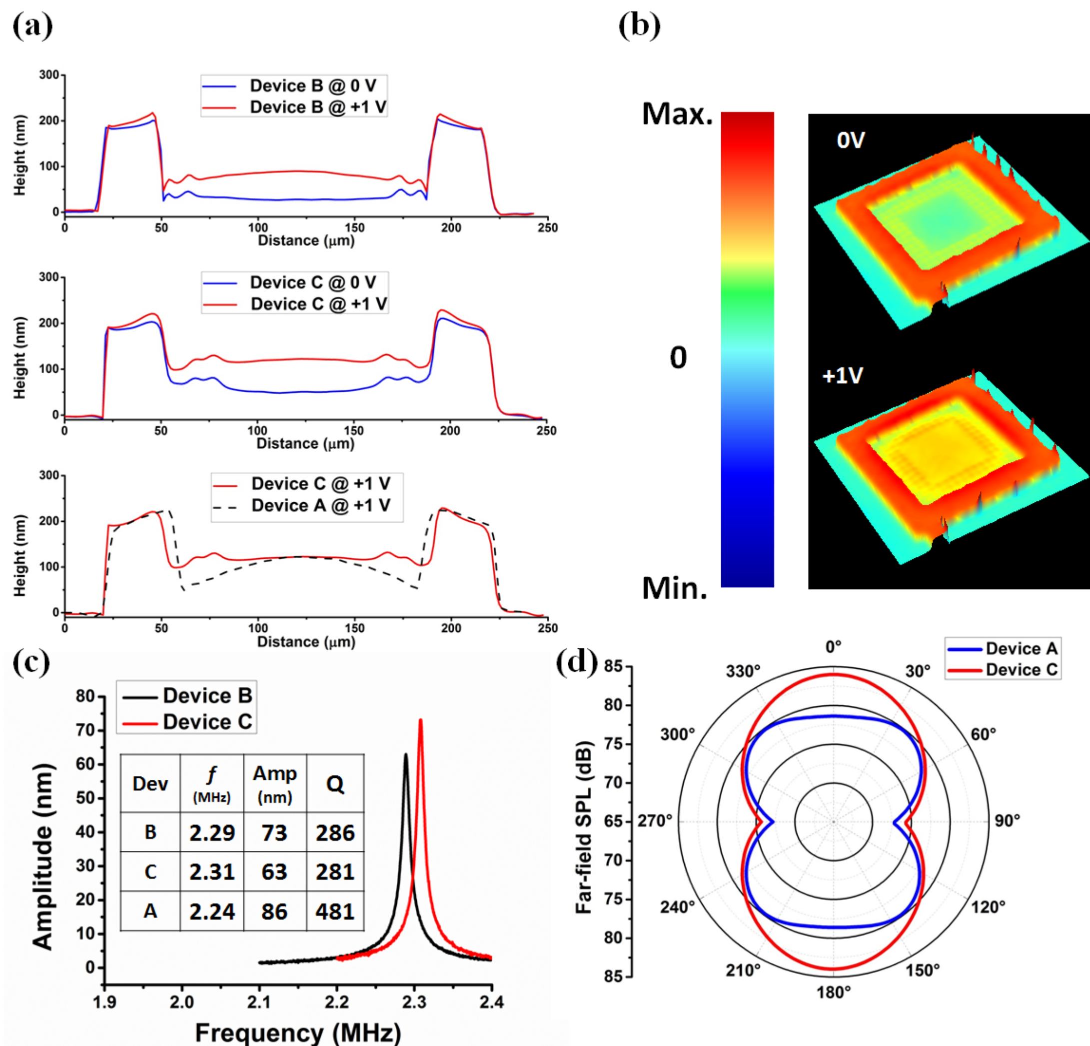

Figure 5.14(a) Surface profiles of the pMUTs at resonance; (b) 3-D images of *Device C*; (c) frequency responses of displacement amplitude for piston-like pMUT. Inset table shows the comparison of the three devices and; (d) simulated far field space pressure levels for *Device A* & *C*.

Acoustic-piezoelectric interaction model is also built to evaluate the performances of *Device C* & *A* in water, and the simulation results are shown in Figure 5.14 (d). Benefited from the piston-like membrane motion, the directivity of

Device C is better than *Device A*, and the far field space pressure level (SPL) of *Device C* is 5.3 dB higher than *Device A*. The receiving sensitivity is studied by applying 1 kPa acoustic pressure to the water medium, where the dimension of water is over 10 λ to eliminate unwilling interferences. The receiving sensitivity of *Device C* at resonance is obtained as 95 mV/kPa, while *Device A* shows receiving sensitivity of 48 mV/kPa based on the modeling data.

5.3 Summary

Residual stress and initial buckling could suppress the transmitting sensitivity of pMUT. Although pMUT with large compressive stress and large upwards buckling exhibit high sensitivity, it may not be preferred for volume fabrication due to the fragility and lower yield rate. Several trials to minimize the stress and buckling are made by different research groups during last decades; there is still a room for innovative design with significant improvement. This is the very reason that pMUT has not been commercialized today due to that performance of current approaches is not satisfactory, and hence the applications are very limited as well. In this chapter, a new pMUT device is proposed. Leveraging on the stress-free AlN thin film, frame-like top electrode layout and the integrated vacuum cavity, a pMUT with zero-bending membrane is finally achieved. The transmitting sensitivity is measured as 123nm/V, which is 450% better than that of reference pMUT with non-zero initial bending. Such pMUT achieves 94.5% of its ideal transmitting sensitivity. By thinning the supporting layer, *i.e.* the device Si layer, the transmitting performance may be further enhanced.

Another approach of enhancing the performance is to realize a pMUT with piston-like membrane motion. Etching holes are applied to pMUT membrane.

Measurement results show that the mode shape of such pMUT has a flat surface. The resonant frequency does not decrease like prior reported piston-like pMUT, but slightly increases by 2 %. This implies that higher frequency for diagnostic ultrasonic imaging can be realized, and the frequency can be predicted using well-established analytical and FEA models. Piston-like pMUT with two- and three- rows of etching holes are studied as well. The pMUT with three rows of etching holes has flatter mode shape, and its transmitting sensitivity is 10nm/V higher, which is superior to the pMUT with two rows of etching holes. Compared to a classical pMUT, the piston-like pMUT with three rows of etching holes is of better directivity, which has almost doubled transmitting and receiving sensitivities.

In conclusion, the two approaches are proven to be effective and reliable ways to enhance the pMUT performance, and the innovative pMUTs may be promising alternatives for future ultrasonic applications.

Chapter 6 Towards PZT Based High Performance pMUT

Piezoelectric material as the key component largely affects the performance of pMUT. Generally, AlN and PZT are the two most popular piezoelectric materials for pMUT. Because of its compatibility with CMOS process, AlN based piezoelectric MEMS devices become popular in recent years [110, 169-171]. Nevertheless, since PZT has the much higher piezoelectric constant d_{31} than AlN, it is still the best choice to realize high performance pMUT for practical use [172-177]. For the PZT thin film, electric poling is a critical process, where usually a DC electric field of 10–100 kV/cm is applied to the PZT thin film. Especially for the most popular sol-gel method, the deposited PZT thin film has very limited initial d_{31}. Thus the final d_{31} is mainly determined by the poling process. According to our previous study, the d_{31} after poling could be drastically lowered by following micro fabrication processes [91], so the suitable poling process step is after completion of MEMS microfabrication processes [90]. As is discussed in Section 2.1.2, the newly developed unipolar pulse poling process is found to be much more effective than conventional DC poling, resulting in a much higher d_{31} coefficient. Leveraging on this process, a high performance pMUT array aiming at volume production is proposed in this chapter. With the optimized design and fabrication process, the pMUT shows a displacement sensitivity of 807nm/V at its resonant frequency (482 kHz). A single pMUT element is able to generate 63.7 dB SPL at 10 mm in air with only 2V input. Such pMUT could be potentially used for range finding or airborne gesture recognition in portable

electronics.

6.1 pMUT Design and Optimization

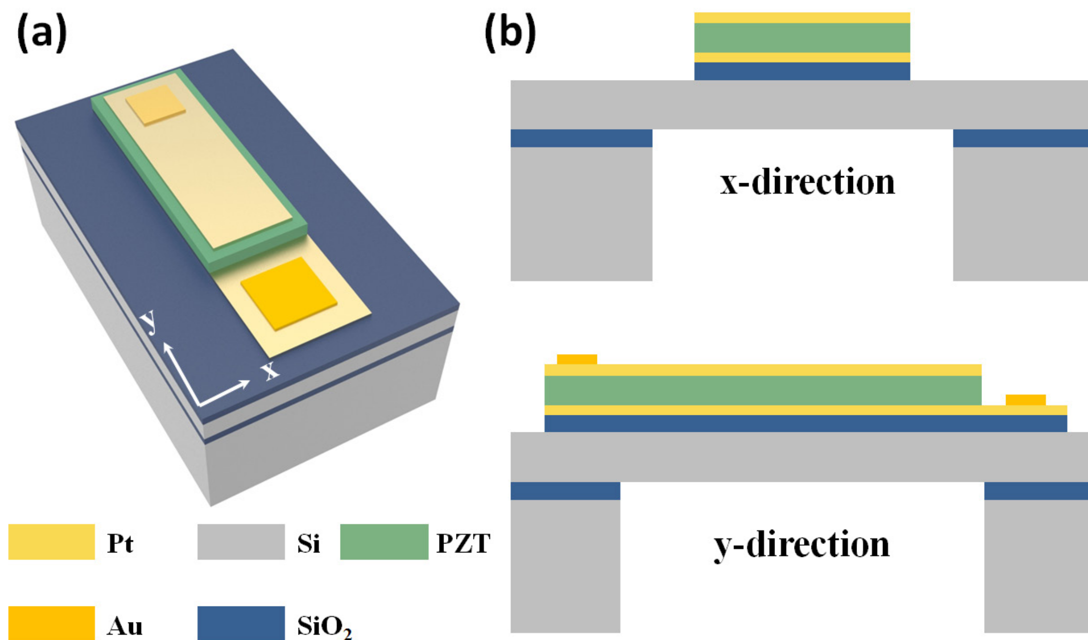

Figure 6.1 Schematic drawings of the proposed high performance pMUT: (a) 3-D illustration and; (b) cross-sectional view of illustration.

The schematic drawings of the pMUT are illustrated in Figure 6.1. The released diaphragm has the dimension of 500μm×300μm. 2μm MPB-PZT thin film is employed because of its high piezoelectric constant, and 1μm SiO_2 is used for isolation. According to previous studies, the position of neutral plane, which is related to the silicon thickness, largely affects the electromechanical coupling [65, 155]. If the neutral plane falls into PZT layer, the lower part of PZT works against the upper part, and this may drastically worsen the pMUT performance. The silicon thickness thus should be carefully chosen. A 3-D FEA piezoelectric device model is built to study the influence of silicon thickness. Driven by input voltage, the normalized membrane

displacement with respect to the silicon thickness is shown in Figure 6.2 (a). The maximum displacement can be achieved with 1.8μm silicon layer. As a compromise of performance and yielding rate, 5μm silicon layer is adopted for the proposed pMUT.

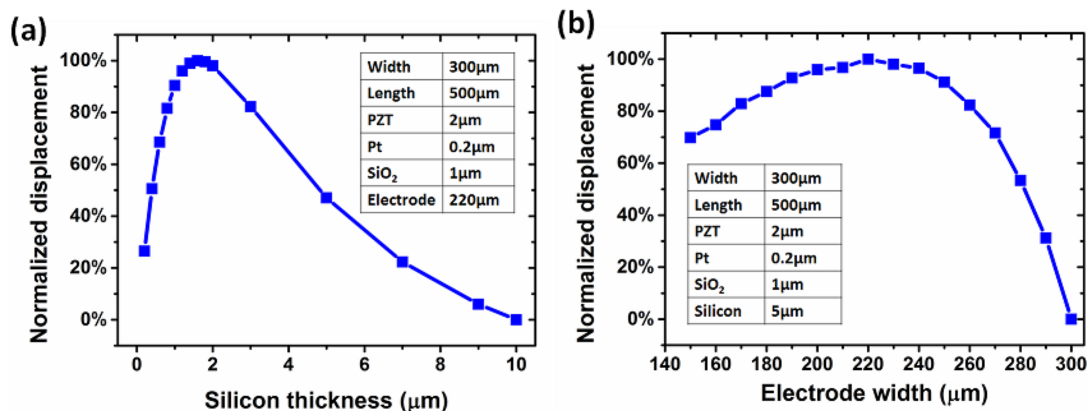

Figure 6.2 The FEM results for pMUT design optimization: (a) normalized displacement with respect to silicon thickness and; (b) normalized displacement with respect to top electrode width.

Since the edges of the membrane are clamped, its curvatures at the center and edge have the opposite signs when the membrane is deformed [65]. The best efficiency hence cannot be achieved with a fully covered top electrode. To optimize the top electrode, the normalized membrane displacement with respect to the top electrode width is plotted in Figure 6.2 (b). It is clearly shown that partially covered top electrode enables a much higher displacement than the fully covered electrode (300μm width). Largest displacement achieves at electrode width of 220μm, and this is the position where the curvature sign becomes zero. Although the length of top electrode should be smaller than membrane as well, the top electrode (y-direction) exceeds the membrane because the bonding pad cannot be on the released structure (see Figure 6.1 (b)). This configuration definitely sacrifices some pMUT performance.

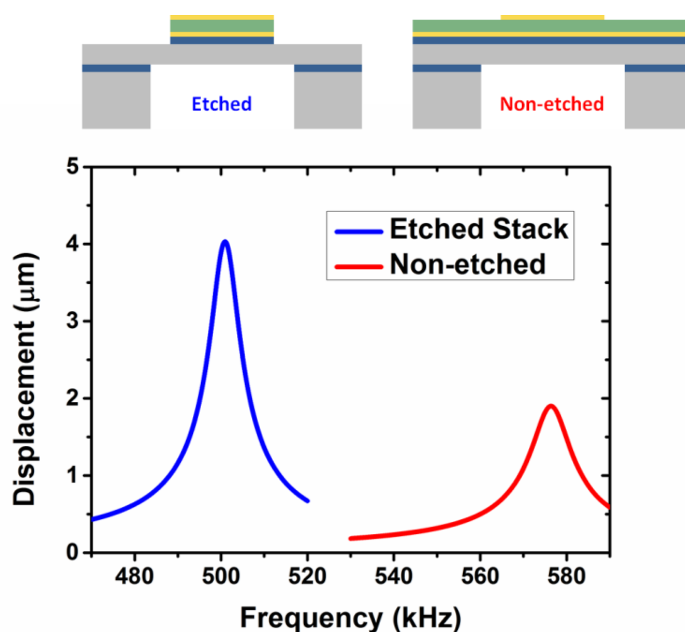

Figure 6.3 Comparison of the pMUTs with etched PZT/Pt/SiO_2 stack and without the etched stack. The FEA modeling results indicate that the pMUT with etched stack has about twice higher sensitivity.

For most of the reported pMUTs, only the top electrode is patterned to simplify the microfabrication processes [69, 151, 166, 168], *i.e.* the PZT layer, bottom electrode and isolating SiO_2 layer remain as shown in Figure 6.3. For the proposed pMUT in this work, however, all the layers are etched to further enhance its performance. Leveraging on the FEA modeling, the performances of the pMUTs with and without etching the PZT and SiO_2 layers are evaluated. Both models use the optimized parameters with 1V excitation. As shown in Figure 6.3, the pMUT with the patterned PZT and SiO_2 layers shows superior displacement sensitivity at its resonant frequency, which is about 2.2 times higher than the non-etched pMUT. Such performance enhancement may be attributed to the change of boundary condition at the edge. Since the PZT and SiO_2 layers are etched, part of the membrane edges become free and only the Si layer is clamped. The etched pMUT also shows a lower

frequency, which implies a smaller elastic constant due to the partially free membrane edges. This helps the membrane to vibrate easily and therefore enlarges the displacement sensitivity. With all the design considerations, the proposed pMUT is optimized to achieve its best performance.

6.2 Experimental Results and Discussions

6.2.1 Device characterization

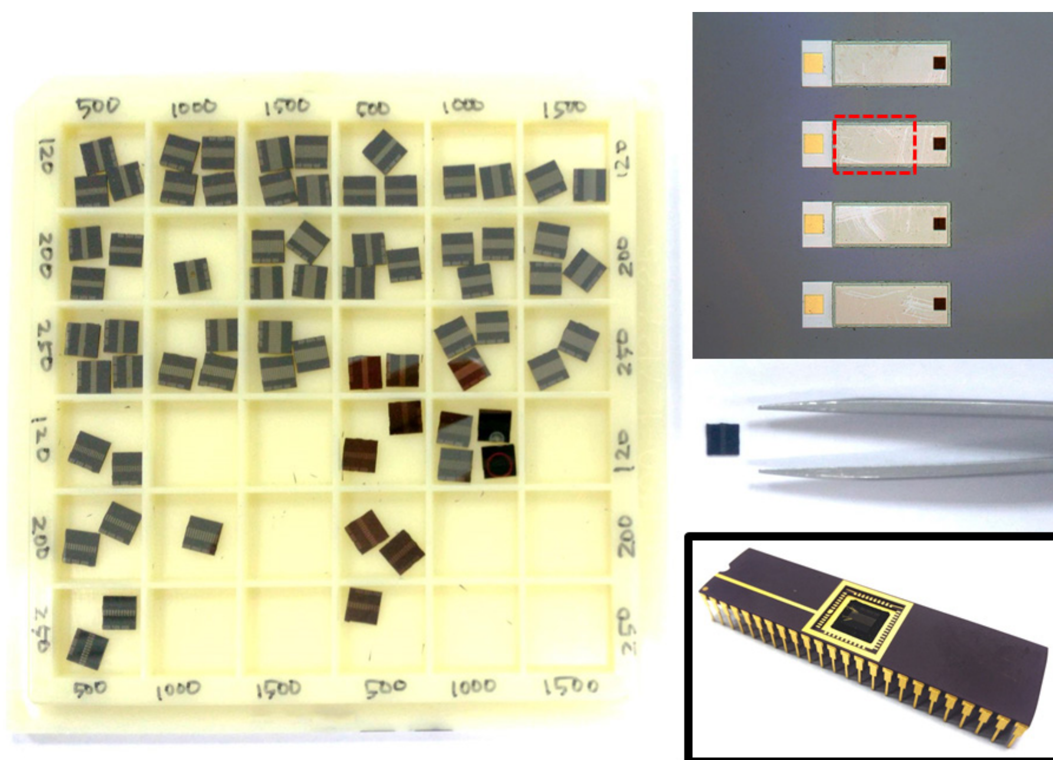

Figure 6.4 The as-fabricated pMUT devices. The red dash lines in optical microscope image indicate the released membrane, which is slightly wider than top electrode to achieve the best performance. The inset shows the pMUT with dual in-line package (DIP) for testing.

The as-fabricated pMUT devices are diced into 4.5mm×4.5mm and each die contains 11 pMUT elements, shown in Figure 6.4. The red dash line in the optical

microscope image indicates the released pMUT membrane. The cross-sectional view SEM images are shown as well in Figure 6.5. It is shown that the top electrode and the PZT stack partially cover the released membrane, which ensures the maximum performance. In addition, the BOX layer is removed completely. According to the simulation result in Figure 6.2 (a), any increased thickness may further lower the pMUT performance. The top view SEM images are shown in Figure 6.6. Zigzag edges can be found for the PZT thin film as it is patterned using wet etching. To avoid the possible short circuit between top and bottom electrodes though the PZT thin film, the PZT/Pt/SiO_2 stack is intentionally larger than the top electrode. The top electrode maintains the optimized 220μm width, and hence the slightly larger PZT/Pt/SiO_2 stack has minimum reverse effects on the pMUT performance. This fabricated pMUT fulfills all the design requirements to achieve its optimized performance.

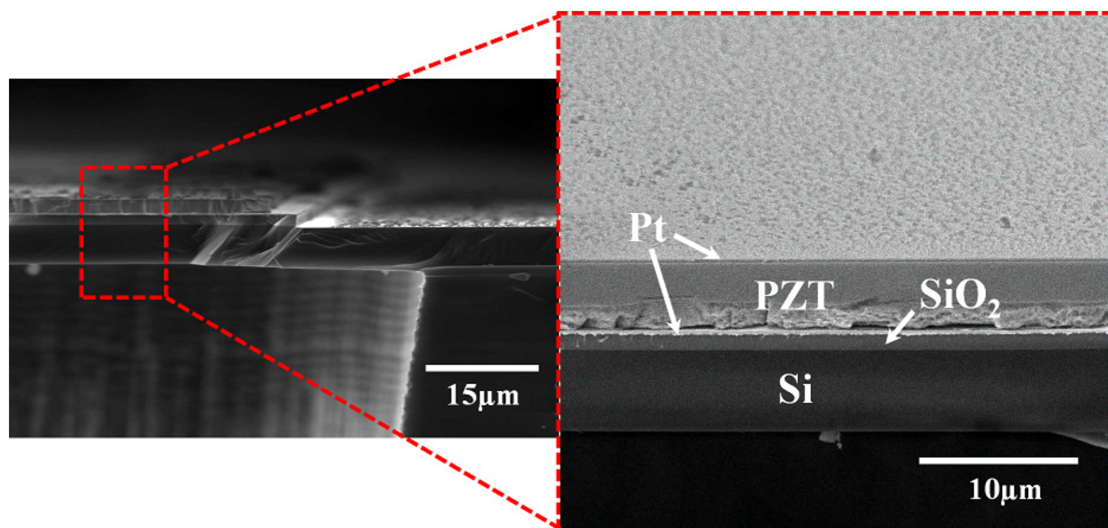

Figure 6.5 The cross-sectional view of the SEM image. It is clearly shown the BOX is completely removed and the top electrode and PZT stack partially covers the released membrane. This fabricated pMUT fulfills all the design requirements to achieve its optimized performance.

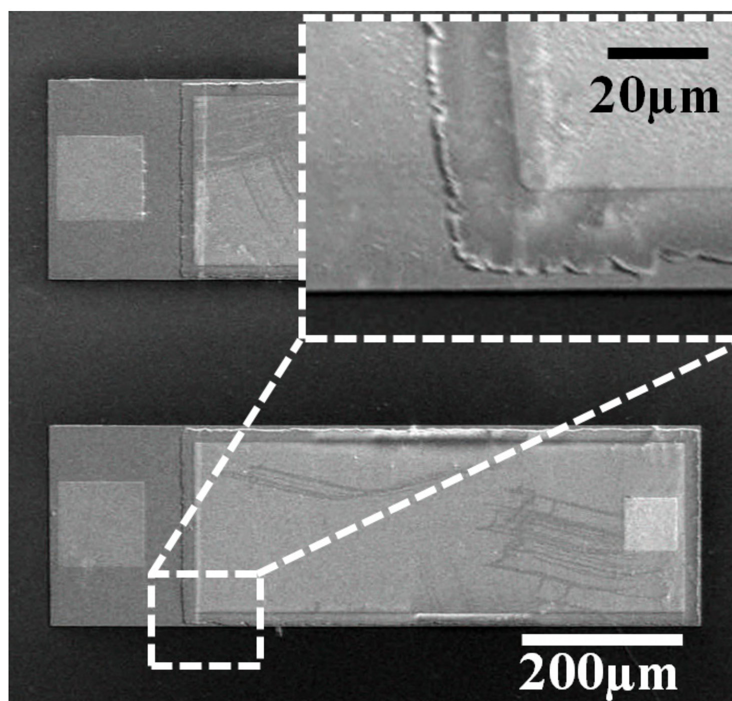

Figure 6.6 The secondary electron microscope (SEM) images of the fabricated pMUT. As the edge of the wet-etched PZT is zigzagged, the PZT thin film and bottom electrode is intentionally larger than top electrode to avoid the short circuit.

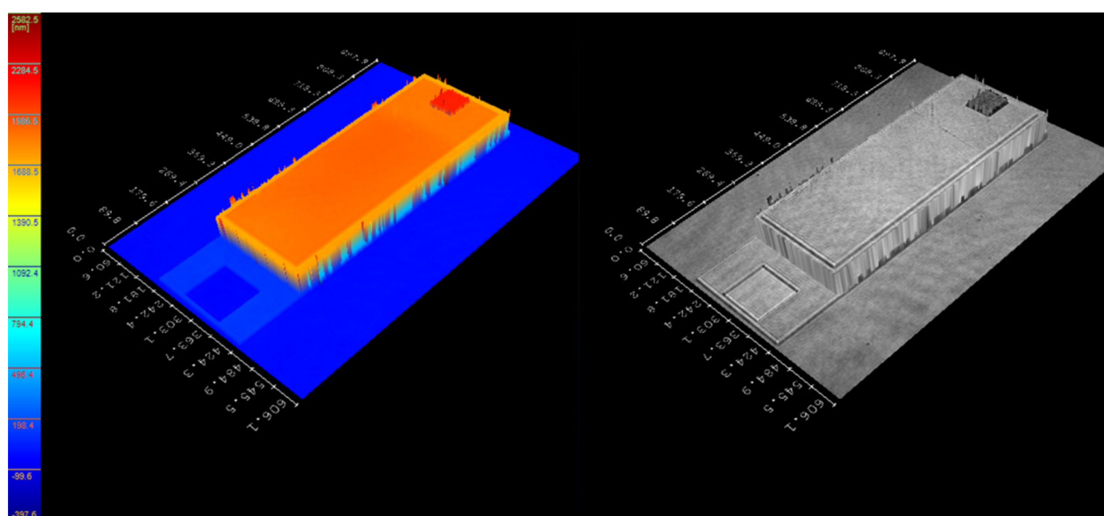

Figure 6.7 3-D image of the pMUT, captured by the digital holographic microscope. No obvious membrane buckling can be observed.

The pMUT is then characterized using the DHM-R2100 digital holographic

microscope from Lyncée Tec Ltd. Figure 6.7 shows the captured 3-D image of one pMUT element. The membrane looks relatively flat, because the top Pt/Ti electrode is compressively stressed which compensates the tensile stress of the PZT thin film. Details of the stress control are described in our previous study [178]. With the help of the relatively flat membrane, the buckling induced performance degradation can be alleviated [64]. The pMUT is then packaged and wire bonded in a dual in-line package (DIP) for testing, shown in the inset of Figure 6.4. It is electrically excited by the stroboscopic module of the holographic microscope with 1V AC voltage, and the 3-D images during motion are captured for analysis. The measured mode shapes are illustrated in Figure 6.8, and the displacement sensitivity with respect to frequency is plotted as well. This device reaches sensitivity of more than 807nm/V at its resonant frequency (482kHz), which is a considerably high performance. Table 6.1 summarizes several previously reported PZT based pMUTs. Benefited from the high d_{31} and low loss MPB-PZT thin film, as well as the design optimization, this proposed pMUT shows superior performance over the others. Even with much smaller membrane dimension, it shows significantly higher displacement sensitivity. Moreover, the driving voltage of previously reported pMUT has to be high enough (>10V) to achieve expected displacement. Such high voltage may result in the repolarization of PZT thin film, and hence those pMUTs employ large DC bias to avoid the repolarization and performance degradation. For the highly sensitive pMUT, however, the expected displacement can be achieved with rather small driving voltage. Considering the 7V coercive voltage of the MPB-PZT thin film, a 2-3V driving voltage can be quite safe for the device. Without the large DC and AC voltage, the pMUT consumes lower power and its lifetime is extended, which is suitable to be integrated to portable electronics.

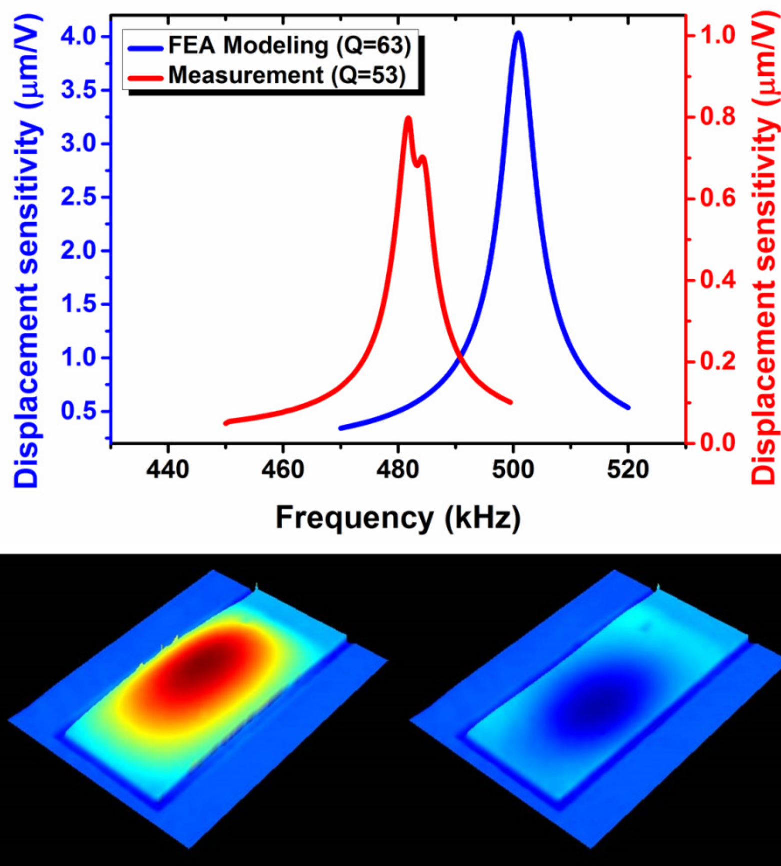

Figure 6.8 The measured displacement sensitivity of the pMUT without DC offset. A 807nm/V sensitivity is achieved at the resonant frequency (482kHz), which is considerbly high. The 3-D mode shape captured during vibration is shown as well.

Table 6.1 Comparison of displacement sensitivities of reported PZT based pMUTs

Device	Dimension (μm)	DC offset (V)	Resonant frequency (kHz)	Displacement sensitivity (nm/V)
Zhu *et al.* [179]	1500×1500	30	58	200
Wang *et al.* [174]	2000×2000	20	45	83
Muralt *et al.* [65]	1100 (Circ.)	5	49	420
This work	500×300	0	482	807

However, the measured displacement sensitivity is still lower than the prediction

by FEA modeling. This over estimation may be mainly attributed to two reasons. First of all, the FEA modeling uses the fixed boundary condition for the membrane edges. Such boundary condition simplifies the model and accelerates the calculation, but does not consider the anchor loss. In fact, the edge is not ideally fixed but slightly moves. Part of the vibration energy of membrane thus propagates into the Si substrate, resulting in lowered displacement sensitivity. The measured lower resonant frequency and lower Q-factor are also due to the non-considered anchor loss. Secondly, the displacement is very sensitive to the membrane stress. Although the membrane is relatively flat, the non-obvious buckling may still largely hamper the membrane vibration [81, 160]. In addition, the polling process adds extra tensile stress to PZT thin film [65], which makes the situation even worse. Other non-ideal effects during microfabrication may contribute to the sensitivity degradation as well.

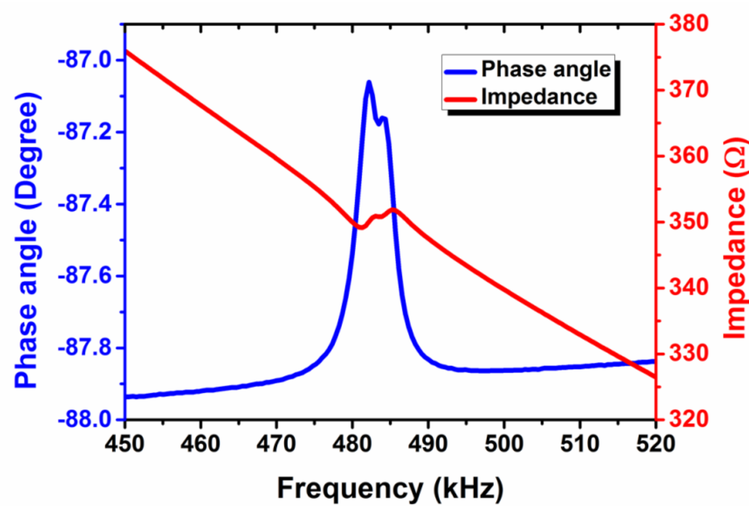

Figure 6.9 The impedance measurement results of the pMUT. The PZT based devices shows relatively low impedance, and standard 50Ω can be achieved by connecting 7 pMUTs in parallel for impedance match. The electromechanical coupling coefficient can be derived from the resonant and anti-resonant frequency as 1.62%.

Impedance characterization is then performed using the Agilent 4294A precision impedance analyzer, and the measurement results of single element are plotted in Figure 6.9. Compared to AlN based pMUT, where the impedance is usually several kΩ [168, 170], the PZT based pMUT shows a much lower impedance. If seven pMUT elements work together, standard 50Ω impedance can be achieved which well matches with circuits and coaxial cables. The electromechanical coupling coefficient k_{eff}^2 can be derived from resonant frequency f_r and anti-resonant frequency f_a through following relation [166]:

$$k_{eff}{}^2 = \frac{f_a^2 - f_r^2}{f_a^2} \tag{6.1}$$

This parameter directly reflects the electrical-mechanical energy conversion efficiency of the device. The in-air k_{eff}^2 is calculated as 1.62% and this value is higher than recently reported PZT pMUTs: 1.56% [168], 1.42% [174], 1.29% [180] and 1.12% [166].

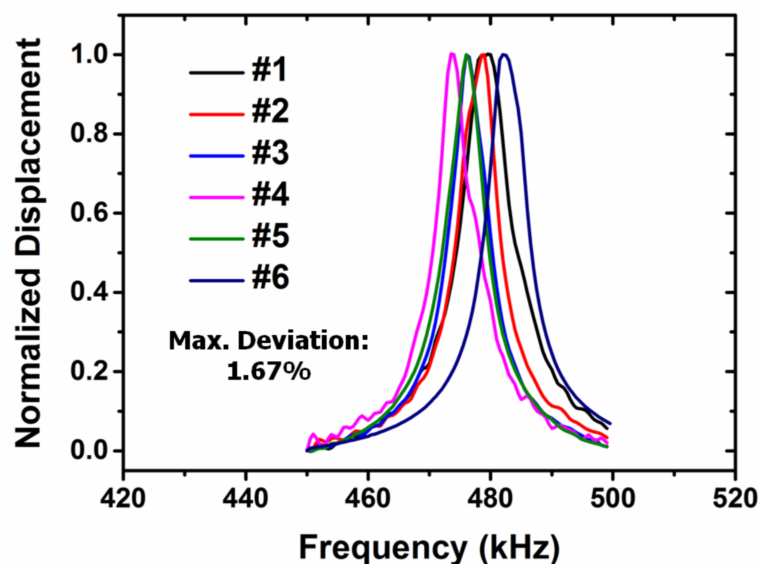

Figure 6.10 The uniformity testing results of the the pMUT array. This pMUT array

shows quite good uniformity, where the maximum frequency deviation is only 1.67%.

As pMUT array, several pMUT elements are simultaneously driven to enhance the transmitted ultrasound pressure. However, if the deviation of their resonant frequencies is too large, the driving frequency may fall into the resonances of only a few elements. As the consequence, the pMUT array cannot achieve its best performance. Thus, the uniformity of the elements is of interest as well. Six pMUT elements from the same die are tested using the digital holographic microscope. Their normalized frequency responses are illustrated in Figure 6.10. Because of the well-controlled fabrication processes, these elements show quite good uniformity. Their resonant frequencies are very close, with maximum deviation of only 0.84%.

6.2.2 In-Air transmitter testing

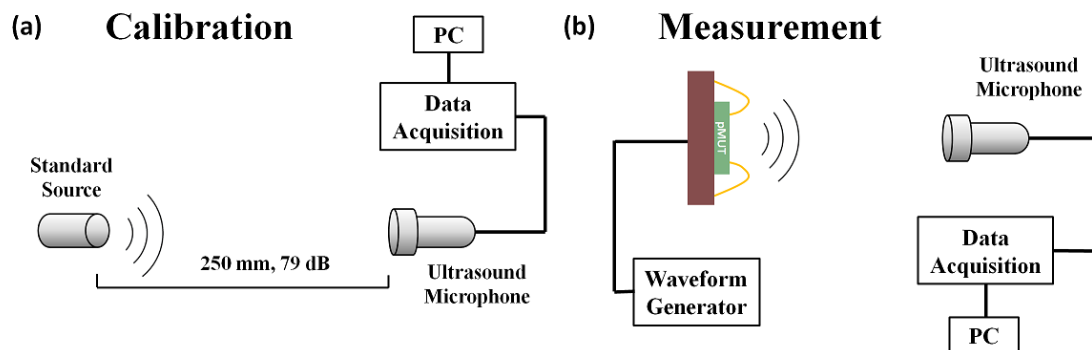

Figure 6.11 The setup for in-air transmitting testing: (a) A standard ultrasound source is used for calibration first, which is able to generate 79dB SPL at distance of 250mm and; (b) pMUT is driven by 2V sinusoidal signals, and the transmitted ultrasound is recorded by the ultrasound microphone.

This proposed pMUT, which is of high performance and high uniformity, shows its promise for practical applications in portable electronics. One of the potential

applications is the in-air gesture recognition for remote interaction with electronic devices, where the pMUT is used to transmit ultrasound waves. In order to evaluate the transmitting performance of the pMUT, the in-air testing is performed with setups shown in Figure 6.11. An ultrasound microphone (CM16/CMPA externally polarized condenser ultrasound microphone from Avisoft-Bioacoustics, together with the UltrasoundGate 116H data acquisition system) is employed to record the transmitted ultrasonic wave. Before the testing, this microphone is calibrated first. As is shown in Figure 6.11 (a), a standard source is fixed 250mm away from the microphone. It continuously generates ultrasound once switched on, and the SPL at distance of 250mm is 79dB (20μPa as reference sound pressure in air). The microphone records such ultrasound for 10s and takes it as the reference for the following testing. The standard source is then changed to the pMUT for measurement, as is shown in Figure 6.11 (b). A single pMUT element is driven by 2V sinusoidal signal at 482kHz without DC offset. Such low voltage prevents the unwanted PZT thin film repolarization and performance degradation. A 31mPa ultrasound pressure is measured at distance of 10mm, shown in Figure 6.12 (a). The SPL change with respect to distance is measured as well. As is shown in Figure 6.12 (b), the SPL decreases exponentially with distance, and 58.5dB SPL can still be detected at distance of 70mm. Since air is a highly damped medium, high frequency ultrasound may suffer significant attenuation. Although the 482kHz frequency of this pMUT may not be low enough in air, the lower frequency can be always achieved by increasing the membrane dimension. Development of such lower frequency pMUT will be our future works, and the sensitivity of the larger membrane will definitely be even higher. It is also worth noting that the SPL at 20mm and 30mm largely deviates. This is probably because of the standing wave between the pMUT and microphone, and the microphone located at

node or antinode experiences depressed or enhanced ultrasound pressure, respectively.

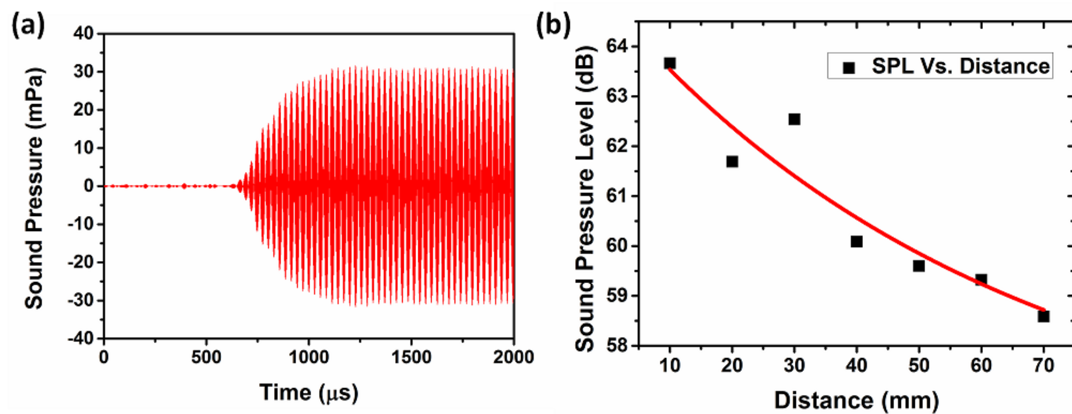

Figure 6.12 (a) The recorded ultrasound transmitted by a single pMUT element at a distance of 10mm and; (b) The SPL chagne with respect to the distance. The SPL drops exponentially, and the deviations at distance of 20mm and 30mm are probably due to the standing wave between the pMUT and the microphone.

6.3 Summary

In this chapter, a high performance PZT pMUT is designed and fabricated. Leveraging on the newly developed pulse poling process, the piezoelectric constant d_{31} of the MPB-PZT thin film can be as high as 105pm/V. Benefited from the high performance PZT thin film and the optimized pMUT design, the fabricated pMUT achieves a displacement sensitivity of 807nm/V at its resonant frequency (482kHz) with dimension of 500×300μm. Such considerably high sensitivity is achieved with no DC offset. A single pMUT element is able to generate 63.7 dB sound pressure level (SPL) at 10 mm in air with only 2V input. The low input voltage not only provides low power consumption, but also prevents the unwanted PZT repolarization and extends the pMUT lifetime. The proposed pMUT shows its promise for practical applications in portable electronics.

Chapter 7 pMUT with Ultra-wide Frequency Bandwidth

Ultrasound based diagnostic imaging is widely used for visualizing internal body structures, because it is efficient, low-cost and real-time, without any harmful ionizing radiation. The ultrasonic pulses are transmitted and received by ultrasonic transducer. For diagnostic imaging, its axial imaging resolution equals to half of spatial pulse length, and shorter pulse length results in better resolution [181]. Shorter pulse length can be achieved by increasing the operating frequency; however higher frequency leads to higher attenuation and the detecting range becomes very small. To ensure a reasonable detecting range, the highest frequency is usually below 10 MHz [182]. Another way to achieve shorter pulse length is increasing the frequency bandwidth of ultrasonic transducer. When an ultrasonic transducer is excited by a short electric pulse, it rings at the resonant frequency for a few oscillations, and the generated acoustic pulse cannot be ideally short, which is shown as Pulse A in Figure 7.1 (a). If Fourier Transform is applied to the pulse, a dispersion of frequency can be observed. The pulse actually contains a series of frequencies. Considering a Pulse B, which is shown in Figure 7.1 (b), the frequency is same to Pulse A but length is shorter. Its corresponding frequency bandwidth is observed to be even broader than that of Pulse A, which means the spread frequencies help to reduce the pulse length. Hence an ultrasonic transducer which has a larger frequency bandwidth can generate a pulse more like the Pulse B, *i.e.* a shorter pulse. Researcher from other group also claimed that the shorter pulse has wider bandwidth, and the pulse length is inversely

proportional to the frequency bandwidth [183]. Therefore, a broadband ultrasonic transducer can generate an acoustic pulse with very short length, which means the axial resolution can be further enhanced, or the detecting range can be deeper inside the body without compromising the imaging resolution. In addition, if the frequency bandwidth is wide enough, advanced harmonic sensing technology, which significantly improves the imaging contrast, can be realized by single transducer device [182]. In consequence, ultrasonic transducer with large frequency bandwidth is always preferred.

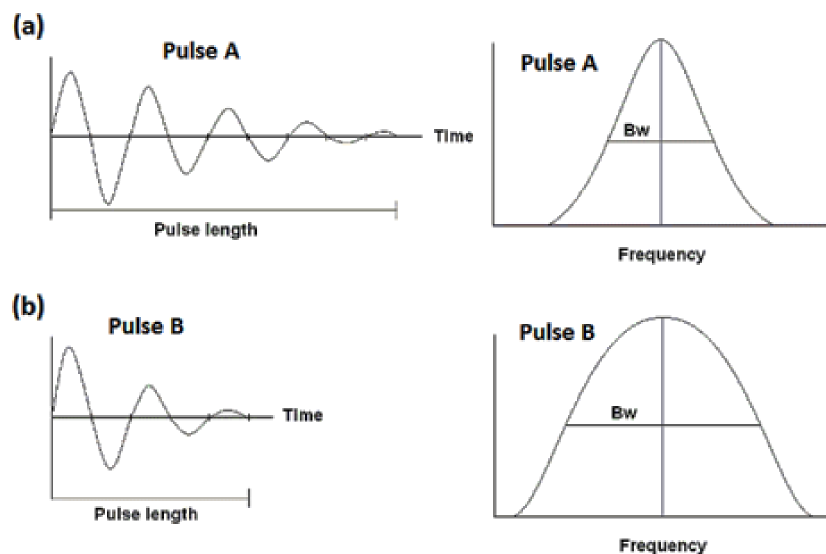

Figure 7.1 (a) Longer pulse (Pulse A) in time domain and frequency domain and; (b) Shorter pulse (Pulse B) in time domain and frequency domain.

7.1 Motivation

Conventional ultrasonic transducer made by bulk piezoelectric ceramics has been dominant for decades, but its limited bandwidth can hardly meet the requirement. The limited bandwidth is mainly due to the large acoustic impedance mismatch between

the transducer and soft tissue of human body. With the MEMS technology, the MUT is a promising alternative which aims to overcome the shortcomings of bulk piezoelectric ceramic based ultrasonic transducer. The flexural mode operation of MUT significantly reduces its mechanical impedance, minimizing the acoustic impedance mismatch between the transducer and working medium. This concept has been successfully realized using cMUT. A remarkably wide frequency bandwidth of over 100 % has been achieved without any matching layer [52]. However, the operating voltage of cMUT is extremely high, which is usually over 100V. Such high voltage creates safety concerns and limits cMUT's application to patients. As the alternative, pMUT is actuated using piezoelectric material, which operates at a much lower voltage [69, 151]. Similar to cMUT, pMUT works in flexural plate mode, therefore the acoustic impedance of pMUT is expected to be lowered as well. Unfortunately, performances of most of realized pMUTs are much poorer than expectation. Especially for the bandwidth, despite that analytical modeling implies that a bandwidth of over 100% is possible for pMUT [50], experimental results show that the bandwidth of pMUT is much smaller than this ideal value, and even worse than conventional bulk piezoelectric ceramic based ultrasonic transducer [184, 185]_ENREF_6. Such deviation is mainly attributed to the residual stress after high temperature processing. Although Muralt *et al.* successfully implements a pMUT with flat membrane by stresses compensation, the bandwidth is severely limited and authors strongly suggest pMUT should not be used for applications which require large bandwidth [65].

To overcome the bandwidth limitation of pMUT, Hajati *et al.* develop a pMUT array with elements of different sizes, and each of them has a distinct resonant peak [186]. When they work together in water, all the peaks are merged and form a wide

bandwidth. Although the bandwidth issue is addressed, the broadband effect is achieved with whole array. Wide bandwidth for single pixel is still not available, and ultrasonic image cannot be obtained without mechanically scanning. In this chapter, we propose a mode-merging pMUT device. A -6dB bandwidth of over 94% in water is achieved by single pMUT without matching layer. The associate pulse duration is only 1 μs at central frequency of 1.24 MHz, which is considerably shorter than previously reported pMUT devices.

7.2 Concept and Design

Figure 7.2 (a) shows the schematic illustration of the mode-merging pMUT containing a released rectangular plate. This pMUT contains a rectangular plate with large aspect ratio, of which the first few resonant frequencies are close to each other. When the pMUT operates in largely damped medium like water or soft tissue, the resonant peaks of different modes are merged together, forming a much wider bandwidth. Choi *et al.* developed 1-D and 2-D analytical models to describe the behavior of pMUT with rectangular plate, but such models only consider the fundamental mode [157, 187]. Since the proposed pMUT employs several resonant modes merged together, such analytical models may not be suitable. To determine the modal frequencies, the pMUT is modeled as a rectangular membrane (dimensions: L_x and L_y) with fully clamped boundaries. Such membrane is assumed to be composed by uniform material for simplification. The modal frequencies of the membrane are given by [188]:

$$f_{m,n} = \frac{1}{2} \times \sqrt{\frac{T}{\sigma}} \times \sqrt{\frac{m^2}{{L_x}^2} + \frac{n^2}{{L_y}^2}} \qquad m, n=1,2,3,\ldots \tag{7.1}$$

where T is the surface tension, and σ is the area density.

Considering k as the length / width aspect ratio ($k = L_x / L_y$ and $L_y = L$), Eq. (7.1) then can be rewritten as:

$$f_{m,n} = \frac{1}{2L} \times \sqrt{\frac{T}{\sigma}} \times \sqrt{(\frac{m^2}{k^2} + n^2)} \qquad m, n = 1,2,3,\ldots \qquad (7.2)$$

The fundamental frequency f_0 (m=1, n=1) thus is:

$$f_0 = \frac{1}{2L} \times \sqrt{\frac{T}{\sigma}} \times \sqrt{(\frac{1}{k^2} + 1)} \qquad (7.3)$$

and the modal frequencies become:

$$f_{m,n} = f_0 \times \sqrt{(\frac{m^2+k^2n^2}{k^2+1})} \qquad m, n = 1,2,3,\ldots \qquad (7.4)$$

If we consider the frequency of *a-th* vibration mode equals to $f_{1,2}$, then frequencies of first $a - 1$ modes are:

$$f_{m,1} = f_0 \times \sqrt{(\frac{m^2+k^2}{k^2+1})} \qquad m < a \qquad (7.5)$$

The relation between a and k is shown in Figure 7.2 (b). Once the aspect ratio k is greater than 3, which is usually true for a rectangular membrane, Eq. (7.5) is valid for the first 5 modes. Hence, the 1st to 5th modes are investigated in this work. Figure 7.2 (c) shows the modal frequency ratios with varying k, and the associated mode shapes are shown in Figure 7.2 (d). The frequency increasing speed is found to be dependent

on the parameter *k*. With higher *k*, the increasing speed becomes slower, *i.e.* higher mode frequencies are closer to fundamental frequency. The number of modes which fall into a certain frequency range is controlled by parameter *k*. Therefore, the length / width aspect ratio *k* is the key design parameter for the mode-merging pMUT.

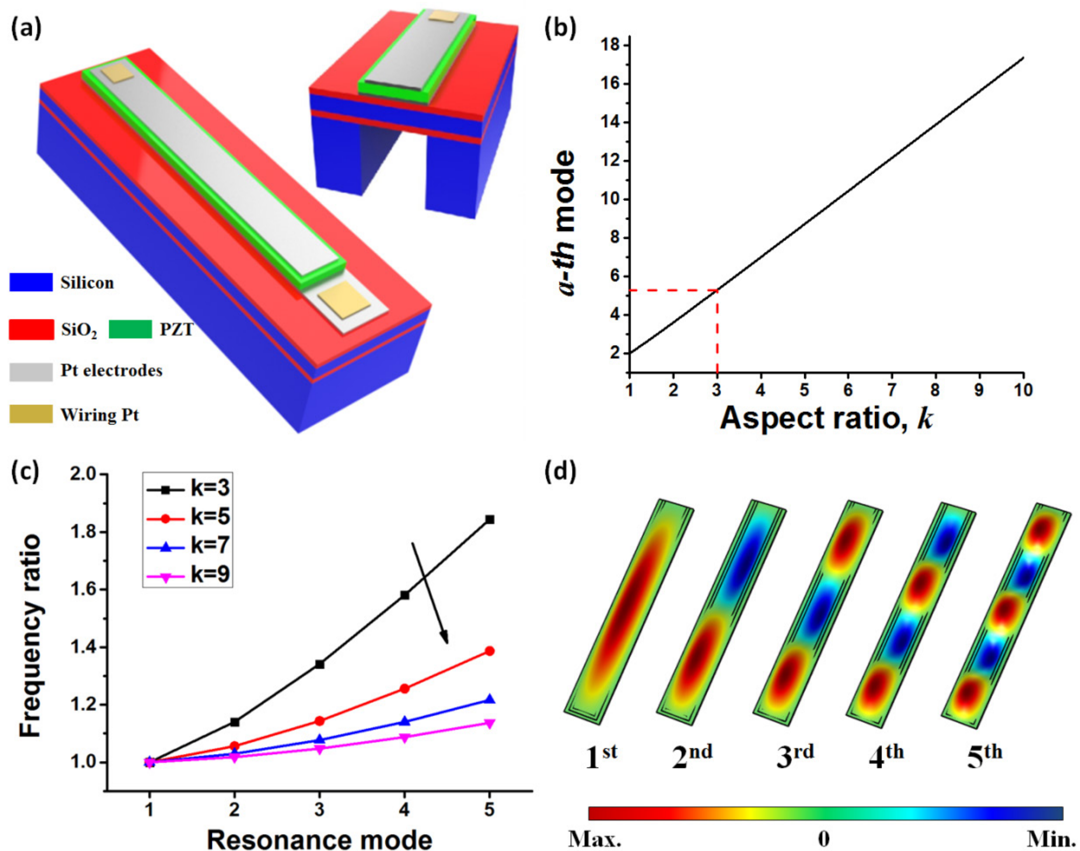

Figure 7.2 (a) The schematic drawing of proposed pMUT; (b) Relation between *a* and length / width aspect ratio *k*; (c) Derived modal frequency ratios with varying *k* and; (d) The associated mode shapes.

The dimension of the pMUT membrane thus is determined as 1550µm * 250µm, with a large length / width aspect ratio *k* of 6.2. Such high *k* ensures that the frequency ratios of first 5 modes are less than 1.3.

7.3 Device Characterization and Discussion

The OM and SEM images of the fabricated pMUT are shown in Figure 7.3. Because of the wet etching process, the edges of PZT thin film are not smooth, illustrated in Figure 7.3 (d).

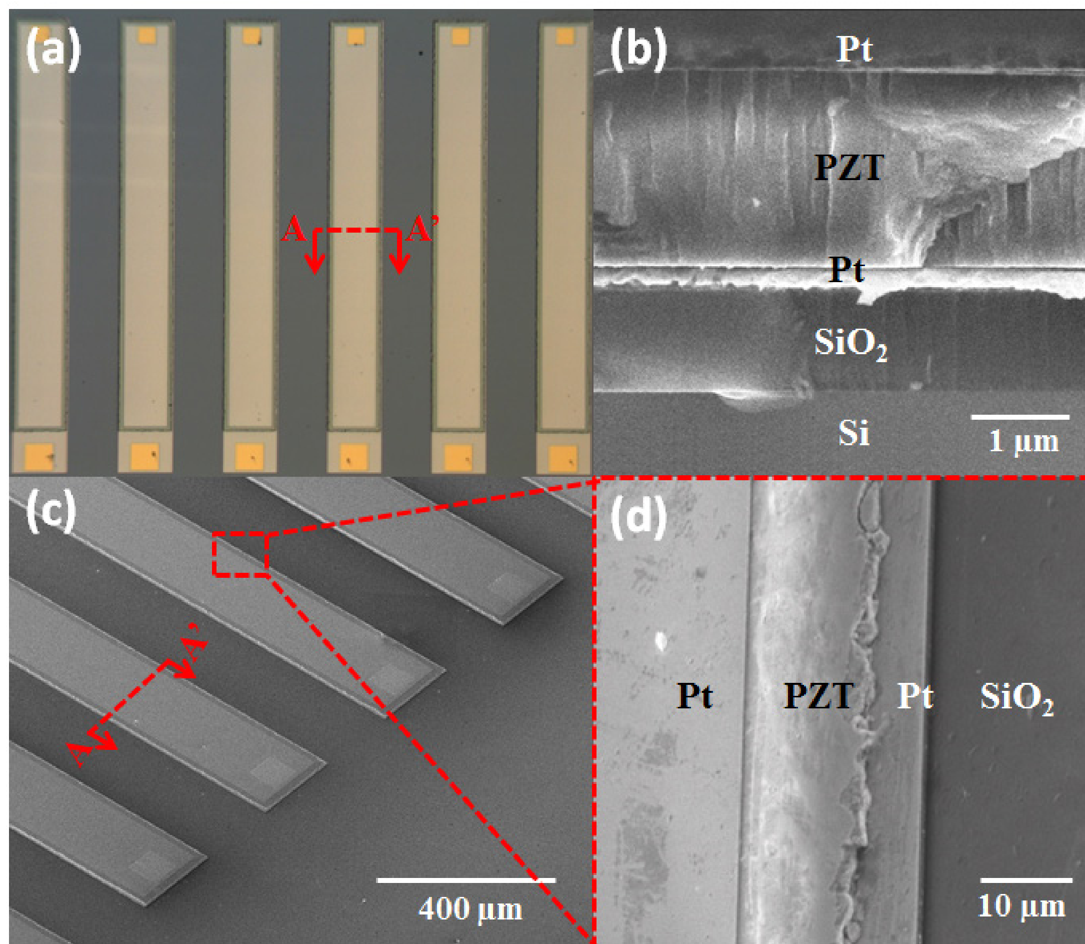

Figure 7.3 (a) OM image of fabricated pMUT; SEM image of (b) cross-sectional view of released multi-layer membrane; (c) pMUT array and; (d) edge of pMUT element.

7.3.1 Device characterization in air

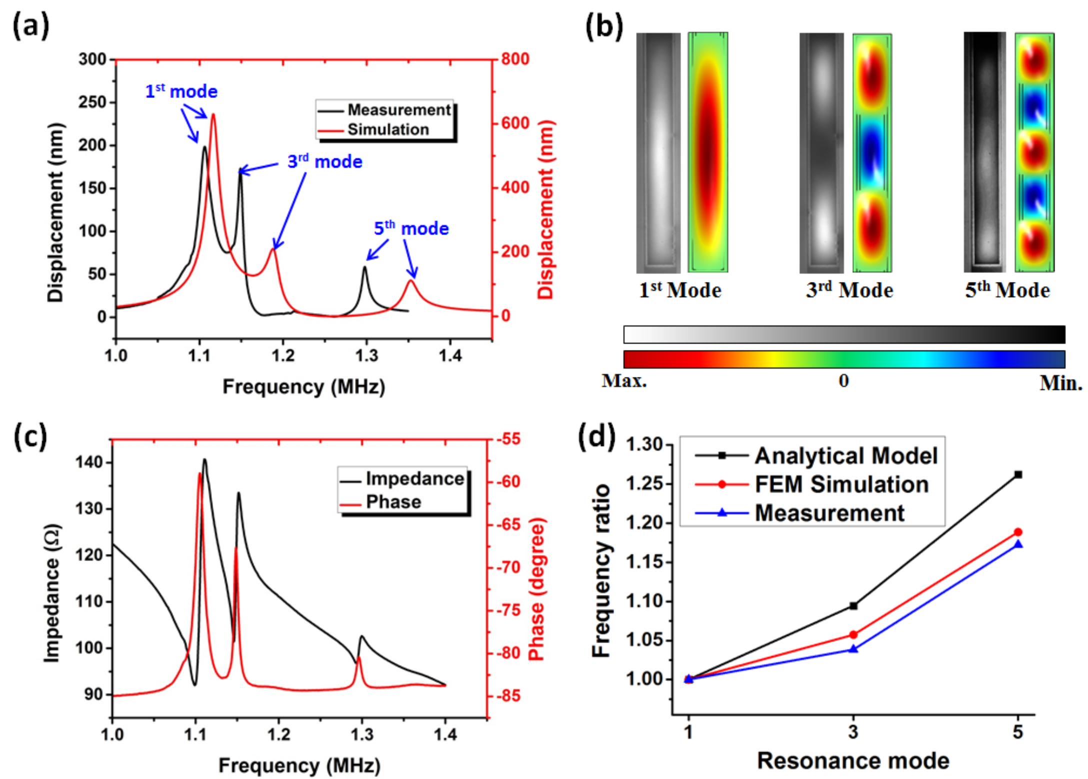

Figure 7.4 (a) Simulated and measured frequency response under 1 V_{pp} electrical excitation; (b) The mode shape for each resonant peak. Left ones are measured (multimedia view) and right ones are obtained by simulation; (c) Impedance measurement results and; (d) Comparison of analytical model, FEM simulation and measurement results.

A 3-D piezoelectric device FEM is created using COMSOL multi-physics software to study the behavior of this multilayer membrane. The frequency response of displacement amplitude under electrical excitation (1 V_{pp}) is shown in Figure 7.4 (a). As is aforementioned, the low-frequency ultrasound suffers lower attenuation and enables a larger imaging depth. Therefore the proposed pMUT has a relatively low fundamental frequency (~1.12 MHz). It is worth noting that the even modes are missing in the response spectrum. For an example of 2nd mode, the membrane can be divided into two regions. These two regions are symmetrical with opposite motions. However, the mechanical force from converse piezoelectric effect is unidirectional.

The unidirectional force can hardly be coupled to such opposite motion and excite the 2nd mode. Other even modes are also missing for the same reason; hence only odd modes are electrically excited. Figure 7.4 (b) shows the mode shape at each peak in response spectrum. Totally three modes are excited within a very narrow frequency range (~0.3 MHz), which is coherent with the analytical model. The 1st mode and 3rd mode have already merged without considering damping effects from environment. When this pMUT works in largely damped medium, all the three resonance modes, or even more modes, will be merged together, and hence the frequency bandwidth is significantly broadened.

The as-fabricated pMUT is firstly characterized using DHM-R2100 holographic MEMS analyzer by Lyncée Tec Ltd. The device under test (DUT) is electrically excited by the stroboscopic module with 1 V_{pp}. Dynamic 3-D vibrations of DUT are captured and recorded for analysis. Measured frequency response and mode shapes at resonant peaks are shown in Figure 7.4 (a) and (b), respectively. Similar to the simulation results, totally three modes are excited within a narrow frequency range of 0.3 MHz with 1st mode and 3rd mode overlapped. It is clearly shown that excited modes are all odd modes, which are consistent with the simulation results and above discussion. Compared with simulation results, the measured frequencies are slightly lower. This may be due to the non-perfect DRIE process during micro-fabrication. Since the side walls cannot be perfectly vertical to the back surface of membrane after DRIE process, therefore, a larger released membrane results in lower frequencies. Another deviation is that measured displacement amplitude of 1st mode is much smaller than that in simulation. Because the device is characterized in air, the 1st mode may suffer severe air damping. From the measured response spectrum, peak of 1st mode is observed to be broadened, implying its energy dissipation due to air damping

is higher than 3rd mode. Hence the displacement amplitude of 1st mode drops to almost the same as 3rd mode. The impedance characterization is performed as well using Agilent 4294A precision impedance analyzer as shown in Figure 7.4 (c). The electromechanical coupling coefficient ${k_{eff}}^2$ can be derived by resonant frequency f_r and anti-resonant frequency f_a through following relation [151]:

$$ {k_{eff}}^2 = \frac{f_a^2 - f_r^2}{f_r^2} \tag{7.6} $$

Calculated electromechanical coupling coefficients for 1st, 3rd and 5th mode are 1.97%, 1.04% and 0.99%, respectively.

Comparison of analytical model, FEM simulation and measurement are illustrated in Figure 7.4 (d). In general, both the analytical and FEM match the measured data well. Although the analytical model is simplified based on the assumption of a uniformly single layer membrane, the predicted frequencies are slightly higher and the errors are still within acceptable range (5.4% for 3rd mode and 7.6% for 5th mode). The analytical model thus provides a quick way to determine the length / width aspect ratio k for design of mode-merging pMUT. For the sophisticated FEM simulation, the results are very close to the experimental data, better than the analytical model. The slight deviation is probably due to some non-ideal factors, as it is discussed above.

7.3.2 Underwater testing

7.3.2.1 Testing setup

To characterize the underwater performance of the fabricated pMUT, a 1.0 mm

needle hydrophone along with 8 dB pre-amplifier by Precision Acoustics Ltd. is used to detect the transmitted acoustic pulse at a distance of 3 mm as shown in inset of Figure 7.5 (b). The pMUT is driven by a 20 V electrical pulse signal using an Agilent 33510B waveform generator. Duration of this pulse signal is 300 ns.

7.3.2.2 Testing results and discussion

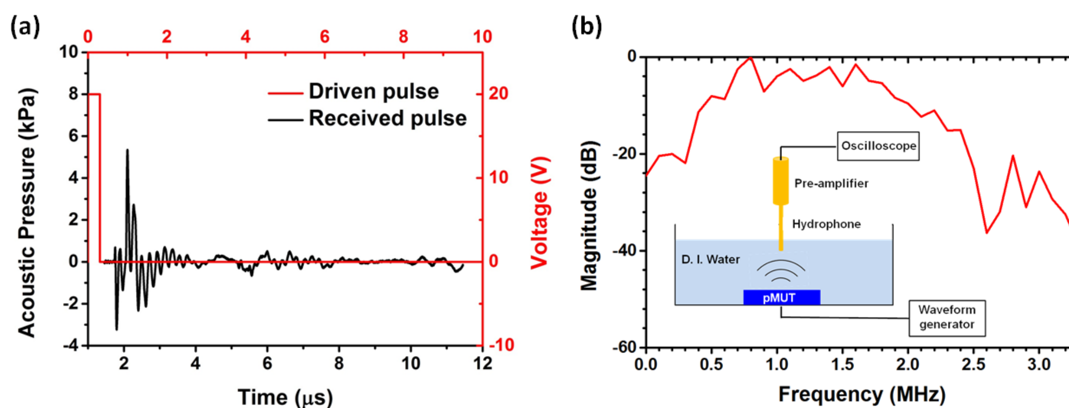

Figure 7.5 (a) Underwater performance testing results using hydrophone and; (b) The corresponding Fast Fourier Transform (FFT) spectrum. The testing set-up is shown in the inset.

Driven pulse and received pulse are shown in Figure 7.5 (a), while the corresponding Fast Fourier Transform (FFT) spectrum is shown in Figure 7.5 (b). The -6 dB frequency bandwidth is measured as 95% with central frequency of 1.24 MHz, which is significantly higher than reported data of 10% [185], 43% [166], and 57% [184]. Benefited from such ultra-wide frequency bandwidth, the mode-merging pMUT is able to generate very short ultrasonic pulse (1 μs) at relatively low frequency. The pMUT with similar pulse duration (~0.7 μs) operates at much higher frequency of 7.1 MHz [184]. For the pMUT with similar operating frequency (~1.8MHz), its pulse duration is as long as 3 μs [185]. Therefore, the ultra-wide frequency bandwidth pMUT is superior to normal pMUTs.

7.4 Summary

In this chapter, a mode-merging pMUT is designed, fabricated and characterized. Totally, three modes are excited within a narrow frequency range of 0.3 MHz. When this pMUT is working in a highly damped medium, excited modes are merged together and form an ultra-wide frequency bandwidth. The -6 dB bandwidth in water is measured as 95 %, which is significantly higher than previously reported pMUTs. Benefited from such ultra-wide frequency bandwidth, 1 μs ultrasonic pulse is achieved at central frequency of 1.24 MHz. Diagnostic imaging with better axial resolution and larger imaging depth may be realized with this ultra-wide frequency bandwidth pMUT.

Chapter 8 Conclusions and Future Works

8.1 Summary of Current Works

A variety of piezoelectric ultrasonic MEMS devices are presented in this thesis, including novel acoustic wave sensors and pMUTs with different unique features. The main focus of this work is to overcome the inherent limitations of currently reported piezoelectric ultrasonic MEMS sensors.

1. SAW based pressure sensor as one of the basic piezoelectric MEMS sensors is firstly studied. It is found that the diaphragm shape can largely influence the sensitivity, and may even change the sign of PCF. This is due to the change of longitudinal / lateral strain ratio. Based on the findings, several approaches are proposed to further enhance the sensitivity.

2. Acoustic wave sensor can also be used for liquid sensing. Currently reported sensor responds to the product of liquid viscosity and density. By inducing two unique Lamb wave modes, the proposed novel sensor can be solely sensitive to either viscosity or density. Decoupled viscosity and density sensing by single device is realized for the first time.

3. Besides the sensor with ultrasonic wave propagating within the device, pMUTs with the capability of transmitting and sensing ultrasonic waves in the outer medium are developed as well. Due to the residual stress and initial deflection after fabrication process, the transmitting sensitivity of currently reported pMUTs becomes quite limited. Leveraging on the top electrode configuration and integrated vacuum cavity, a novel pMUT with zero initial deflection is developed. The transmitting sensitivity is

several times over the conventional design. In order to further increase the ultrasound transmitting efficiency, a pMUT with piston-like membrane motion is also developed. Unlike the Gaussian-like membrane deflection during vibration, the piston-like deflection can push more ultrasound medium back and forth, generating an even higher ultrasonic pressure.

4. The performance of AlN based pMUT may still be not satisfactory for practical applications, and therefore a PZT based pMUT is developed in this work. The newly developed unipolar pulse poling process enables a PZT thin film with much higher piezoelectric constant and lower dielectric constant than conventional film. Together with optimized pMUT design, a high performance pMUT is finally achieved, showing a significantly high transmitting sensitivity.

5. Except for the sensitivity, the frequency bandwidth is also important for pMUT. Especially for diagnostic ultrasonic imaging application, the bandwidth determines the axial image resolution. With a large length / width ratio membrane, a broadband pMUT is developed. Several resonant modes are excited simultaneously, and the resonant peaks are overlapped with each other, forming an ultra-wide frequency bandwidth. The bandwidth is considerably higher than previously reported pMUTs.

8.2 Future Development of Electrically Switchable pMUT

8.2.1 Motivation

The quality of the diagnostic ultrasonic imaging, or the resolution, is mainly determined by the working frequency. Higher frequency gives shorter wavelength, and therefore better resolution [181]. However, the ultrasound attenuation also increases with frequency. Too high frequency means the ultrasound energy dissipates

very fast. The transmitted ultrasound pulse cannot penetrate to body deeply, resulting in very limited detecting range. Users therefore choose different frequencies between resolution and penetration for different situations. For example, higher frequency is used for superficial imaging and lower frequency for deep organ imaging [189]. Conventionally the pMUT, however, is designed at one dedicated frequency [170, 171], which usually works at its fundamental resonant mode. Although it shows weak resonances at higher modes, the electromechanical coupling is quite limited, *i.e.* the sensitivity is very low. Use of the higher modes thus is not practical. The user therefore has to physically change the transducer to meet the frequency requirements. In addition, for some applications like intravascular ultrasonic imaging (IVUS), changing of the transducer inside the vessel is not even possible. To overcome this limit, an electrically frequency switchable pMUT is proposed. With the innovative top electrode configuration, the proposed switchable pMUT is able to work at its 1st, 3rd and 5th mode efficiently, by activating different sets of top electrodes. As the consequence, this pMUT can electrically switch its working frequency (where the pMUT shows highest sensitivity) between 2.01 MHz, 3.19 MHz, and 5.84 MHz, without sacrificing the performance. This switchable pMUT would provide user with extra flexibility.

8.2.2 Concept and design

The proposed switchable pMUT (one element) is illustrated in Figure 8.1 (a). The element contains a rectangular flexural membrane with dimension of 400μm × 170μm. Usually one top electrode is adopted for conventional pMUT, and the induced piezoelectric stress couples with the fundamental mode vibration efficiently. However, if the pMUT works at its higher mode, the coupling efficiency significantly drops,

because the piezoelectric stress no longer matches with the mode shape but works against part of the membrane motion. The sensitivity at higher mode becomes poorer, and hence the use of higher modes for conventional pMUT is not practical.

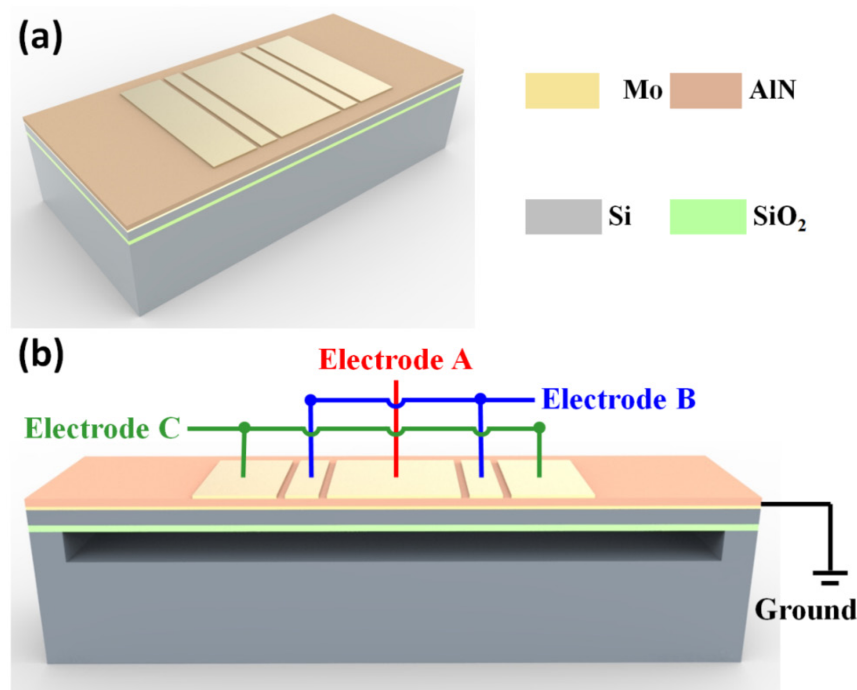

Figure 8.1 (a) 3-D schematic illustration of the switchable pMUT, which has five individual top electrodes and; (b) The electrical connections of the top electrodes. The top electrodes are divided into three sets, denoted as Electrode A, B and C.

To realize the electrically switching feature, this pMUT has five individual top electrodes. Such electrodes are divided into three sets, shown in Figure 8.1 (b). An FEM is built using COMSOL Multiphysics to determine the proper location and width of each electrode. Combination of different sets of electrodes enables the electrodes match with the mode shapes, *i.e.* Electrode A+B+C for 1st mode, Electrode A+B for 3rd mode, and Electrode B+C for 5th mode. Thus, by activating different sets of electrodes, the switchable pMUT can always achieve its best electromechanical coupling efficiencies at each resonant mode. As the results, the working frequency can

be electrically switched, without physically changing the pMUT.

The fundamental resonant frequency of a rectangular membrane is determined by the geometry as [188]:

$$f_0 = \frac{1}{2} \times \sqrt{\frac{T}{\sigma}} \times \sqrt{\frac{1}{L^2} + \frac{1}{W^2}} \tag{8.1}$$

where T is the surface tension, σ is the area density, L is the membrane length, and W is the membrane width. Meanwhile, the membrane aspect ratio $k=L/W$ determines the positions of higher resonant modes with respect to fundamental mode as [172]:

$$f_n = f_0 \times \sqrt{\left(\frac{n^2+k^2}{k^2+1}\right)} \qquad n=1, 2, 3\ldots \tag{8.2}$$

The frequency distance between each mode thus can be engineered by the factor k, and a lower k gives rise to larger frequency switching range. With the given materials and geometry, the frequencies of the switchable pMUT are predicted by FEA modeling as 2.28MHz, 3.59MHz and 6.40MHz for 1st, 3rd and 5th mode, respectively.

8.2.3 Preliminary characterization and discussion

The as-fabricated switchable pMUT array is shown in Figure 8.2 (a). All the elements are connected in parallel, and the bonding pad for each electrode set is denoted in the figure as well. Figure 8.2 (b) shows a single pMUT element. The minimum feature size of the top electrodes is 1μm to reduce the non-ideal effect of the synthesized effective electrodes. The multilayer interconnections and the vias are shown in Figure 8.2 (c).

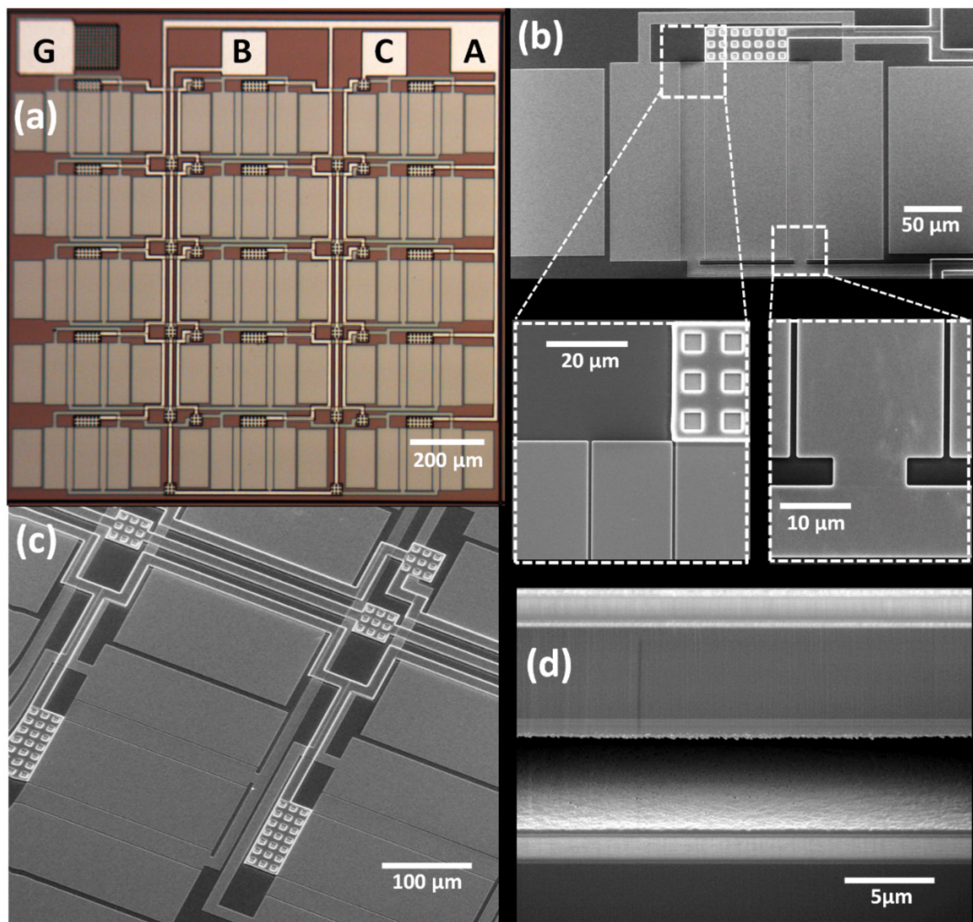

Figure 8.2 The as-fabricated switchable pMUT: (a) OM image of the pMUT array; (b) SEM image of a single pMUT element. The minimum feature size is 1µm; (c) The multilayer metal structures and vias and: (d) cross-sectional view of the device.

The switchable pMUT is characterized using the DHM-2100R digital holographic microscope from Lyncée Tech, with 1V excitation. The phase images of the device during motion are captured, where the lighter color stands for higher surface height while darker color for lower height. Figure 8.3 shows the activated electrode sets, together with the corresponding phase images at resonance. The activated electrode sets are highlighted by orange color. It is worth noting that two dummy electrodes are also fabricated besides the electrode sets. The dummy electrodes are employed to reduce the initial membrane buckling, leveraging on their tensile residual stresses [64]. Largely deflected membrane could hamper the membrane vibration and give rise to

performance degradation. With the dummy electrode design, the pMUT performance degradation therefore can be minimized.

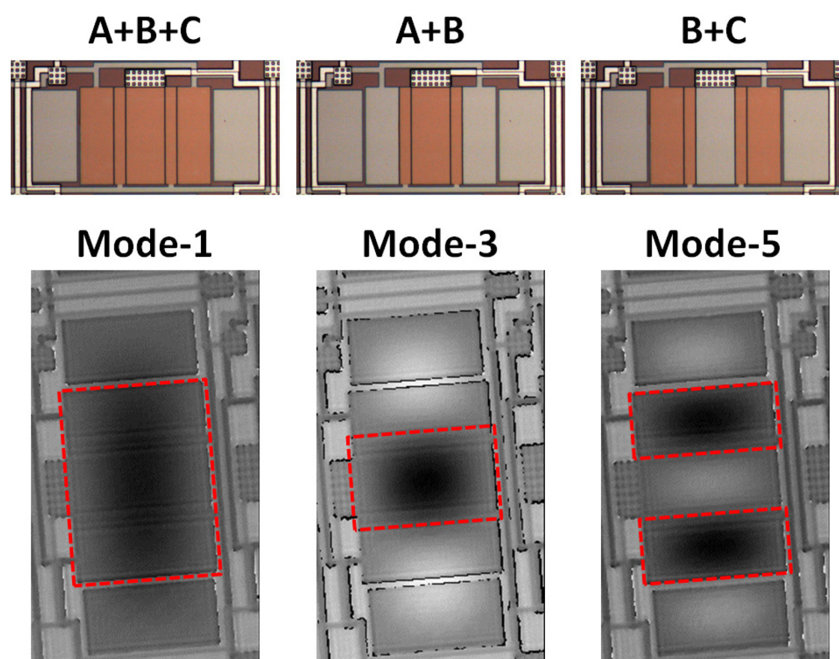

Figure 8.3 The activated electrode sets and the corresponding phase image for each resonance mode. By activating different sets of top electrodes, the synthesized effective electrode matches the in-phase motion parts of the membrane to achieve efficient coupling.

For the Mode-1 (fundamental mode), Electrode A, B and C are simultaneously activated, which work as one large effective electrode. The mode shape can be seen from the phase images, where the dash lines indicate the effective electrode in the phase image. It is clearly shown that the effective electrode matches well with the mode shape. The induced piezoelectric stress thus can couple with the vibration with maximum efficiency. For Mode-3, only Electrode A and B are activated. As can be seen from the figure, the effective electrode only covers the central part of the membrane, where the motion phase is 180° different with the rest part of membrane. Therefore, the effective electrode induced piezoelectric stress efficiently couples with

the in-phase motion part, and does not work against the rest of the membrane. In terms of Mode-5, Electrode B and C are activated. Since two parts of the membrane have the same motion phase, the effective electrode is divided to two parts to match them. Vibration at Mode-5 thus is enhanced.

A reference pMUT with the same membrane design but fully covered single top electrode is fabricated for performance comparison. Both the reference and switchable pMUTs are excited with 1V sinusoidal signal. Their frequency responses of displacement sensitivity in air are plotted in Figure 8.4. The resonant frequencies of the switchable pMUT are measured as 2.01 MHz, 3.19 MHz and 5.84 MHz for the three resonance modes. Compared to the FEA modeling results, these frequencies are slightly lower. This could be due to the anchor loss at the edges of membrane, which is not taken into account for FEA modeling.

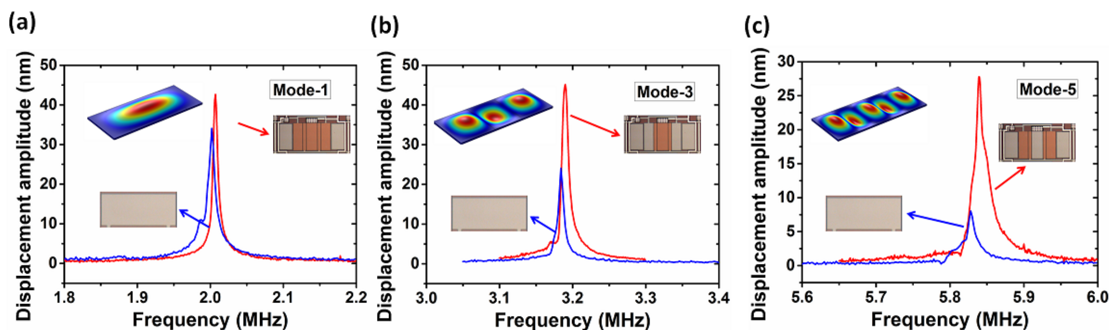

Figure 8.4 Performance comparison of reference pMUT and switchable pMUT: measured frequency response of displacement amplitude with 1V input voltage at each mode. The simulated mode shapes by FEA modeling are also shown as insets.

The sensitivity of the reference pMUT at Mode-1 is 34nm/V, which is denoted as S_{ref}. If this reference pMUT works at its higher mode, the sensitivity drastically drops to 70% S_{ref} and 23% S_{ref} at Mode-3 and Mode-5, respectively. Such low sensitivity, *e.g.* 8nm/V at Mode-5, can nearly be usable for practical applications. Meanwhile, for

the switchable pMUT, it shows higher sensitivities: 125% S_{ref} and 132% S_{ref} for Mode-1 and Mode-3, respectively. The sensitivity at Mode-3 does not decrease and is even higher than the S_{ref}, showing the high coupling efficiency. The performance at Mode-5 is 28nm/V, which is slightly lowered to 82% S_{ref}, but is still 3.5 times higher than the value of reference pMUT. This sensitivity is considered satisfactory for practical use.

Thus, the switchable pMUT has achieved considerably high sensitivities at three different frequencies, ranging from 2.01 MHz to 5.84MHz. In the future research, the switchable pMUT will be further characterized and tested under water to validate its frequency switchable function. The receiving sensitivity will be characterized as well, so as to make sure it functions well as both transmitter and receiver at different frequencies. With the switchable pMUT, the user would be able to electrically switch the working frequency for different situations, without physically changing the transducer or sacrificing the pMUT performance. This switchable pMUT shows its promise in the future dual-frequency ultrasonic imaging technology.

Bibliography

[1] G. A. Slack and T. McNelly, "Growth of high purity AlN crystals," *Journal of Crystal Growth,* vol. 34, pp. 263-279, 1976.

[2] W. Mueller, "A Brief Overview of FBAR technology," *Agilent White Paper,* 2001.

[3] R. Jakkaraju, G. Henn, C. Shearer, A. Harris, N. Rimmer, and P. Rich, "Integrated approach to electrode and AlN depositions for bulk acoustic wave (BAW) devices," *Microelectronic Engineering,* vol. 70, pp. 566-570, Nov 2003.

[4] T. Nishihara, T. Yokoyama, T. Miyashita, and Y. Satoh, "High performance and miniature thin film bulk acoustic wave filters for 5 GHz," in *Ultrasonics Symposium, 2002. Proceedings. 2002 IEEE*, 2002, pp. 969-972.

[5] O. Elmazria, M. El Hakiki, V. Mortet, B. M. Assouar, M. Nesladek, M. Vanecek*, et al.*, "Effect of diamond nucleation process on propagation losses of AlN/diamond SAW filter," *IEEE Trans Ultrason Ferroelectr Freq Control,* vol. 51, pp. 1704-9, Dec 2004.

[6] E. Iborra, M. Clement, J. Sangrador, A. Sanz-Hervas, L. Vergara, and M. Aguilar, "Effect of particle bombardment on the orientation and the residual stress of sputtered AlN films for SAW devices," *IEEE Trans Ultrason Ferroelectr Freq Control,* vol. 51, pp. 352-8, Mar 2004.

[7] N. Ledermann, P. Muralt, J. Baborowski, S. Gentil, K. Mukati, M. Cantoni*, et al.*, "{1 0 0}-Textured, piezoelectric Pb(Zrx, Ti1−x)O3 thin films for MEMS: integration, deposition and properties," *Sensors and Actuators A: Physical,* vol. 105, pp. 162-170, 7/15/ 2003.

[8] K. H. Koh and C. Lee, "A Two-Dimensional MEMS Scanning Mirror Using Hybrid Actuation Mechanisms With Low Operation Voltage," *Journal of Microelectromechanical Systems,* vol. 21, pp. 1124-1135, Oct 2012.

[9] K. H. Koh, B. W. Soon, J. M. Tsai, A. J. Danner, and C. Lee, "Study of hybrid driven micromirrors for 3-D variable optical attenuator applications," *Opt Express,* vol. 20, pp. 21598-611, Sep 10 2012.

[10] K. H. Koh, T. Kobayashi, and C. Lee, "Investigation of piezoelectric driven MEMS mirrors based on single and double S-shaped PZT actuator for 2-D scanning applications," *Sensors and Actuators a-Physical,* vol. 184, pp. 149-159, Sep 2012.

[11] K. H. Koh, T. Kobayashi, and C. Lee, "A 2-D MEMS scanning mirror based on dynamic mixed mode excitation of a piezoelectric PZT thin film S-shaped

actuator," *Opt Express,* vol. 19, pp. 13812-24, Jul 18 2011.

[12] K. H. Koh, T. Kobayashi, J. Xie, A. B. Yu, and C. K. Lee, "Novel piezoelectric actuation mechanism for a gimbal-less mirror in 2D raster scanning applications," *Journal of Micromechanics and Microengineering,* vol. 21, p. 075001, Jul 2011.

[13] K. H. Koh, T. Kobayashi, F. L. Hsiao, and C. Lee, "Characterization of piezoelectric PZT beam actuators for driving 2D scanning micromirrors," *Sensors and Actuators a-Physical,* vol. 162, pp. 336-347, Aug 2010.

[14] C. Lee, F. L. Hsiao, T. Kobayashi, K. H. Koh, P. V. Ramana, W. F. Xiang*, et al.*, "A 1-V Operated MEMS Variable Optical Attenuator Using Piezoelectric PZT Thin-Film Actuators," *IEEE Journal of Selected Topics in Quantum Electronics,* vol. 15, pp. 1529-1536, Sep-Oct 2009.

[15] K. H. Koh, C. Lee, and T. Kobayashi, "A Piezoelectric-Driven Three-Dimensional MEMS VOA Using Attenuation Mechanism With Combination of Rotational and Translational Effects," *Journal of Microelectromechanical Systems,* vol. 19, pp. 1370-1379, Dec 2010.

[16] K. H. Koh, T. Kobayashi, and C. Lee, "Low-Voltage Driven MEMS VOA Using Torsional Attenuation Mechanism Based on Piezoelectric Beam Actuators," *IEEE Photonics Technology Letters,* vol. 22, pp. 1355-1357, Sep 15 2010.

[17] M. Kohli, C. Wuethrich, K. Brooks, B. Willing, M. Forster, P. Muralt*, et al.*, "Pyroelectric thin-film sensor array," *Sensors and Actuators a-Physical,* vol. 60, pp. 147-153, May 1997.

[18] H. C. Liu, S. S. Zhang, T. Kobayashi, T. Chen, and C. Lee, "Flow sensing and energy harvesting characteristics of a wind-driven piezoelectric Pb(Zr0.52, Ti0.48)O-3 microcantilever," *Micro & Nano Letters,* vol. 9, pp. 286-289, Apr 2014.

[19] H. C. Liu, C. Lee, T. Kobayashi, C. J. Tay, and C. G. Quan, "Piezoelectric MEMS-based wideband energy harvesting systems using a frequency-up-conversion cantilever stopper," *Sensors and Actuators a-Physical,* vol. 186, pp. 242-248, Oct 2012.

[20] H. C. Liu, S. S. Zhang, R. Kathiresan, T. Kobayashi, and C. Lee, "Development of piezoelectric microcantilever flow sensor with wind-driven energy harvesting capability," *Applied Physics Letters,* vol. 100, p. 223905, May 28 2012.

[21] H. C. Liu, C. Lee, T. Kobayashi, C. J. Tay, and C. G. Quan, "A new S-shaped MEMS PZT cantilever for energy harvesting from low frequency vibrations below 30 Hz," *Microsystem Technologies-Micro-and Nanosystems-Information Storage and Processing Systems,* vol. 18, pp. 497-506, Apr 2012.

[22] H. C. Liu, C. K. Lee, T. Kobayashi, C. J. Tay, and C. G. Quan, "Investigation of a MEMS piezoelectric energy harvester system with a frequency-widened-bandwidth mechanism introduced by mechanical stoppers," *Smart Materials and Structures,* vol. 21, p. 035005, Mar 2012.

[23] H. C. Liu, C. J. Tay, C. Quan, T. Kobayashi, and C. Lee, "A scrape-through piezoelectric MEMS energy harvester with frequency broadband and up-conversion behaviors," *Microsystem Technologies-Micro-and Nanosystems-Information Storage and Processing Systems,* vol. 17, pp. 1747-1754, Dec 2011.

[24] H. C. Liu, C. J. Tay, C. G. Quan, T. Kobayashi, and C. Lee, "Piezoelectric MEMS Energy Harvester for Low-Frequency Vibrations With Wideband Operation Range and Steadily Increased Output Power," *Journal of Microelectromechanical Systems,* vol. 20, pp. 1131-1142, Oct 2011.

[25] W. G. Zhu, Z. H. Wang, C. L. Zhao, O. K. Tan, and H. H. Hng, "Low temperature processing of nanocrystalline lead zirconate titanate (PZT) thick films and ceramics by a modified sol-gel route," *Japanese Journal of Applied Physics Part 1-Regular Papers Short Notes & Review Papers,* vol. 41, pp. 6969-6975, Nov 2002.

[26] T. Grudkowski, J. Black, T. Reeder, D. Cullen, and R. Wagner, "Fundamental‐mode VHF/UHF minature acoustic resonators and filters on silicon," *Applied Physics Letters,* vol. 37, pp. 993-995, 1980.

[27] J. Wang, G. Kline, A. Landin, Y. Chen, and J. Hunt, "Thin film resonators and filters," in *1982 Ultrasonics Symposium*, 1982, pp. 466-475.

[28] D. L. DeVoe and A. P. Pisano, "Surface micromachined piezoelectric accelerometers (PiXLs)," *Journal of Microelectromechanical Systems,* vol. 10, pp. 180-186, Jun 2001.

[29] H. Jin, J. Zhou, X. He, W. Wang, H. Guo, S. Dong*, et al.*, "Flexible surface acoustic wave resonators built on disposable plastic film for electronics and lab-on-a-chip applications," *Scitific Report,* vol. 3, p. 2140, 2013.

[30] J. Zhou, X. L. He, H. Jin, W. B. Wang, B. Feng, S. R. Dong*, et al.*, "Crystalline structure effect on the performance of flexible ZnO/polyimide surface acoustic wave devices," *Journal of Applied Physics,* vol. 114, p. 044502, Jul 28 2013.

[31] X. L. He, D. J. Li, J. Zhou, W. B. Wang, W. P. Xuan, S. R. Dong*, et al.*, "High sensitivity humidity sensors using flexible surface acoustic wave devices made on nanocrystalline ZnO/polyimide substrates," *Journal of Materials Chemistry C,* vol. 1, pp. 6210-6215, 2013.

[32] Y. Q. Fu, L. Garcia-Gancedo, H. F. Pang, S. Porro, Y. W. Gu, J. K. Luo*, et al.*, "Microfluidics based on ZnO/nanocrystalline diamond surface acoustic wave devices," *Biomicrofluidics,* vol. 6, pp. 24105-2410511, Jun 2012.

[33] J. K. Luo, Y. Fu, G. Ashley, and W. I. Milne, "Integrated ZnO film based

acoustic wave microfluidics and biosensors," in *Advances in Science and Technology*, 2011, pp. 49-58.

[34] Y. Q. Fu, J. K. Luo, X. Y. Du, A. J. Flewitt, Y. Li, G. H. Markx*, et al.*, "Recent developments on ZnO films for acoustic wave based bio-sensing and microfluidic applications: a review," *Sensors and Actuators B-Chemical,* vol. 143, pp. 606-619, Jan 7 2010.

[35] X. Mu, C. Sun, H. Ji, L. Siow, Q. Zhang, Y. Zhu*, et al.*, "A high efficiency frequency pre-defined flow-driven energy harvester dominated by on-chip modified Helmholtz Resonating cavity," in *Electron Devices Meeting (IEDM), 2014 IEEE International*, 2014, pp. 8.4. 1-8.4. 4.

[36] S. A. Goss, R. L. Johnston, and F. Dunn, "Comprehensive compilation of empirical ultrasonic properties of mammalian tissues," *J Acoust Soc Am,* vol. 64, pp. 423-57, Aug 1978.

[37] A. Goldstein and R. L. Powis, "Medical ultrasonic diagnostics," *Ultrasonic Instruments and Devices I,* vol. 23, pp. 43-191, 1999.

[38] I. Ladabaum, X. Jin, H. T. Soh, A. Atalar, and B. T. Khuri-Yakub, "Surface micromachined capacitive ultrasonic transducers," *IEEE Trans Ultrason Ferroelectr Freq Control,* vol. 45, pp. 678-90, 1998.

[39] J. D. Bronzino, *Biomedical engineering handbook* vol. 2: CRC press, 1999.

[40] I. A. Viktorov, *Rayleigh and Lamb Waves: Physical Theory and Applications*. New York: Plenum Press, 1967.

[41] S. W. Wenzel and R. M. White, "A Multisensor Employing an Ultrasonic Lamb-Wave Oscillator," *IEEE Transactions on Electron Devices,* vol. 35, pp. 735-743, Jun 1988.

[42] R. Ali, "Time-space analysis of a surface-bonded piezoelectric film's response with Lamb wave for diagnostics," *Sensors and Actuators a-Physical,* vol. 161, pp. 12-22, Jun 2010.

[43] R. Hino, M. Esashi, and S. Tanaka, "Antisymmetric-mode lamb wave methanol sensor with edge reflectors for fuel cell applications," in *23rd IEEE International Conference on Micro Electro Mechanical Systems, MEMS 2010, January 24, 2010 - January 28, 2010*, Hong Kong, China, 2010, pp. 871-874.

[44] H. Jia, R. Duhamel, J. F. Manceau, M. de Labachelerie, and F. Bastien, "Improvement of Lamb waves sensors temperature sensitivity compensation," *Sensors and Actuators a-Physical,* vol. 121, pp. 321-326, Jun 30 2005.

[45] T. Laurent, F. O. Bastien, J. C. Pommier, A. Cachard, D. Remiens, and E. Cattan, "Lamb wave and plate mode in ZnO/silicon and AlN/silicon membrane - Application to sensors able to operate in contact with liquid," *Sensors and Actuators a-Physical,* vol. 87, pp. 26-37, Dec 1 2000.

[46] J. Moll, M. V. Golub, E. Glushkov, N. Glushkova, and C. P. Fritzen, "Non-axisymmetric Lamb wave excitation by piezoelectric wafer active sensors," *Sensors and Actuators a-Physical,* vol. 174, pp. 173-180, Feb 2012.

[47] J. H. Kuypers and A. P. Pisano, "Green's function analysis of Lamb wave resonators," in *Ultrasonics Symposium, 2008. IUS 2008. IEEE*, 2008, pp. 1548-1551.

[48] J. A. Jensen, S. I. Nikolov, J. Udesen, P. Munk, K. L. Hansen, M. M. Pedersen*, et al.*, "Recent advances in blood flow vector velocity imaging," in *Ultrasonics Symposium (IUS), 2011 IEEE International*, 2011, pp. 262-271.

[49] T. L. Szabo, *Diagnostic ultrasound imaging: inside out*: Academic Press, 2004.

[50] F. Akasheh, T. Myers, J. D. Fraser, S. Bose, and A. Bandyopadhyay, "Development of piezoelectric micromachined ultrasonic transducers," *Sensors and Actuators a-Physical,* vol. 111, pp. 275-287, Mar 15 2004.

[51] P. C. Eccardt and K. Niederer, "Micromachined ultrasound transducers with improved coupling factors from a CMOS compatible process," *Ultrasonics,* vol. 38, pp. 774-80, Mar 2000.

[52] B. T. Khuri-Yakub and O. Oralkan, "Capacitive micromachined ultrasonic transducers for medical imaging and therapy," *J Micromech Microeng,* vol. 21, pp. 54004-54014, May 2011.

[53] B. T. Khuri-Yakub, O. Oralkan, and M. Kupnik, "Next-Gen Ultrasound," *IEEE Spectrum,* vol. 46, pp. 44-+, May 2009.

[54] M. J. Anderson, J. A. Hill, C. M. Fortunko, N. S. Dogan, and R. D. Moore, "Broadband electrostatic transducers: Modeling and experiments," *The Journal of the Acoustical Society of America,* vol. 97, pp. 262-272, 1995.

[55] M. I. Haller and B. T. KhuriYakub, "A surface micromachined electrostatic ultrasonic air transducer," *IEEE Transactions on Ultrasonics Ferroelectrics and Frequency Control,* vol. 43, pp. 1-6, Jan 1996.

[56] Y. Qiu, J. V. Gigliotti, M. Wallace, F. Griggio, C. E. Demore, S. Cochran*, et al.*, "Piezoelectric micromachined ultrasound transducer (PMUT) arrays for integrated sensing, actuation and imaging," *Sensors (Basel),* vol. 15, pp. 8020-41, 2015.

[57] K. K. Park, O. Oralkan, and B. T. Khuri-Yakub, "A comparison between conventional and collapse-mode capacitive micromachined ultrasonic transducers in 10-MHz 1-D arrays," *IEEE Trans Ultrason Ferroelectr Freq Control,* vol. 60, pp. 1245-55, Jun 2013.

[58] G. Caliano, R. Carotenuto, E. Cianci, V. Foglietti, A. Caronti, A. Iula*, et al.*, "Design, fabrication and characterization of a capacitive micromachined ultrasonic probe for medical imaging," *IEEE Trans Ultrason Ferroelectr Freq*

Control, vol. 52, pp. 2259-69, Dec 2005.

[59] Y. Lu, H. Tang, Q. Wang, S. Fung, J. M. Tsai, M. Daneman*, et al.*, "Waveguide piezoelectric micromachined ultrasonic transducer array for short-range pulse-echo imaging," *Applied Physics Letters,* vol. 106, p. 193506, May 11 2015.

[60] A. Hajati, D. Latev, D. Gardner, M. Ottosson, D. Imai, M. Torrey*, et al.*, "Monolithic ultrasonic integrated circuits based on micromachined semi-ellipsoidal piezoelectric domes," *Applied Physics Letters,* vol. 103, p. 202906, Nov 11 2013.

[61] Y. Lu, H.-Y. Tang, S. Fung, B. E. Boser, and D. A. Horsley, "Pulse-Echo Ultrasound Imaging Using an AlN Piezoelectric Micromachined Ultrasonic Transducer Array With Transmit Beam-Forming," *Journal of Microelectromechanical Systems,* 2016.

[62] B. A. Griffin, M. D. Williams, C. S. Coffman, and M. Sheplak, "Aluminum Nitride Ultrasonic Air-Coupled Actuator," *Journal of Microelectromechanical Systems,* vol. 20, pp. 476-486, Apr 2011.

[63] B. Z. Chen, F. T. Chu, X. Z. Liu, Y. R. Li, J. Rong, and H. B. Jiang, "AlN-based piezoelectric micromachined ultrasonic transducer for photoacoustic imaging," *Applied Physics Letters,* vol. 103, p. 031118, Jul 15 2013.

[64] T. Wang and C. Lee, "Piezoelectric micromachined ultrasonic transducer of flat membrane with boosted transmitting performance," in *18th International Conference on Solid-State Sensors, Actuators and Microsystems (TRANSDUCERS)*, 2015, pp. 666-669.

[65] P. Muralt, N. Ledermann, J. Baborowski, A. Barzegar, S. Gentil, B. Belgacem*, et al.*, "Piezoelectric micromachined ultrasonic transducers based on PZT thin films," *IEEE Trans Ultrason Ferroelectr Freq Control,* vol. 52, pp. 2276-88, Dec 2005.

[66] Y. P. Lu, A. Heidari, and D. A. Horsley, "A High Fill-Factor Annular Array of High Frequency Piezoelectric Micromachined Ultrasonic Transducers," *Journal of Microelectromechanical Systems,* vol. 24, pp. 904-913, Aug 2015.

[67] D. E. Dausch, K. H. Gilchrist, J. B. Carlson, S. D. Hall, J. B. Castellucci, and O. T. von Ramm, "In vivo real-time 3-D intracardiac echo using PMUT arrays," *IEEE Trans Ultrason Ferroelectr Freq Control,* vol. 61, pp. 1754-64, Oct 2014.

[68] O. Rozen, S. T. Block, S. E. Shelton, R. J. Przybyla, and D. A. Horsley, "Air-coupled aluminum nitride piezoelectric micromachined ultrasonic transducers at 0.3 MHz TO 0.9 MHz," in *Micro Electro Mechanical Systems (MEMS), 2015 28th IEEE International Conference on*, 2015, pp. 921-924.

[69] R. J. Przybyla, S. E. Shelton, A. Guedes, I. I. Izyumin, M. H. Kline, D. A.

Horsley, *et al.*, "In-Air Rangefinding With an AlN Piezoelectric Micromachined Ultrasound Transducer," *IEEE Sensors Journal,* vol. 11, pp. 2690-2697, Nov 2011.

[70] R. Przybyla, A. Flynn, V. Jain, S. Shelton, A. Guedes, I. Izyumin, *et al.*, "A micromechanical ultrasonic distance sensor with> 1 meter range," in *Solid-State Sensors, Actuators and Microsystems Conference (TRANSDUCERS), 2011 16th International*, 2011, pp. 2070-2073.

[71] R. Przybyla, I. Izyumin, M. Kline, B. Boser, and S. Shelton, "An ultrasonic rangefinder based on an AlN piezoelectric micromachined ultrasound transducer," in *IEEE Sensors,* 2010, pp. 2417-2421.

[72] R. Przybyla, "Ultrasonic 3D Rangefinder on a Chip," Ph.D. dissertation, Electrical Engineering and Computer Sciences, University of California at Berkeley, Berkeley, CA, 2015.

[73] Y. Lu, H. Tang, S. Fung, Q. Wang, J. M. Tsai, M. Daneman, *et al.*, "Ultrasonic fingerprint sensor using a piezoelectric micromachined ultrasonic transducer array integrated with complementary metal oxide semiconductor electronics," *Applied Physics Letters,* vol. 106, p. 263503, Jun 29 2015.

[74] H. Tang, Y. Lu, S. Fung, J. Tsai, M. Daneman, D. Horsley, *et al.*, "Pulse-echo ultrasonic fingerprint sensor on a chip," in *2015 18th International Conference on Solid-State Sensors, Actuators and Microsystems (TRANSDUCERS)*, 2015, pp. 674-677.

[75] H. Campanella, C. J. Camargo, J. L. Garcia, A. Daza, R. Urquiza, and J. Esteve, "Thin-Film Piezoelectric MEMS Transducer Suitable for Middle-Ear Audio Prostheses," *Journal of Microelectromechanical Systems,* vol. 21, pp. 1452-1463, Dec 2012.

[76] V. M. Mastronardi, F. Guido, M. Amato, M. De Vittorio, and S. Petroni, "Piezoelectric ultrasonic transducer based on flexible AlN," *Microelectronic Engineering,* vol. 121, pp. 59-63, 2014.

[77] M. A. Dubois and P. Muralt, "Stress and piezoelectric properties of aluminum nitride thin films deposited onto metal electrodes by pulsed direct current reactive sputtering," *Journal of Applied Physics,* vol. 89, pp. 6389-6395, Jun 1 2001.

[78] M. Clement, E. Iborra, J. Sangrador, A. Sanz-Hervas, L. Vergara, and M. Aguilar, "Influence of sputtering mechanisms on the preferred orientation of aluminum nitride thin films," *Journal of Applied Physics,* vol. 94, pp. 1495-1500, Aug 1 2003.

[79] J. A. Ruffner, P. G. Clem, B. A. Tuttle, D. Dimos, and D. M. Gonzales, "Effect of substrate composition on the piezoelectric response of reactively sputtered AlN thin films," *Thin Solid Films,* vol. 354, pp. 256-261, Oct 8 1999.

[80] J. H. Harris, R. A. Youngman, and R. G. Teller, "On the Nature of the

Oxygen-Related Defect in Aluminum Nitride," *Journal of Materials Research,* vol. 5, pp. 1763-1773, Aug 1990.

[81] F. Sammoura, K. Smyth, S.-G. Kim, and L. Lin, "An accurate equivalent circuit for the clamped circular multiple-electrode PMUT with residual stress," in *Ultrasonics Symposium (IUS), 2013 IEEE International*, 2013, pp. 275-278.

[82] P. Pobedinskas, J. C. Bolsee, W. Dexters, B. Ruttens, V. Mortet, J. D'Haen*, et al.*, "Thickness dependent residual stress in sputtered AlN thin films," *Thin Solid Films,* vol. 522, pp. 180-185, Nov 1 2012.

[83] F. Martin, P. Muralt, M. A. Dubois, and A. Pezous, "Thickness dependence of the properties of highly c-axis textured AlN thin films," *Journal of Vacuum Science & Technology A,* vol. 22, pp. 361-365, Mar-Apr 2004.

[84] T. Iijima and K. Kunii, "Preparation of texture-controlled lead zirconate titanate diaphragm-type film actuator using a chemical solution method," *Japanese Journal of Applied Physics Part 1-Regular Papers Short Notes & Review Papers,* vol. 40, pp. 5740-5742, Sep 2001.

[85] K. Yamashita, H. Katata, M. Okuyama, H. Miyoshi, G. Kato, S. Aoyagi*, et al.*, "Arrayed ultrasonic microsensors with high directivity for in-air use using PZT thin film on silicon diaphragms," *Sensors and Actuators a-Physical,* vol. 97-8, pp. 302-307, Apr 1 2002.

[86] J. Tsaur, L. Zhang, R. Maeda, S. Matsumoto, and S. Khumpuang, "Design and fabrication of 1D and 2D micro scanners actuated by double layered lead zirconate titanate (PZT) bimorph beams," *Japanese Journal of Applied Physics Part 1-Regular Papers Short Notes & Review Papers,* vol. 41, pp. 4321-4326, Jun 2002.

[87] M. Hoffmann, H. Kuppers, T. Schneller, U. Bottger, U. Schnakenberg, W. Mokwa*, et al.*, "Theoretical calculations and performance results of a PZT thin film actuator," *IEEE Trans Ultrason Ferroelectr Freq Control,* vol. 50, pp. 1240-6, Oct 2003.

[88] H. Chen, K. Udayakumar, C. Gaskey, and L. Cross, "Electrical properties' maxima in thin films of the lead zirconate–lead titanate solid solution system," *Applied physics letters,* vol. 67, pp. 3411-3413, 1995.

[89] T. Kobayashi, M. Ichiki, J. Tsaur, and R. Maeda, "Effect of multi-coating process on the orientation and microstructure of lead zirconate titanate (PZT) thin films derived by chemical solution deposition," *Thin Solid Films,* vol. 489, pp. 74-78, Oct 1 2005.

[90] T. Kobayashi, N. Makimoto, Y. Suzuki, H. Funakubo, T. Oikawa, A. Wada*, et al.*, "Effects of Bipolar Pulse Poling on the Ferroelectric and Piezoelectric Properties of Tetragonal Composition Pb (Zr0. 3, Ti0. 7) O3 Thin Films on Microelectromechanical Systems Microcantilevers," *Japanese Journal of Applied Physics,* vol. 52, p. 09KA01, 2013.

[91] T. Kobayashi, M. Ichiki, R. Kondou, K. Nakamura, and R. Maeda, "Degradation in the ferroelectric and piezoelectric properties of Pb(Zr, Ti) O-3 thin films derived from a MEMS microfabrication process," *Journal of Micromechanics and Microengineering,* vol. 17, pp. 1238-1241, Jul 2007.

[92] T. Kobayashi, Y. Suzuki, N. Makimoto, H. Funakubo, and R. Maeda, "Influence of pulse poling on the piezoelectric property of Pb(Zr0.52,Ti0.48)O3 thin films," *AIP Advances,* vol. 4, p. 117116, 2014.

[93] T. Y. Sheng, Z. Q. Yu, and G. J. Collins, "Disk Hydrogen Plasma Assisted Chemical Vapor-Deposition of Aluminum Nitride," *Applied Physics Letters,* vol. 52, pp. 576-578, Feb 15 1988.

[94] L. Huang, X. D. Wang, K. W. Hipps, U. Mazur, R. Heffron, and J. T. Dickinson, "Chemical etching of ion beam deposited AlN and AlN:H," *Thin Solid Films,* vol. 279, pp. 43-48, Jun 1996.

[95] S. S. Zhang, T. Wang, L. Lou, W. M. Tsang, R. Sawada, D. L. Kwong*, et al.*, "Annularly Grooved Diaphragm Pressure Sensor With Embedded Silicon Nanowires for Low Pressure Application," *Journal of Microelectromechanical Systems,* vol. 23, pp. 1396-1407, Dec 2014.

[96] Y. Hezarjaribi, M. Hamidon, S. Keshmiri, and A. Bahadorimehr, "Capacitive pressure sensors based on MEMS, operating in harsh environments," in *Semiconductor Electronics, 2008. ICSE 2008. IEEE International Conference on*, 2008, pp. 184-187.

[97] C. Kolle, W. Scherr, D. Hammerschmidt, G. Pichler, M. Motz, B. Schaffer*, et al.*, "Ultra low-power monolithically integrated, capacitive pressure sensor for tire pressure monitoring," in *Sensors, 2004. Proceedings of IEEE*, 2004, pp. 244-247.

[98] A. M. Anis, M. Abutaleb, H. F. Ragai, and M. Eladawy, "SiC capacitive pressure sensor node for harsh industrial environment," in *Computational Intelligence, Modelling and Simulation (CIMSiM), 2011 Third International Conference on*, 2011, pp. 413-416.

[99] J. C. Xu, G. Pickrell, X. W. Wang, W. Peng, K. Cooper, and A. B. Wang, "A novel temperature-insensitive optical fiber pressure sensor for harsh environments," *IEEE Photonics Technology Letters,* vol. 17, pp. 870-872, Apr 2005.

[100] L. S. Pakula, H. Yang, H. T. M. Pham, P. J. French, and P. M. Sarro, "Fabrication of a CMOS compatible pressure sensor for harsh environments," *Journal of Micromechanics and Microengineering,* vol. 14, pp. 1478-1483, Nov 2004.

[101] H. San, H. Zhang, Q. Zhang, Y. Yu, and X. Chen, "Silicon–glass-based single piezoresistive pressure sensors for harsh environment applications," *Journal of Micromechanics and Microengineering,* vol. 23, p. 075020, 2013.

[102] X. Zhao, J. M. Tsai, H. Cai, X. M. Ji, J. Zhou, M. H. Bao*, et al.*, "A nano-opto-mechanical pressure sensor via ring resonator," *Opt Express,* vol. 20, pp. 8535-42, Apr 9 2012.

[103] A. A. Ned, R. S. Okojie, and A. D. Kurtz, "6H-SiC pressure sensor operation at 600 C," presented at the 1998 Fourth International High Temperature Electronics Conference, HITEC, 1998.

[104] R. S. Okojie, C. W. Chang, and L. J. Evans, "Reducing DRIE-Induced Trench Effects in SiC Pressure Sensors Using FEA Prediction," *Journal of Microelectromechanical Systems,* vol. 20, pp. 1174-1183, Oct 2011.

[105] R. S. Okojie, A. A. Ned, and A. D. Kurtz, "Operation of α (6H)-SiC pressure sensor at 500 C," *Sensors and Actuators A: Physical,* vol. 66, pp. 200-204, 1998.

[106] R. J. Besson, J. J. Boy, B. Glotin, Y. Jinzaki, B. Sinha, and M. Valdois, "A dual-mode thickness-shear quartz pressure sensor," *IEEE Trans Ultrason Ferroelectr Freq Control,* vol. 40, pp. 584-91, 1993.

[107] L. D. Clayton and E. P. Eernisse, "Quartz thickness-shear mode pressure sensor design for enhanced sensitivity," *IEEE Trans Ultrason Ferroelectr Freq Control,* vol. 45, pp. 1196-203, 1998.

[108] E. P. EerNisse and R. B. Wiggins, "Review of Thickness-Shear Mode Quartz Resonator Sensors for Temperature and Pressure," *IEEE Sensors Journal,* vol. 1, pp. 79-87, Jun 2001.

[109] P. Kropelnicki, K. M. Muckensturm, X. J. Mu, A. B. Randles, H. Cai, W. C. Sng*, et al.*, "CMOS-compatible ruggedized high-temperature Lamb wave pressure sensor," *Journal of Micromechanics and Microengineering,* vol. 23, p. 085018 (9 pp.), Aug 2013.

[110] T. Wang, X. J. Mu, P. Kropelnicki, A. B. Randles, and C. Lee, "Viscosity and density decoupling method using a higher order Lamb wave sensor," *Journal of Micromechanics and Microengineering,* vol. 24, p. 075002, Jul 2014.

[111] X. J. Mu, P. Kropelnicki, Y. Wang, A. B. Randles, K. T. C. Chai, H. Cai*, et al.*, "Dual mode acoustic wave sensor for precise pressure reading," *Applied Physics Letters,* vol. 105, p. 113507, Sep 15 2014.

[112] V. V. e. Bolotin, G. Herrmann, and T. Lusher, *Nonconservative problems of the theory of elastic stability* vol. 1991: Pergamon Press Oxford, 1963.

[113] A. Nalamwar and M. Epstein, "Surface acoustic waves in strained media," *Journal of Applied Physics,* vol. 47, pp. 43-48, 1976.

[114] M. Hirao and H. Ogi, *EMATs for science and industry: noncontacting ultrasonic measurements*: Springer Science & Business Media, 2003.

[115] A. L. Nalamwar and M. Epstein, "Effects of Applied Strain in Zno Thin-Film

Saw Devices," *IEEE Transactions on Sonics and Ultrasonics,* vol. 23, pp. 144-147, 1976.

[116] V. M. Koleshko, Y. V. Meshkov, and V. V. Barkalin, "Strain Effect in Single-Crystal Silicon-Based Multilayer Surface Acoustic-Wave Structures," *Thin Solid Films,* vol. 190, pp. 359-372, Sep 15 1990.

[117] P. Keating, "Theory of the third-order elastic constants of diamond-like crystals," *Physical Review,* vol. 149, p. 674, 1966.

[118] M. Cole, G. Sehra, J. W. Gardner, and V. K. Varadan, "Development of smart tongue devices for measurement of liquid properties," *IEEE Sensors Journal,* vol. 4, pp. 543-550, Oct 2004.

[119] Y. Q. Fu, J. K. Luo, X. Y. Du, A. J. Flewitt, Y. Li, G. H. Markx*, et al.*, "Recent developments on ZnO films for acoustic wave based bio-sensing and microfluidic applications: a review," *Sensors and Actuators B: Chemical,* vol. 143, pp. 606-619, 2010.

[120] I. Voiculescu and A. N. Nordin, "Acoustic wave based MEMS devices for biosensing applications," *Biosens Bioelectron,* vol. 33, pp. 1-9, Mar 15 2012.

[121] B. E. Rapp, F. J. Gruhl, and K. Lange, "Biosensors with label-free detection designed for diagnostic applications," *Anal Bioanal Chem,* vol. 398, pp. 2403-12, Nov 2010.

[122] U. Latif, A. Mujahid, A. Afzal, R. Sikorski, P. A. Lieberzeit, and F. L. Dickert, "Dual and tetraelectrode QCMs using imprinted polymers as receptors for ions and neutral analytes," *Anal Bioanal Chem,* vol. 400, pp. 2507-15, Jun 2011.

[123] M. A. Cooper, "Label-free screening of bio-molecular interactions," *Anal Bioanal Chem,* vol. 377, pp. 834-42, Nov 2003.

[124] K. Lange, B. E. Rapp, and M. Rapp, "Surface acoustic wave biosensors: a review," *Anal Bioanal Chem,* vol. 391, pp. 1509-19, Jul 2008.

[125] F. Priego Capote and M. D. Luque de Castro, "Ultrasound in analytical chemistry," *Anal Bioanal Chem,* vol. 387, pp. 249-57, Jan 2007.

[126] M. Olfatnia, Z. Shen, J. M. Miao, L. S. Ong, T. Xu, and M. Ebrahimi, "Medium damping influences on the resonant frequency and quality factor of piezoelectric circular microdiaphragm sensors," *Journal of Micromechanics and Microengineering,* vol. 21, Apr 2011.

[127] T. Nomura, A. Saitoh, and Y. Horikoshi, "Measurement of acoustic properties of liquid using liquid flow SH-SAW sensor system," in *8th International Meeting on Chemical Sensors IMCS-8, 2-5 July 2000*, Switzerland, 2001, pp. 69-73.

[128] J. L. Vivancos, Z. Racz, M. Cole, and J. W. Gardner, "Surface acoustic wave based analytical system for the detection of liquid detergents," *Sensors and*

Actuators B-Chemical, vol. 171, pp. 469-477, Aug-Sep 2012.

[129] W. C. Xu, J. Appel, and J. Chae, "Real-Time Monitoring of Whole Blood Coagulation Using a Microfabricated Contour-Mode Film Bulk Acoustic Resonator," *Journal of Microelectromechanical Systems,* vol. 21, pp. 302-307, Apr 2012.

[130] K. Mitsakakis, A. Tsortos, J. Kondoh, and E. Gizeli, "Parametric study of SH-SAW device response to various types of surface perturbations," *Sensors and Actuators B-Chemical,* vol. 138, pp. 408-416, May 6 2009.

[131] I. Oita, H. Halewyck, B. Thys, B. Rombaut, Y. Vander Heyden, and D. Mangelings, "Microfluidics in macro-biomolecules analysis: macro inside in a nano world," *Anal Bioanal Chem,* vol. 398, pp. 239-64, Sep 2010.

[132] D. Chen, J. J. Wang, Y. Xu, D. H. Li, L. Y. Zhang, and W. H. Liu, "A lateral field excited ZnO film bulk acoustic wave sensor working in viscous environments," *Journal of Micromechanics and Microengineering,* vol. 23, p. 095032, Sep 2013.

[133] N. Doy, G. McHale, M. I. Newton, C. Hardacre, R. Ge, J. M. Macinnes*, et al.*, "Small volume laboratory on a chip measurements incorporating the quartz crystal microbalance to measure the viscosity-density product of room temperature ionic liquids," *Biomicrofluidics,* vol. 4, p. 14107, 2010.

[134] S. Furukawa, H. Furukawa, T. Nomura, T. Yasuda, and M. Tamura, "Precise estimation of viscosity of liquid using leaky surface acoustic waves propagating along liquid/polymer/LiNbO3 structures," in *IEEE 1992 Ultrasonics Symposium (Cat. No.92CH3118-7), 20-23 Oct. 1992*, New York, NY, USA, 1992, pp. 303-6.

[135] T. Sato, H. Okajima, Y. Kashiwase, R. Motegi, and H. Nakajima, "Shear Horizontal Acoustic Plate Mode Viscosity Sensor," *Japanese Journal of Applied Physics Part 1-Regular Papers Short Notes & Review Papers,* vol. 32, pp. 2392-2395, May 1993.

[136] F. Herrmann, D. Hahn, and S. Buttgenbach, "Separate determination of liquid density and viscosity with sagittally corrugated Love-mode sensors," *Sensors and Actuators a-Physical,* vol. 78, pp. 99-107, Dec 14 1999.

[137] B. A. Martin, S. W. Wenzel, and R. M. White, "Viscosity and density sensing with ultrasonic plate waves," in *5th International Conference on Solid-State Sensors and Actuators and Eurosensors III, 25-30 June 1989*, Switzerland, 1990, pp. 704-8.

[138] L. Zhou, Y. Wu, M. Xuan, J. F. Manceau, and F. Bastien, "A multi-parameter decoupling method with a Lamb wave sensor for improving the selectivity of label-free liquid detection," *Sensors (Basel),* vol. 12, pp. 10369-80, 2012.

[139] I. V. Anisimkin, "A novel Lamb-mode liquid sensor array," in *2003 IEEE Ultrasonics Symposium, 5-8 Oct. 2003*, Piscataway, NJ, USA, pp. 1326-9.

[140] M. J. Vellekoop, G. W. Lubking, P. M. Sarro, and A. Venema, "Evaluation of liquid properties using a silicon Lamb wave sensor," in *7th International Conference on Solid State Sensors and Actuators (Transducers '93), 7-10 June 1993*, Switzerland, 1994, pp. 175-80.

[141] L. Arapan, E. Anderas, I. Katardjiev, and V. Yantchev, "Sensitivity Features of Thin Film Plate Acoustic Wave Resonators," *IEEE Sensors Journal,* vol. 11, pp. 3330-3331, Dec 2011.

[142] V. Yantchev and I. Katardjiev, "Thin film Lamb wave resonators in frequency control and sensing applications: a review," *Journal of Micromechanics and Microengineering,* vol. 23, p. 043001 (14 pp.), Apr 2013.

[143] C.-M. Lin, Y.-Y. Chen, V. V. Felmetsger, G. Vigevani, D. G. Senesky, and A. P. Pisano, "Micromachined aluminum nitride acoustic resonators with an epitaxial silicon carbide layer utilizing high-order lamb wave modes," in *2012 IEEE 25th International Conference on Micro Electro Mechanical Systems, MEMS 2012, January 29, 2012 - February 2, 2012*, Paris, France, 2012, pp. 733-736.

[144] C. M. Lin, Y. Y. Chen, V. V. Felmetsger, D. G. Senesky, and A. P. Pisano, "AlN/3C-SiC composite plate enabling high-frequency and high-Q micromechanical resonators," *Adv Mater,* vol. 24, pp. 2722-7, May 22 2012.

[145] L. Q. Zhou, J. F. Manceau, and F. Bastien, "Influence of gases on Lamb waves propagations in resonator," *Applied Physics Letters,* vol. 95, Nov 30 2009.

[146] "CRC handbook of chemistry and physics," vol. 51458, 79 ed. Cleveland, Ohio: CRC Press, 1998.

[147] B. Jakoby and M. J. Vellekoop, "Viscosity sensing using a Love-wave device," *Sensors and Actuators a-Physical,* vol. 68, pp. 275-281, Jun 15 1998.

[148] A. K. Pantazis, E. Gizeli, and G. Konstantinidis, "A high frequency GaN Lamb-wave sensor device," *Applied Physics Letters,* vol. 96, p. 194103 (3 pp.), May 10 2010.

[149] J. Kestin, H. E. Khalifa, and R. J. Correia, "Tables of the dynamic and kinematic viscosity of aqueous NaCl solutions in the temperature range 20-150C and the pressure range 0.1-35 MPa," *Journal of Physical and Chemical Reference Data,* vol. 10, pp. 71-87, 1981.

[150] J. Cho, M. Anderson, R. Richards, D. Bahr, and C. Richards, "Optimization of electromechanical coupling for a thin-film PZT membrane: II. Experiment," *Journal of Micromechanics and Microengineering,* vol. 15, pp. 1804-1809, Oct 2005.

[151] S. Shelton, M.-L. Chan, H. Park, D. Horsley, B. Boser, I. Izyumin*, et al.*, "CMOS-compatible AlN piezoelectric micromachined ultrasonic transducers," in *Ultrasonics Symposium (IUS), 2009 IEEE International*, 2009, pp. 402-405.

[152] Y.-F. Wang, Y. Yang, T.-L. Ren, H. Chen, W.-j. Liao, X.-m. Kong*, et al.*, "Ultrasonic transducer array design for medical imaging based on MEMS technologies," in *Biomedical Engineering and Informatics (BMEI), 2010 3rd International Conference on*, 2010, pp. 666-669.

[153] J. J. Bernstein, S. L. Finberg, K. Houston, L. C. Niles, H. D. Chen, L. E. Cross*, et al.*, "Micromachined high frequency ferroelectric sonar transducers," *IEEE Transactions on Ultrasonics Ferroelectrics and Frequency Control,* vol. 44, pp. 960-969, Sep 1997.

[154] J. H. Mo, A. L. Robinson, D. W. Fitting, F. L. Terry, and P. L. Carson, "Micromachining for Improvement of Integrated Ultrasonic Transducer Sensitivity," *IEEE Transactions on Electron Devices,* vol. 37, pp. 134-140, Jan 1990.

[155] P. Muralt and J. Baborowski, "Micromachined ultrasonic transducers and acoustic sensors based on piezoelectric thin films," *Journal of Electroceramics,* vol. 12, pp. 101-108, Jan-Mar 2004.

[156] B. Belgacem, F. Calame, and P. Muralt, "Piezoelectric micromachined ultrasonic transducers with thick PZT sol gel films," *Journal of Electroceramics,* vol. 19, pp. 369-373, Dec 2007.

[157] H. S. Choi, M. J. Anderson, J. L. Ding, and A. Bandyopadhyay, "A two-dimensional electromechanical composite plate model for piezoelectric micromachined ultrasonic transducers (pMUTs)," *Journal of Micromechanics and Microengineering,* vol. 20, p. 015013, Jan 2010.

[158] K. Smyth, S. Bathurst, F. Sammoura, and S. G. Kim, "Analytic solution for N-electrode actuated piezoelectric disk with application to piezoelectric micromachined ultrasonic transducers," *IEEE Trans Ultrason Ferroelectr Freq Control,* vol. 60, pp. 1756-67, Aug 2013.

[159] F. Sammoura and S. G. Kim, "Theoretical modeling and equivalent electric circuit of a bimorph piezoelectric micromachined ultrasonic transducer," *IEEE Trans Ultrason Ferroelectr Freq Control,* vol. 59, pp. 990-8, May 2012.

[160] F. Sammoura, K. Smyth, S. Bathurst, and S.-G. Kim, "An analytical analysis of the sensitivity of circular piezoelectric micromachined ultrasonic transducers to residual stress," in *Ultrasonics Symposium (IUS), 2012 IEEE International*, 2012, pp. 580-583.

[161] D. J. Morris, R. F. Need, M. J. Anderson, and D. F. Bahr, "Enhanced actuation and acoustic transduction by pressurization of micromachined piezoelectric diaphragms," *Sensors and Actuators a-Physical,* vol. 161, pp. 164-172, Jun 2010.

[162] K. Yamashita, H. Nishimoto, and M. Okuyama, "Diaphragm deflection control of piezoelectric ultrasonic microsensors for sensitivity improvement," *Sensors and Actuators a-Physical,* vol. 139, pp. 118-123, Sep 12 2007.

[163] S. Akhbari, F. Sammoura, S. Shelton, C. Yang, D. Horsley, and L. Lin, "Highly responsive curved aluminum nitride pMUT," in *Micro Electro Mechanical Systems (MEMS), 2014 IEEE 27th International Conference on*, 2014, pp. 124-127.

[164] S. Akhbari, F. Sammoura, C. Yang, A. Heidari, D. Horsley, and L. Lin, "Self-curved diaphragms by stress engineering for highly responsive pMUT," in *Micro Electro Mechanical Systems (MEMS), 2015 28th IEEE International Conference on*, 2015, pp. 837-840.

[165] A. Guedes, S. Shelton, R. Przybyla, I. Izyumin, B. Boser, and D. Horsley, "Aluminum nitride pMUT based on a flexurally-suspended membrane," in *Solid-State Sensors, Actuators and Microsystems Conference (TRANSDUCERS), 2011 16th International*, 2011, pp. 2062-2065.

[166] J. Jung, S. Kim, W. Lee, and H. Choi, "Fabrication of a two-dimensional piezoelectric micromachined ultrasonic transducer array using a top-crossover-to-bottom structure and metal bridge connections," *Journal of Micromechanics and Microengineering,* vol. 23, p. 125037, Dec 2013.

[167] Y. Huang, X. Zhuang, E. O. Haeggstrom, A. S. Ergun, C. H. Cheng, and B. T. Khuri-Yakub, "Capacitive micromachined ultrasonic transducers with piston-shaped membranes: fabrication and experimental characterization," *IEEE Trans Ultrason Ferroelectr Freq Control,* vol. 56, pp. 136-45, Jan 2009.

[168] Y. P. Lu and D. A. Horsley, "Modeling, Fabrication, and Characterization of Piezoelectric Micromachined Ultrasonic Transducer Arrays Based on Cavity SOI Wafers," *Journal of Microelectromechanical Systems,* vol. 24, pp. 1142-1149, Aug 2015.

[169] T. Wang, X. J. Mu, A. B. Randles, Y. D. Gu, and C. Lee, "Diaphragm shape effect on the sensitivity of surface acoustic wave based pressure sensor for harsh environment," *Applied Physics Letters,* vol. 107, p. 123501, Sep 21 2015.

[170] T. Wang and C. Lee, "Zero-Bending Piezoelectric Micromachined Ultrasonic Transducer (pMUT) With Enhanced Transmitting Performance," *Journal of Microelectromechanical Systems,* vol. 24, pp. 2083-2091, Dec 2015.

[171] T. Wang, R. Sawada, and C. Lee, "A Piezoelectric Micromachined Ultrasonic Transducer Using Piston-Like Membrane Motion," *IEEE Electron Device Letters,* vol. 36, pp. 957-959, Sep 2015.

[172] T. Wang, T. Kobayashi, and C. Lee, "Micromachined piezoelectric ultrasonic transducer with ultra-wide frequency bandwidth," *Applied Physics Letters,* vol. 106, p. 013501, Jan 5 2015.

[173] Z. H. Wang, J. M. Miao, C. W. Tan, and T. Xu, "Fabrication of piezoelectric MEMS devices-from thin film to bulk PZT wafer," *Journal of Electroceramics,* vol. 24, pp. 25-32, Feb 2010.

[174] Z. H. Wang, J. M. Miao, and W. G. Zhu, "Micromachined ultrasonic transducers and arrays based on piezoelectric thick film," *Applied Physics a-Materials Science & Processing,* vol. 91, pp. 107-117, Apr 2008.

[175] Z. H. Wang, J. M. Miao, and W. G. Zhu, "Piezoelectric thick films and their application in MEMS," *Journal of the European Ceramic Society,* vol. 27, pp. 3759-3764, 2007.

[176] Z. H. Wang, W. G. Zhu, O. K. Tan, C. Chao, H. Zhu, and J. M. Miao, "Ultrasound radiating performances of piezoelectric micromachined ultrasonic transmitter," *Applied Physics Letters,* vol. 86, pp. 033508-033508-3, Jan 17 2005.

[177] Z. Wang, W. Zhu, H. Zhu, J. Miao, C. Chao, C. Zhao*, et al.*, "Fabrication and characterization of piezoelectric micromachined ultrasonic transducers with thick composite PZT films," *IEEE Trans Ultrason Ferroelectr Freq Control,* vol. 52, pp. 2289-97, Dec 2005.

[178] T. Kobayashi, M. Ichiki, T. Noguchi, and R. Maeda, "Deflection of wafers and cantilevers with Pt/LNO/PZT/LNO/Pt/Ti/SiO2 multilayered structure," *Thin Solid Films,* vol. 516, pp. 5272-5276, Jun 30 2008.

[179] H. Zhu, J. M. Mioa, Z. H. Wang, C. L. Zhao, and W. G. Zhu, "Fabrication of ultrasonic arrays with 7 mu m PZT thick films as ultrasonic emitter for object detection in air," *Sensors and Actuators a-Physical,* vol. 123-24, pp. 614-619, Sep 23 2005.

[180] J. Jung, W. Lee, W. Kang, H. Hong, H. Y. Song, I.-y. Oh*, et al.*, "A top-crossover-to-bottom addressed segmented annular array using piezoelectric micromachined ultrasonic transducers," *Journal of Micromechanics and Microengineering,* vol. 25, p. 115024, 2015.

[181] N. M. Tole and H. Ostensen, *Basic Physics of Ultrasonographic Imaging*: World Health Organization, 2005.

[182] P. R. Hoskins, K. Martin, and A. Thrush, *Diagnostic Ultrasound: Physics and Equipment*: Cambridge University Press, 2010.

[183] B. Angelsen, *Ultrasound Imaging: Waves, Signals, and Signal Processing*: Emantec, 2000.

[184] D. E. Dausch, J. B. Castellucci, D. R. Chou, and O. T. von Ramm, "Theory and operation of 2-D array piezoelectric micromachined ultrasound transducers," *IEEE Trans Ultrason Ferroelectr Freq Control,* vol. 55, pp. 2484-92, Nov 2008.

[185] G. Percin and B. T. Khuri-Yakub, "Piezoelectrically actuated flextensional micromachined ultrasound transducers--II: fabrication and experiments," *IEEE Trans Ultrason Ferroelectr Freq Control,* vol. 49, pp. 585-95, May 2002.

[186] A. Hajati, D. Latev, D. Gardner, A. Hajati, D. Imai, M. Torrey*, et al.*,

"Three-dimensional micro electromechanical system piezoelectric ultrasound transducer," *Applied Physics Letters,* vol. 101, p. 253101, Dec 17 2012.

[187] H. S. Choi, J. L. Ding, A. Bandyopadhyay, M. J. Anderson, and S. Bose, "Characterization and modeling of a piezoelectric micromachined ultrasonic transducer with a very large length/width aspect ratio," *Journal of Micromechanics and Microengineering,* vol. 18, p. 025037, Feb 2008.

[188] T. D. Rossing and N. H. Fletcher, *Principles of Vibration and Sound*: Springer, 2004.

[189] V. Chan and A. Perlas, "Basics of ultrasound imaging," in *Atlas of Ultrasound-Guided Procedures in Interventional Pain Management*, ed: Springer, 2011, pp. 13-19.

Appendix: List of Publication

Journal Papers

1. **Tao Wang**, Takeshi Kobayashi and Chengkuo Lee, "Highly Sensitive Piezoelectric Micromachined Ultrasonic Transducer (pMUT) Operated in Air", ***Micro & Nano Letters***, *under review*.

2. Qiongfeng Shi, **Tao Wang** and Chengkuo Lee, "MEMS Based Broadband Piezoelectric Ultrasonic Energy Harvester (PUEH) for Enabling Self-Powered Implantable Biomedical Devices", ***Scientific Report,*** *in press.*

3. **Tao Wang**, Xiaojing Mu, Andrew Benson Randles, Yuandong Gu and Chengkuo Lee, "Diaphragm shape effect on the sensitivity of surface acoustic wave (SAW) based pressure sensor for harsh environment", ***Applied Physics Letters,*** vol.107, issue 12, pp. 123501, 2015.

4. **Tao Wang** and Chengkuo Lee, "Zero-Bending Piezoelectric Micromachined Ultrasonic Transducer (pMUT) with Enhanced Transmitting Performance", ***IEEE Journal of Microelectromechanical Systems.*** vol. 24, no.6, pp. 2083-2091, 2015.

5. **Tao Wang**, Renshi Sawada, and Chengkuo Lee, "A Piezoelectric Micromachined Ultrasonic Transducer (pMUT) Using Piston-like Membrane Motion*",* ***IEEE Electron Device Letters***, vol.36, no. 9, pp.1-3, 2015.

6. **Tao Wang**, Takeshi Kobayashi and Chengkuo Lee, "Ultra-wide frequency bandwidth piezoelectric micromachined ultrasonic transducer", ***Applied Physics Letters***, vol. 106, no. 1, pp. 013501, 2015.

7. Songsong Zhang, **Tao Wang**, Liang Lou, Wei Mong Tsang, Renshi Sawada, Dim-Lee Kwong and Chengkuo Lee, "Annularly grooved diaphragm pressure sensor with embedded silicon nanowires for low pressure application", ***IEEE Journal of Microelectromechanical Systems***, vol.23, No.6, pp. 1396-1407, 2014.

8. **Tao Wang**, Xiaojing Mu, Piotr Kropelnicki, Andrew Benson Randles and Chengkuo Lee, "Viscosity and density decoupling method by using higher-order Lamb wave sensor", ***IOP Journal of Micromechanics and Microengineering***, vol. 24, no. 7, pp. 075002, 2014.

9. **Tao Wang**, Liang Lou, and Chengkuo Lee, "A junctionless gate-all-around silicon nanowire FET of high linearity and its potential applications", ***IEEE Electron Device Letters,*** vol. 34, no. 4, pp. 478-480, 2013.

Awards

1. **Best Paper Award Finalist (Top 5 Papers)** for *10th IEEE International Conference on Nano/Micro Engineered and Molecular Systems (IEEE NEMS 2015).*

Invited Talks

2. **Tao Wang**, Bin Yang, Renshi Sawada and Chengkuo Lee, "Piezoelectric micromachined ultrasonic transducer (pMUT) for biomedical applications", ***International Conference on BioSensors, BioElectronics, BioMedical Devices, BioMEMS/NEMS and Applications (Bio4Apps 2015)***, Fukuoka, Japan, Dec. 9-11, 2015.

3. Songsong Zhang, **Tao Wang**, Renshi Sawada, and Chengkuo Lee, "Silicon nanowire embedded diaphragm based pressure sensor with micro-grooved structure to improve sensitivity", ***The 2th Japan-Singapore Research Exchange & ICT Farm Project***, Kyushu University, Japan, Aug 16-17, 2013.

Conference Papers

1. **Tao Wang**, Takeshi Kobayashi, Hao Wang and Chengkuo Lee, "Highly Sensitive Piezoelectric Micromachined Ultrasonic Transducer (pMUT) Operated in Air", ***The 11th IEEE Intern. Conf. on Nano/Micro Engineered and Molecular Systems (IEEE NEMS 2016)***, Sendai, Japan, 17-20 April, 2016.

2. **Tao Wang** and Chengkuo Lee, "Electrically Switchable Multi-Frequency Piezoelectric Micromachined Ultrasonic Transducer (pMUT)", ***The 29th IEEE International Conference on Micro Electro Mechanical Systems (MEMS 2016)***, Shanghai, China, Jan. 24-28, 2016.

3. Qiongfeng Shi, **Tao Wang**, Takeshi Kobayashi and Chengkuo Lee, "MEMS Based Piezoelectric Ultrasonic Energy Harvester for Selfpowered Under-water Applications", ***The 29th IEEE International Conference on Micro Electro Mechanical Systems (MEMS 2016)***, Shanghai, China, Jan. 24-28, 2016.

4. **Tao Wang** and Chengkuo Lee, "Piezoelectric Micromachined Ultrasonic Transducer of Flat Membrane with Boosted Transmitting Performance", ***The 18th Intern. Conf. on Solid-State Sensors, Actuators and Microsystems (Transducers 2015)***, W3E.002, pp.666-669, Anchorage, Alaska, U.S., June 21-25, 2015.

5. **Tao Wang**, Takeshi Kobayashi and Chengkuo Lee, "Broadband Piezoelectric

Micromachined Ultrasonic Transducer (pMUT) Using Mode-Merged Design", ***The 10th IEEE Intern. Conf. on Nano/Micro Engineered and Molecular Systems (IEEE NEMS 2015)***, Xi'an, China, Apr. 7-11, 2015. **(Plenary Talk)**

6. Prakash Pitchappa, Lokesh Dhakar, Chong Pei Ho, You Qian, **Tao Wang** and Chengkuo Lee, "Subwavelength MEMS cantilever array for dynamic manipulation of terahertz waves" , ***The 10th IEEE Intern. Conf. on Nano/Micro Engineered and Molecular Systems (IEEE NEMS 2015)***, Xi'an, China, Apr. 7-11, 2015.

7. Songsong Zhang, **Tao Wang**, Renshi Sawada and **Chengkuo Lee**, "NEMS pressure sensor aiming at low pressure sensing for healthcare applications", ***Intern. Union of Mat. Research Soc. - Intern. Conf. in Asia. (IUMRS-ICA 2014),*** Fukuoka, Japan, Aug. 24 – 28, 2014.

8. **Tao Wang**, Xiaojing Mu, Piotr Kropelnicki, Andrew Benson Randles and Chengkuo Lee, "MEMS based liquid density and viscosity sensor", ***The 6th International Symposium on Microchemistry and Microsystems (ISMM 2014),*** Singapore, July 30 – Aug. 1, 2014.

9. **Tao Wang**, Xiaojing Mu, Piotr Kropelnicki, Andrew Benson Randles and **Chengkuo Lee**, "A CMOS- compatible lamb wave resonator for liquid properties sensing", ***2014 IEEE Intern. Conf. on Intelligent Sensors, Sensor Networks and Information Processing (ISSNIP 2014)***, Singapore, Apr. 21–24, 2014.

10. Songsong Zhang, **Tao Wang**, Liang Lou, Wei-Mong Tsang, Dim-Lee Kwong and **Chengkuo Lee**, "Silicon nanowires embedded pressure sensor with annularly grooved diaphragm for sensitivity improvement", ***2014 IEEE Intern. Conf. on Intelligent Sensors, Sensor Networks and Information Processing (ISSNIP 2014),*** Singapore, Apr. 21–24, 2014.

11. Songsong Zhang, Liang Lou, **Tao Wang**, Wei Mong Tsang, Dim-Lee Kwong and **Chengkuo Lee**, "Characterizations of silicon nanowires (SiNWs) embedded NEMS sensors and for potential bio-medical applications", ***IEEE MTT-S International Microwave Workshop Series on RF and Wireless Technologies for Biomedical and Healthcare Applications (IMWS-Bio 2013)***, MPoster-20, Singapore, Dec. 09-11,2013.

12. Songsong Zhang, **Tao Wang**, Liang Lou, Wei Mong Tsang, Renshi Sawada and **Chengkuo Lee**, "Piezoresistive silicon nanowires based NEMS pressure sensors for potential biomedical applications", ***Intern. Conf. on BioElectronics, BioSensor, BioMedical Devices, BioMEMS/NEMS and Applications 2013 (Bio4Apps 2013) & 5th Sensing Biology Symposium***, PNM-1, Tokyo Medical and Dental University, Tokyo, Japan, Oct. 30-31, 2013.